Thermophysical Properties of Nanofluids

Oscar Javier Gutierrez

THESE DE DOCTORAT DE L'UNIVERSITE CLAUDE BERNARD DE LYON 1

En cotutelle avec:
L'UNIVERSITÉ NATIONALE AUTONOME DU MEXIQUE

Ecole Doctorale 52
Physique et Astrophysique

Discipline: Physique

Soutenue publiquement le 12/06/2023, par :
Oscar Javier GUTIERREZ VARELA

Propriétés Thermophysiques des Nanofluides

Devant le jury composé de :

ESQUIVEL SIRVENT, Raul Patricio, Professeur Université Nationale Autonome du Mexique
Président de Jury et Examinateur

ALEJANDRE RAMIREZ, José Reyes, Autonome Métropolitaine (Mexique) Professeur Université
Rapporteur
RAMOS ALVARADO, Bladimir Professeur Associé Université d'Etat de Pennsylvanie (USA)
Rapporteur
BANFI, Francesco, Professeur des Universités Université Lyon 1, Examinateur
GAUDRY, Émilie, Professeure des Universités Université de Lorraine, Examinatrice
MORENO RAZO, José Antonio,Professeur Université Autonome Métropolitaine (Mexique), Examinateur
MERABIA, Samy, Directeur de Recherche CNRS Lyon, Directeur de thèse
SANTAMARIA ORTIZ Ruben, Professeur Université Autonome Métropolitaine (Mexique),Examinateur

Agradecimientos

Primeramente quiero agradecer a mi compañera de vida, mi mejor amiga y mi esposa Larissa García Romero quien me acompañó, me apoyó y siempre ha estado a mi lado durante todo este proceso de conseguir mi grado de Doctor en Ciencias en el área de Física y en demás procesos de mi vida. Te agradezco infinitamente todo tu amor, apoyo y paciencia ya que gracias a ti esta etapa académica de mi vida fue más fácil de sobrellevar. Te amo y siempre estaré a tu lado así como tu lo has estado.

También quiero agradecer de todo corazón a mis padres, Oscar Javier Gutiérrez Calzadillas y Guadalupe Varela Caro, y a mi hermana Alejandra Gutiérrez Varela, quienes siempre han estado conmigo en todo momento bueno y malo brindándome todo su apoyo, paciencia y amor, ayudándome a cumplir mis sueños y enseñándome a ser una mejor persona con su gran ejemplo. Sin ellos no hubiera podido cumplir esta meta que en gran parte también es suya. Les agradezco infinitamente.

Agradezco a mi asesores de tesis el Prof. Samy Merabia y el Prof. Rubén Santamaría Ortiz por todo su tiempo dedicado en mi formación, quienes me guiaron a través de su experiencia para poderme formar en el camino de la ciencia e investigación, siempre con el objetivo de que aprendiera los conceptos básicos y primordiales de una carrera científica, tanto desde el punto de vista teórico, práctico y los aspectos éticos de la investigación.

Agradezco a los demás miembros de mi comité tutor, a la Prof. Renela María Valladares Mc Nelis y al Prof. Francisco Javier Sevilla Pérez. Al Instituto de Física de la UNAM y al Institut Lumière Matière de la UCBL y a todo su personal que siempre me brindaron su apoyo. También agradezco al programa IDEXLYON de la Université de Lyon que me dió su apoyo para poder realizar una estancia en el Institut Lumière Matière de la UCBL.

También agradezco todo el soporte de PSMN (Pôle Scientifique de Modélisation Numérique) de la ENS de Lyon por todos los recursos computacionales brindados. Al centro de cómputo de la Institut Lumière Matière de la UCBL, del Instituto de Física de la UNAM y a DGTIC-UNAM por facilitarnos el acceso a Miztli para realizar los cálculos numéricos y apoyo técnico. Agradezco al CONACyT por el apoyo económico brinado durante todos mis estudios de doctorado.

Summary

Spanish version

El objetivo de esta tesis se puede resumir en dos puntos: el primero consiste en poner a prueba la termodinámica para sistemas lejos del límite termodinámico, esto es, cuando $N \to \infty$ y $V \to \infty$ está lejos de satisfacerse. Para este fin utilizamos simulaciones de Dinámica Molecular para un sistema de 126 moléculas de agua en donde las interacciones inter- e intra-moleculares se simulan con cálculos de DFT y están contendias en un volumen de unos pocos nm^3. A su vez, proponemos una metodología para el confinamiento de sistemas moleculares en el que se simulan condiciones isobáricas con más apego a la realidad física. Este sistema de confinamiento consiste de una cobertura con descripción tipo atomística que es movible y ejerce una fuerza constante sobre el fluido, similar a un pistón que confina a un fluido ejerciendo una presión constante.

Calculamos diferentes parámetros termofísicos del sistema de unas cuantas decenas de moléculas de agua utilizando principalmente conceptos termodinámicos. Los valores que obtenemos están en general en el orden de magnitud esperado según datos experimentales. Esto nos lleva a concluir que la termodinámica sigue siendo válida incluso para sistemas de decenas de moléculas contenidas en un volumen de pocos nm^3. Con respecto a la metodología propuesta para simular condiciones isobáricas en Dinámica Molecular, tenemos que las densidades en las que el sistema se equilibra corresponden en forma cuantitativa con los valores experimentales según la temperatura y la presión impuestas en la simulación. Esto, en conjunto con los valores de los parámetros termofísicos que calculamos el pequeño bulto de agua, nos permiten concluir que la metodología es eficaz para simular condiciones isobáricas en cálculos de Dinámica Molecular. Sin embargo, algunos factores deben de ser mejorados con el fin de hacer más eficiente el método desde el punto de vista computacional.

El segundo punto de la tesis consiste en estudiar las propiedades de transporte térmico entre nanopartículas metálicas y un medio acuoso. Para esto utilizamos principalmente simulaciones de Dinámica Molecular usando cálculos clásicos. Los sistemas moleculares consisten de cientos de miles de átomos. Más específicamente, consideramos nanopartículas de diferentes tamaños, geometrías y humectaciones inmersas en un cubo de agua. Nuestras simulaciones recrean experimentos en los que nanopartículas plasmónicas dispersas en un medio acuoso son calentadas por medio de la irradiación de un láser.

Al considerar un calentamiento moderado de la nanopartícula tal que no genera una transición de fase del líquido circundante, observamos lo siguiente. El transporte de calor es más eficiente al reducir el tamaño de la nanopartícula sin importar el tipo de humectación en la interfaz nanopartícula-medio acuoso. Esto se observa al calcular la conductancia térmica interfacial, la cual muestra que al reducir el radio de la nanopartícula su valor incrementa. Con el fin de explicar este comportamiento, hacemos un análisis de diferentes parámetros físicos y observamos lo siguiente. El número de moléculas de fluido vecinas a los átomos de la nanopartícula cercanos a la interfaz aumenta cuando se disminuye el diámetro de la nanopartícula. Esto se refleja en una energía potencial interfacial cada vez más negativa mientras más pequeña sea la nanopartícula, lo que hace que la transferencia de calor en la interfaz sea más eficiente.

Al realizar un análisis de los modos normales de vibración de los átomos en la interfaz, observamos que al reducir el tamaño de la nanopartícula su espectro incrementa su amplitud y las frecuencias menores

se exacerban. Ya que el espectro de los oxígenos tiene una mayor amplitud en frecuencias menores, esto ayuda a explicar y entender el porque de el mejoramiento en el transporte térmico al disminuir las dimensiones de la nanopartícula al existir un mejor emparejamiento entre los modos de vibración. Al calcular el espectro térmico del transporte de calor interfacial, confirmamos que son las frecuencias menores, < 3.2 THz, las que dominan el transporte térmico en la interfaz nanopartícula-medio acuoso. A su vez, determinamos que los modos anarmónicos son menos relevantes en el transporte térmico cuando la humectación nanopartícula-medio acuoso es más fuerte.

Por otro lado, al considerar un calentamiento de la nanopartícula lo suficientemente sustancial como para generar una transición de fase del líquido circundante observamos lo siguiente. El fenónemo de nucleación-cavitación del fluido depende fuertemente del tipo de humectación en la interfaz. Por ejemplo, la temperatura mínima del fluido para que se presente la cavitación depende del tipo de humectación, y esta disminuye mientras más débil sea la humectación. Incluso esta temperatura puede estar 100 K por debajo de la temperatura spinodal del agua cuando consideramos una humectación débil. Este resultado está en contraste con la creencia común de que el fenómeno de cavitación alrededor de nanopartículas plasmónicas es un fenómeno de descomposición spinodal. También observamos que la nucleación del fluido que rodea a la nanopartícula es un fenómeno lento en comparación con el tiempo típico para la difusión del calor en el bulto. La nucleación está controlada por una disminución de la conductancia térmica interfacial previo a la cavitación, lo que genera que el transporte térmico entre la nanopartícula y el fluido sea cada vez menos eficiente y sea necesario un tiempo mayor para alcanzar la nucleación.

Al tomar en cuenta los factores de tamaño y geometría en el fenómeno de la cavitación, observamos que estos también tienen un papel relevante. Existe un tamaño mínimo de la nanopartícula para que haya nucleación que depende del tipo de humectación y del tipo de fluido. Mientras más fuerte sea la humectación, más pequeña la nanopartícula para que cavite el fluido. A su vez, mostramos que la temperatura mínima para que se presente la nucleación depende también del tamaño y de la geometría de la nanopartícula. Por último, mostramos que existen diferentes escenarios en función de la energía suplida a la nanopartícula. Estos escenarios son: i) no-cavitación y no-fragmentación de la nanopartícula, ii) cavitación y parcial fragmentación y iii) cavitación y fragmentación total. Los valores específicos a los que estos escenarios suceden dependen de la geometría y la humectación de la nanopartícula.

French version

L'objectif de cette thèse peut être résumé en deux points : le premier consiste à tester la thermodynamique pour des systèmes loin de la limite thermodynamique, c'est-à-dire lorsque $N \to \infty$ et $V \to \infty$ ne sont pas satisfaits. À cette fin, nous utilisons des simulations de dynamique moléculaire pour un système de 126 molécules d'eau où les interactions inter- et intra-moléculaires sont simulées par des calculs de DFT et sont contenues dans un volume de quelques nm. Nous proposons également une méthodologie pour confiner des systèmes moléculaires où des conditions isobariques sont simulées avec une meilleure correspondance à la réalité physique. Ce système confiné consiste en un couvercle mobile une description atomistique mobile qui exerce une force constante sur le fluide, similaire à un piston qui confine un fluide en exerçant une pression constante.

Nous mesurons différents paramètres thermophysiques du système de quelques dizaines de molécules d'eau en utilisant principalement des concepts thermodynamiques. Les valeurs que nous obtenons sont généralement de l'ordre de grandeur attendu selon les données expérimentales. Cela nous conduit à conclure que la thermodynamique reste valable même pour des systèmes de quelques dizaines de molécules contenues dans un volume de quelques nm^3. En ce qui concerne la méthodologie proposée pour simuler des conditions isobariques en dynamique moléculaire, nous constatons que les densités auxquelles le système s'équilibre correspondent quantitativement aux valeurs expérimentales suivant la température et la pression imposées dans la simulation. Cela, combiné avec les valeurs des paramètres

thermophysiques que nous avons mesurés pour ce petit système d'eau, nous permet de conclure que la méthodologie est efficace pour simuler des conditions isobariques dans les calculs de dynamique moléculaire. Cependant, certains facteurs doivent être améliorés pour rendre la méthode plus efficace du point de vue computationnel.

Le deuxième sujet de la thèse consiste à étudier les propriétés de transport thermique entre des nanoparticules métalliques et un milieu aqueux. Pour cela, nous utilisons principalement des simulations de dynamique moléculaire en utilisant des calculs classiques. Les systèmes moléculaires consistent en des centaines de milliers d'atomes. Plus spécifiquement, nous considérons des nanoparticules de différentes tailles, géométries et mouillage immergées dans un cube d'eau. Nos simulations reproduisent des expériences dans lesquelles des nanoparticules plasmoniques dispersées dans un milieu aqueux sont chauffées par irradiation laser.

En considérant un chauffage modéré de la nanoparticule de sorte qu'il ne génère pas de transition de phase du liquide environnant, nous observons ce qui suit. Le transport de chaleur est plus efficace en réduisant la taille de la nanoparticule, quel que soit le type de mouillage à l'interface nanoparticule-milieu aqueux. Cela est observé en mesurant la conductance thermique interfaciale, qui montre que sa valeur augmente lorsque le rayon de la nanoparticule diminuer. Pour expliquer ce comportement, nous analysons différents paramètres physiques et observons que le nombre de molécules de fluide voisines des atomes de la nanoparticule proches de l'interface augmente lorsque le diamètre de la nanoparticule est réduit. Cela se reflète par une énergie potentielle interfaciale de plus en plus faible lorsque la nanoparticule est plus petite, ce qui rend le transfert de chaleur à l'interface plus efficace.

En analysant les modes normaux de vibration des atomes à l'interface, nous observons que la réduction de la taille de la nanoparticule augmente l'amplitude de son spectre et exacerbe les fréquences les plus basses. Étant donné que le spectre des atomes d'oxygènes a une plus grande amplitude à des fréquences plus basses, cela aide à expliquer et à comprendre l'amélioration du transport thermique lorsque les dimensions de la nanoparticule sont réduites en raison d'un meilleur accord entre les modes de vibration. En calculant le spectre thermique interfacial, nous confirmons que les fréquences les plus basses, < 3.2 THz, dominent le transport thermique à l'interface nanoparticule-milieu aqueux. Nous déterminons également que les modes anharmoniques sont moins pertinents pour le transport thermique lorsque le mouillage nanoparticule-milieu aqueux est plus forte.

D'autre part, en considérant un chauffage de la nanoparticule suffisamment important pour générer une transition de phase du liquide environnant, nous observons ce qui suit. Le phénomène de nucléation-cavitation du fluide dépend fortement mouillage l'interface. Par exemple, la température minimale du fluide pour que la cavitation se produise dépend du type mouillage et elle diminue plus le mouillage est faible. Cette température peut même être inférieure de 100 K à la température spinodale de l'eau lorsque le mouillage est faible. Ce résultat est en contraste avec la croyance commune selon laquelle le phénomène de cavitation autour des nanoparticules plasmoniques est un phénomène de décomposition spinodale. Nous observons également que la nucléation du fluide qui entoure la nanoparticule est un phénoméne lent par rapport au temps typique de diffusion de la chaleur. La nucléation est contrôlée par une diminution de la conductance thermique interfaciale avant la cavitation, ce qui rend le transport thermique entre la nanoparticule et le fluide de moins en moins efficace et nécessite un temps plus long pour atteindre la nucléation.

En ètudiant les effects de taille et de géométrie par le phénomène de cavitation, nous constatons qu'ils ont également un rôle important. Il existe une taille minimale de nanoparticule pour qu'il y ait nucléation, qui dépend du type mouillage et du type de fluide. Plus mouillÃ© est forte, plus petite est la nanoparticule pour que le fluide cavite. De même, nous montrons que la température minimale pour que la nucléation se produise dépend également de la taille et de la géométrie de la nanoparticule. Enfin, nous montrons qu'il existe différents scénarios en fonction de l'énergie fournie à la nanoparticule. Ces scénarios sont : i) pas de cavitation ni de fragmentation de la nanoparticule, ii)

cavitation et fragmentation partielle et iii) cavitation et fragmentation totale. Les valeurs spécifiques auxquelles ces scénarios se produisent dépendent de la géométrie et du mouillage de la nanoparticule.

English version

The objective of this thesis can be summarized in two points. The first consists in testing thermodynamics for systems far from the thermodynamic limit, that is, when $N \to \infty$ and $V \to \infty$ are far from being satisfied. For this purpose, we use Molecular Dynamics simulations for a system of 126 water molecules where inter- and intra-molecular interactions are simulated with DFT calculations which are contained in a volume of a few nm^3. In turn, we propose a methodology for confining molecular systems in which isobaric conditions are simulated in line with physical reality. This confined system consists of a cover that is mobile and exerts a constant force on the fluid, similar to a piston that confines a fluid by exerting constant pressure.

We calculate different thermophysical parameters of the system of a few dozen water molecules using mainly thermodynamic concepts. The values we obtain are generally in the expected order of magnitude according to experimental data. This leads us to conclude that thermodynamics is still valid even for systems of dozens of molecules contained in a volume of a few nm^3. Regarding the proposed methodology for simulating isobaric conditions in Molecular Dynamics, we find that the densities at which the system equilibrates correspond quantitatively to experimental values according to the temperature and pressure imposed in the simulation. This, together with the values of the thermophysical parameters we measure for the small water system, allows us to conclude that the methodology is effective for simulating isobaric conditions in Molecular Dynamics calculations. However, some factors need to be improved to make the method more efficient from a computational point of view.

The second subject of the thesis is to study the thermal transport properties between metallic nanoparticles and an aqueous medium. To this end, we mainly use Molecular Dynamics simulations using classical calculations. The molecular systems consist of hundreds of thousands of atoms. Specifically, we consider nanoparticles of different sizes, geometries, and wettability immersed in a cube of water. Our simulations model experiments in which plasmonic nanoparticles dispersed in an aqueous medium are heated by irradiation of a laser.

When considering moderate heating of the nanoparticle that does not generate a phase transition of the surrounding liquid, we observe the following. Interfacial heat transport is more efficient when reducing the size of the nanoparticle regardless of the wettability at the nanoparticle-water interface. This is concluded by calculating the interfacial thermal conductance, which shows that its value increases when reducing the nanoparticle radius. In order to explain this behavior, we analyze different physical parameters. The number of neighboring fluid molecules to the atoms of the nanoparticle increases when the size of the nanoparticle is reduced. This is reflected in more negative values of the interfacial potential energy, which makes thermal transport more efficient.

By analyzing the normal modes of vibration of the atoms at the interface, we observe that as the size of the nanoparticle is reduced, the amplitude of the spectrum is increased and the lower frequencies are exacerbated. Since the oxygen spectrum has a greater amplitude at lower frequencies, this helps to explain and understand the improvement in thermal transport when reducing the dimensions of the nanoparticle by displaying better matching between vibration modes. By calculating the interfacial thermal spectrum, we confirm that low frequencies, < 3.2 THz, dominate thermal transport at the nanoparticle-water interface. At the same time, we show that anharmonic modes are less important in thermal transport when the nanoparticle-aqueous medium wetting is stronger.

On the other hand, when considering a strong heating of the nanoparticle sufficient to generate phase transition of the surrounding liquid, we observe the following. The phenomenon of nucleation-cavitation of the fluid strongly depends on the wettability of the interace. For example, the minimum temperature

of the fluid to start cavitation depends on the contact angle, and it decreases as the wetting becomes weaker. This temperature can be even 100 K below the spinodal temperature of water for weak wetting. This result is in contrast to the common belief that cavitation phenomenon around plasmonic nanoparticles is a spinodal decomposition phenomenon. We also observe that nucleation of the fluid surrounding the nanoparticle is a slow process compared to the typical time governing heat diffusion in bulk water. Nucleation is controlled by a decrease in the interfacial thermal conductance prior to cavitation, which makes thermal transport between the nanoparticle and the fluid less efficient and explains the slow nucleation kinetics.

Studying the effects of size and geometry in the cavitation phenomenon, we observe that they also play a relevant role. There is a minimum nanoparticle size for nucleation to occur that depends on wetting and the type of fluid. The stronger the wetting, the smaller the nanoparticle needed for fluid cavitation. In turn, we show that the minimum temperature for nucleation to occur also depends on the size and geometry of the nanoparticle. Finally, we demonstrate that there are different scenarios depending on the energy supplied to the nanoparticle. These scenarios are: i) no cavitation and no fragmentation of the nanoparticle, ii) cavitation and partial fragmentation, and iii) cavitation and total fragmentation. The specific values at which these scenarios occur depend on the geometry and wetting of the nanoparticle.

Contents

Chapter 1

Introduction

Thermodynamics is the branch of physics that studies heat and other forms of energy. Its beginnings have been mainly phenomenological, and it is considered that it was born as a topic of science with the works of Sadi Carnot, *Reflections on the motive energy of fire*, in 1824. Thermodynamics is based on four fundamental postulates that fall into the category of laws.

The law zero of the thermodynamics, is about thermodynamic equilibrium which must be satisfied for the entire apparatus of thermodynamics to be valid, and conceptualizes the existence of a thermodynamic variable that we call *temperature*. More explicitly, the zeroth law of thermodynamics states that if a system A is in contact and thermodynamic equilibrium with a body B, and that if a body C is in contact and thermodynamic equilibrium with body B, then system A and C are also in thermodynamic equilibrium even though they are not in contact. This establishes that systems A, B, and C have a thermodynamic variable in equilibrium, and we call it temperature.

The first law of the thermodynamics, deals with the existence of a thermodynamic variable called *internal energy*. In turn, it defines the existence of a quantity called *heat*, which is a form of energy in transition that can also be converted into work. The discover, that heat can be converted into work, gave rise to the industrial revolution and massive industrialization that in turn brought social and political changes to humanity. This technological revolution is encoded in a simple equation that contains three terms:

$$\Delta U = \Delta Q + \Delta W. \tag{1.1}$$

The term ΔU is the internal energy of the system that can change if we extract or supply heat ΔQ and/or if we do work ΔW on the system or if the system does work.

The second law of the thermodynamics, deals with the existence of another thermodynamic variable named *entropy*. This thermodynamic quantity establishes that for a closed and isolated system, the state of minimum energy and thermodynamically stable of the system is the one that maximizes the value of entropy. The definition of the entropy ΔS for a reversible process is the following:

$$\Delta S = \frac{\Delta Q}{T}. \tag{1.2}$$

Finally, the third law of thermodynamics, deals with the impossibility of reaching absolute zero temperatures. More specifically, the third law of thermodynamics states that the change in entropy of the system is zero in the low temperature limit, that is:

$$\lim_{T \to 0} \Delta S = 0, \tag{1.3}$$

so, it is not possible to supply or extract heat when working with temperatures close to absolute zero.

Apart from the postulates of the thermodynamics, there is also a thermodynamic limit, which establishes the validity of the theory taking into account the dimensions of the system. In general, this limit

establishes that the number of particles N that make up the system and the volume V it occupies is very large and tends to infinity, that is, $N \to \infty$ and $V \to \infty$. In turn, it must be satisfied that the density of the system ρ is a finite quantity, that is, $N/V \to \rho$. When dealing with macroscopic systems, these definitions are easily satisfied, since common systems consist of several Avogadro's numbers of particles contained in a sufficiently large volume compared with the typical volume occupied by one particle. However, when dealing with small systems, the thermodynamic limit is somewhat ambiguous when applied. Actually, thermodynamics does not establish a lower limit at which it ceases to be valid, which leaves many questions when trying to apply it to systems with few molecules only.

Thermodynamics originally ignored the existence of atoms and molecules and was only based on the measurement of extensive variables, such as mass or volume, and intensive quantities such as pressure or temperature. It was not until the end of the 19th century that most of the scientific community began to accept the existence of atoms and molecules, and that they made up matter. This opened the need to understand thermodynamics no longer from a macroscopic point of view, but from a microscopic point of view, in which the existence of these small bricks of matter is taken into account. As a result of this, statistical mechanics arises, a branch of physics that is responsible for studying the thermodynamic properties of a system, taking into account that matter is made up of atoms and molecules.

Statistical mechanics allows establishing a connection between the atomistic properties with the laws of thermodynamics. It uses the tools offered by probability theory to deduce the behavior of a physical system, taking into account that the system is made of atoms and molecules. As in the case of the thermodynamic limit, we need a sufficient number of atoms and molecules to be able to do statistics on them. When the thermodynamic system is in thermal equilibrium, we can consider that it is possible to divide the system into subsystems in the phase space that have their own thermodynamic state, and that these subsystems form an ensemble that characterizes the total system. It is to this ensemble that statistical mechanics applies probability theory and deduces physical characteristics of the system. For this, statistical mechanics assumes that the energy states accessible by the subsystems obey a certain probability distribution function that depends on the conditions of the system.

The use of probability distribution functions arises from the fact that macroscopic systems are composed of a very large number of particles that is in the order of Avogadro's number. Due to this, using Newton's laws of mechanics on each particle that makes up the system and thereby studying its evolution becomes a titanic task. However, today it is unclear what the transition is like from a deterministic system where the positions and velocities of each atom in the system are described by Newton's second law, to one in which, a priori, individual behavior is irrelevant, and it is governed by a stochastic evolution. In this last case what matters is the collective behavior of macroscopic variables than individual behavior of each atom of the system.

Due to the rise of nanosciences during the last decades, it has been of great interest to study the properties of matter on scales of a few nanometers. It has been shown that on scales of a few nanometers, matter can behave very differently from what it exhibits on the macroscale, and many researchers have taken on the task of studying and characterizing matter at the nanoscale [1–4]. In this sense, the thermodynamic properties of systems with few molecules occupying a volume of a few nanometers have been studied. In many of these works, the validity of thermodynamics is implicitly assumed even when $N \to \infty$ and $V \to \infty$ are far from being satisfied. In this sense, the questions arise: What is the minimum number of molecules for which thermodynamics is still valid? What are the dimensions that these molecules must occupy?

We know that the atoms and molecules that make up a thermodynamic system obey, as a sufficient approximation, Newton's laws. From this, it follows that it should be possible to find a direct connection between Newton's laws of mechanics applied to each atom that constitutes the system and the laws of thermodynamics, without the need to invoke a probability distribution function. Molecular Dynamics

(MD) is the scientific method to simulate the interaction of atoms. MD allows us to define the type of molecular interaction that characterizes the system, which can be represented by means of classical or quantum potentials. In essence, it is possible to establish Newton's second law for each atom that makes up the system, where the force on atom i depends on the interaction with the other atoms in the system. Since the number of differential equations to solve increases proportionally with the number of atoms in the system, it is necessary to carry out the calculations with the support of computers. The continuous technological advance in computing systems has made it possible to study a considerable number of atoms, that it is in the order of 10^4 for conventional computer systems and in the order of $10^5 - 10^6$ for supercomputing centers. Although these numbers are still far from Avogadro's number, have allowed obtaining valuable information on small systems.

An important characteristic of MD is that it can be equally applied to systems in thermodynamic equilibrium, as to systems that are driven far out of thermodynamic equilibrium. This is due to the fact that MD have atomistic origin, which makes it a solid technic since it comes from more basic physical atomistic considerations of the system in which, a priori, the thermodynamic properties of the entire system are irrelevant. It means, thermodynamic laws come from atomistic considerations where inter and intra molecular interactions are taken explicitly into account.

In this regard, MD opens the possibility of answering the questions: What are the minimum dimensions of a system in which thermodynamics is still valid? What is the direct connection between the Newton's laws and the laws of thermodynamics? To this end, various works have been developed to try to answer these questions in a direct or indirect way. The validity of thermodynamics has recently been demonstrated for a nanometer system consisting of a few tens of water molecules confined within a fullerene molecule [5]. Classical atomistic calculations were used in this work. The methodology of this previous work consists in the variation of the volume of the system using different fullerene molecules and measuring different thermal properties of the system. Although the methodology allows testing thermodynamics for a nanometric system in a good way, it does not allow controlling all the thermodynamic variables of interest. For example, this previous methodology does not allow knowing the system pressure directly, which is obtained by adjusting the parameters of an analytical function derived from thermodynamics considerations.

Pressure control is an important factor in a large number of phenomena. In this way, different MD methodologies have been established to be able to simulate phenomena under isobaric conditions, and some of them are the following. The Berendsen thermostat controls the pressure by changing the volume with an increment that is proportional to the difference betweem the internal pressure and pressure in a weakly coupled bath [6]. Although this barostat equilibrates efficiently, it does have problems obtaining the specific characteristics in an NPT ensemble, and induces artifacts into simulations of in-homogeneous systems.

Andersen proposed a methodology to control the pressure using an extended system variable, which refers to include an additional degree of freedom corresponding to the volume of a simulation cell which is adjusted itself to equilibrate the internal and the external pressure [7]. In this method, it is added an additional degree of freedom that can be interpreted as a fictitious or virtual wall of mass M that is movable and encloses the system in a variable volume V. It is through this virtual wall by means of which the conditions for the desired pressure are imposed. This artifice is introduced as a scaling in the position of the system particles through a Lagrangian. Although it is possible to obtain a distribution function that represents the isobaric-isothermal ensemble using virtual concepts, the Lagrangian that describes the system does not have a consistent physical interpretation. Even Andersen accepts and warns of this in his work, and in his words he says "*Despite the absence of a consistent physical interpretation, the Lagrangian proposition gives a well-defined Lagrangian, and we now analyze the dynamics it generates*". The Parrinello-Rahman barostat, the Nose-Hoover barostat, and the Martyna-Tuckerman-Tobias-Klein barostat, all are based on the Andersen methodology. Furthermore, the Hamiltonian equations obtained with the Lagrangian from Andersen methodology and its variations

are not canonical, in the mechanical classical sense, because they do not preserve Hamilton's equations under transformations, and only emphasizes satisfying a distribution function related with the ensemble targetted that seeks to simulate.

Because of this, we propose a different method to establish a fixed pressure in atomistic simulations. The method makes use of basic physics and concepts that are taught in basic classical mechanics courses, where pressure P is defined as the ratio of a force F on a surface with a given area A, $P = F/A$ (Pascal's principle). In fact, it is under this principle that many pressure is gauged in the laboratory or industry work, measuring the force of the molecular tapping of a substance on the sensor and dividing it by its area. In addition, we want avoid, as possible, the use of fictitious particles, distribution functions, and all the mathematical complexity that this entails. The proposed method is more intuitive and has a direct connection to how pressure is measured in a laboratory.

In order to test our methodology, we use a nanometer test system consisting of a few tens of water molecules confined in a test tube which is simulated by means of exponential potentials and covered at one end. This cover has an atomistic-type structure and fulfills the role of a movable piston that exerts a constant pressure on the confined fluid. In addition, intra and inter molecular interactions of water molecules are simulated taking into account quantum considerations using density functional theory (DFT). The idea is to calculate different thermodynamic properties of the system and compare them with the experimental and literature results, in order to validate both the proposed method and the laws of thermodynamics on small scales.

Throughout the discussion above, we have been talking about systems that are in thermodynamic equilibrium. Actually, for the entire apparatus of thermodynamics to apply, it is necessary to deal with systems in thermal equilibrium. One of the implicit assumptions from the previous discussion is that thermodynamic variables such as volume, temperature, etc., remain constant over time for systems in equilibrium. When the system is driven out of thermodynamic equilibrium due to a perturbation, there begins to be flows of energy, mass, etc., within the system in order to bring it to the equilibrium again. The values of volume, temperature, etc. are not constant anymore until reached the equilibrium. In these systems it is not possible to directly apply the postulates of classical thermodynamics since the thermodynamic variables can vary in space and time. It is the flow of energy, mass, etc., and their derivatives that concerns the study of out of equilibrum thermodynamic systems. Since in nature and in practical situations it is more common to find phenomena out of equilibrium than in equilibrium, it becomes necessary to consider the study of this type of systems. In a very general way, when a system leaves equilibrium, the region with the highest energy gives up a part of its energy to the region with the lowest energy in order to reach equilibrium.

There are various physical phenomena in non-equilibrium that occur in practical situations that make them interesting to study. In our case, we are interested in studying matter and its properties at the nanoscale. An example of a common system where nanoscale effects are very relevant are colloidal systems. In this type of system, the interfacial area is relatively large, so the properties of the colloidal system are closely related to the interfacial properties of the phases in contact. Hence, the interfacial thermal properties are what largely define the thermal properties of the colloid. For this reason, transport at nanoscale interfaces is of great interest to be studied, and also because of the numerous applications that this phenomenon has.

In recent decades, interest in studying the properties of plasmonic nanoparticles has increased due to their diverse areas of applications. Plasmonic nanoparticles are nanoparticles whose electron density can couple with electromagnetic radiation of wavelengths that are far larger than the particle, unlike in a pure metal where there is a maximum limit on what size wavelength can be effectively coupled based on the material size [8].

Understanding the way in which heat is transferred from a plasmonic nanoparticle to the surrounding

liquid in a suspension, is of great interest for numerous technological applications. It is easy to heat up plasmonic nanoparticles that are dispersed in an aqueous medium using lasers in the visible spectrum. When irradiating a suspension of plasmonic nanoparticles in an aqueous medium with a visible light laser, the light beam is weakly absorbed by the liquid. However, when the light beam interacts with the plasmonic nanoparticles, the plasmon absorbs the laser energy and enters into resonance, which leads to heating of the nanoparticle. Fig. 1.1 shows the absorption spectrum considering different sizes of the plasmonic nanoparticle.

Due to the high electronic susceptibility of the metallic nanoparticles, the irradiated nanoparticles may see their temperature increase by hundreds of Kelvins in a picosecond-nanosecond time scale, creating nanoscale localized sources of heat in liquid water which can be used to create metastable liquid states, or practical purposes [9, 10]. For example, it is possible to obtain and study metastable states of the liquid that surrounds the nanoparticle and learn more about its nature [11, 12]. As for of potential applications encompass thermal management of liquids, mass transport [13, 14], drug delivery [15], oil recovery [16], pollutant reduction in buildings [17], solar energy conversion [18], among other important topics [16, 19, 20]. All these applications explains the increased interest in the last two decades in the thermophysical properties of plasmonic nanoparticles dispersed in a liquid environment.

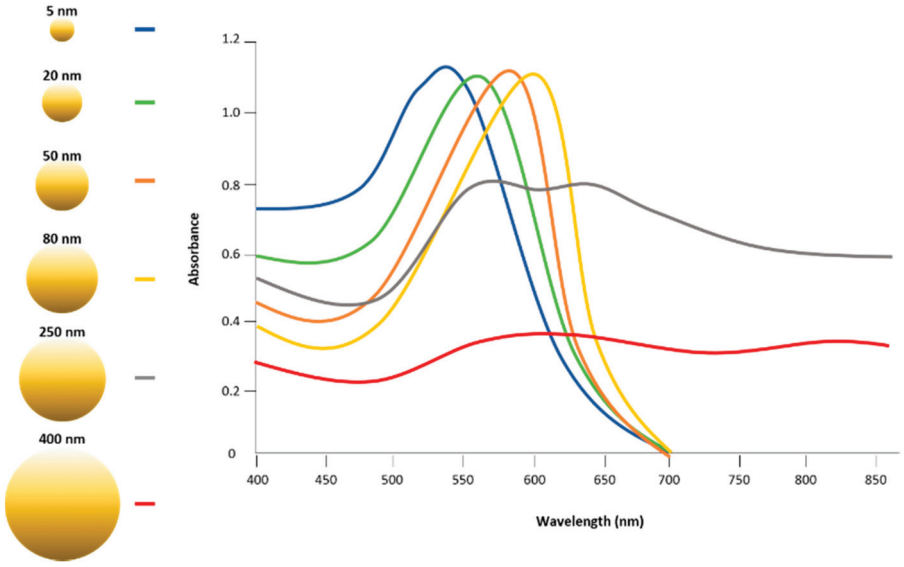

Figure 1.1: Absorption spectra of gold nanoparticles with diameters from 5 to 400 nm. It is observed that for nanoparticles smaller than 200 nm they have resonance in their plasmon in the UV-visible spectrum. Image taken from the following reference [21].

A fundamental understanding of thermal transport at the nanoscale presents significant experimental challenges due to, both, the small spatial dimensions and the short time scales relevant to the phenomena. These challenges have been addressed by different groups by employing time-resolved optical techniques, where the colloidal nanoparticles are initially heated up by a short-pulse laser. The nanoparticle temperature kinetics may be followed by either pump-probe time-resolved reflectance or by X-ray scattering, which can also give evidence of the loss of the nanoparticle crystallinity due to the laser heating [11].

Under moderate excitation, it is found that the heat transfer from the nanoparticle to its water environment is well described by the continuous heat transfer equations, supplemented with a finite *interfacial thermal conductance*, G_{K} [11]. The interfacial thermal conductance G_{K} is a quantity that allows us to analyze how efficient is the thermal transport at an interface. This parameter relates the heat flux at an interface, with the jump in the temperature value at the interface. More specifically,

we have the following relation that defines the interfacial thermal conductance G_{K}:

$$\mathbf{J} \cdot \widehat{n} = G_{\mathrm{K}}(T_{int}^{(1)} - T_{int}^{(2)}) \tag{1.4}$$

with $\mathbf{J} \cdot \widehat{n}$ the interfacial heat flux in a direction perpendicular to the interface. $T_{int}^{(1)}$ and $T_{int}^{(2)}$ are the temperatures at the interface of the phases 1 and 2 and $T_{int}^{(1)} - T_{int}^{(2)}$ is the temperature jump at the interface. This temperature jump is represented in the Fig. 1.2. Typical values of G_{K} are in the range of $10 - 300$ MW m^{-2} K^{-1}, and depend on several characteristics, including the nature of the nanoparticles [22], their shapes [23], the presence of surfactants [23,24], their wetting properties [25,26], and the chemical nature of the solvent [22, 27] as well.

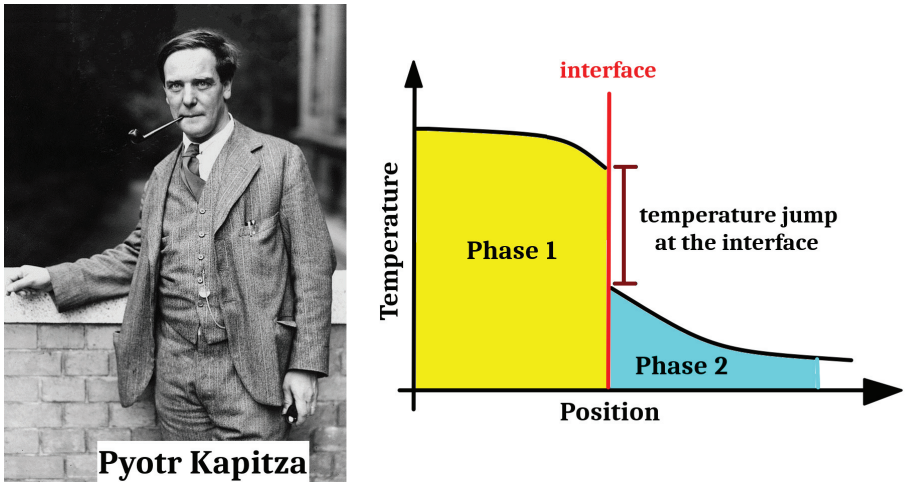

Figure 1.2: Right: temperature jump at an interface that can be characterized by the interfacial thermal conductance G_{K} defined in Eq. 1.4. Left: a photo of Pyotr Kapitsa who was the first to unveil this temperature jump at an interface when working with superfluid helium in contact with metals at temperatures close to superfluidity [28].

Concurrently, thermal transport around hot colloidal nanoparticles has been modeled using Molecular Dynamics simulations. Early studies concentrated on small nanoparticles dispersed in water [29–31], while more recent works have considered extreme heating conditions [32,33]. The thermal conductance at the interface between the gold nanoparticle and water has been shown to depend on the interface wetting properties [34]. The nanoparticle curvature is a parameter which also plays an important role in interfacial heat transport [35–37]. Different qualitative results have been obtained so far: for gold nanoparticles immersed in a Lennard-Jones fluid, the conductance G_{K} is found to increase with the nanoparticle curvature [36], while the opposite behavior is observed for gold nanoparticles in toluene [35]. The size-dependence of the interfacial heat transfer process has been characterized beyond the colloidal nanoparticle systems, including nanocrystal arrays at the organic-inorganic interface [38], octane droplets in water [39], and bubbles [40]. The size dependence of the thermal conductance $G_{\mathrm{K}}(R_{np})$ are generally described with an empirical relation, $G_{\mathrm{K}}(R_{\mathrm{np}}) = G_0 + \delta/R_{\mathrm{np}}$ [36], where R_{np} is the nanoparticle radius, δ is a characteristic length on the order of a molecular size, and G_0 is the value for a planar surface.

Characterizing the size-dependent transport properties of the metallic nanoparticle is critical to accurately understand thermal transport in colloidal gold nanoclusters. Gold nanoclusters have diameters smaller than 2 nm, and a number of atoms typically less than 100. Presently, it is possible to experimentally synthesize metal nanoparticles with diameters down to 1 nm [41,42]. On the other side, the simulations of gold nanoclusters in water under realistic conditions are scarce in the literature, with the exception of a few studies [29, 30]. These studies do not address the size dependence of the interfacial thermal transport. However, due to fundamental purposes and potential applications, it is important to characterize heat transfer from nanobjects to their liquid environment.

Having this vision in mind, we investigate how the interfacial thermal conductance G_K depends on the nanoparticle size, and assess the predictions of the continuum model on the heat transfer of small nanobjects. To do this, we analyze in detail the thermal transport of spherical gold nanoparticles, with diameters ranging from 1 up to 8 nm, immersed in water by employing non-equilibrium molecular dynamics simulations. It is shown that the interfacial thermal conductance increases by reducing the nanoparticle size. We rationalize the size-dependent effects with a generalized acoustic model, where the interfacial bonding increases with the nanoparticle curvature. A thermal spectrum analysis allows us to determine the vibrational modes with major contributions to the interfacial heat transfer, and explore the vibrational coupling changes of the gold nanocluster-water interface with the nanoparticle size. Also, we consider the description of a continuum model of the heat transfer process between the heated nanoparticle and surrounding water.

These previous considerations cases correspond to the case where the energy flowing from the nanoparticle to the liquid is not high enough to generate a phase transition of the fluid. However, if the energy supplied to the nanoparticle with the pulse and then from the nanoparticle to the fluid is high enough, can be a liquid-vapor phase transition. In this case, the liquid surrounding the nanoparticle gets hot enough and the nucleation of a bubble around the nanoparticle begins. This case and the one previously considered without cavitation are represented in Fig. 1.3.

The general evolution of the bubble around the plasmonic nanoparticle is to increase its size until is reached a maximum value, and then begin to collapse and disappear. This type of phenomenon that consists of bubbles immersed in a fluid in a liquid state is known as cavitation. The cavitation phenomenon has important relevance in many different physical situations and enginering problems. For example, cavitation can occur in submarine eruptions [43] or in the xylem of vascular plants [44]. Cavitation releases mechanical energy by emitting a shock wave, which can be dangerous or can be an advantage one in some cases of practical interest. To give a few examples, bubble collapse can destroy a nuclear power plant [43], or it can be used in microsurgery [45].

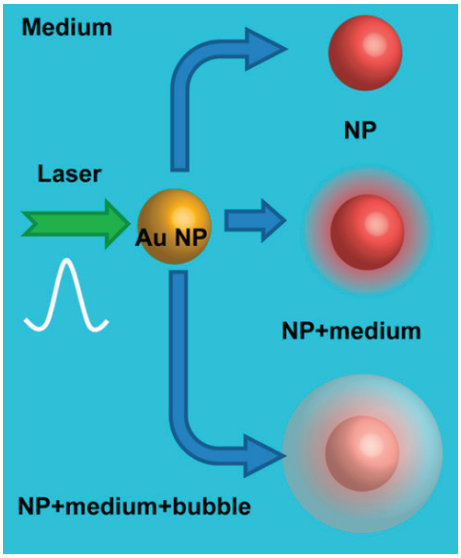

Figure 1.3: Schematic representation of the event of irradiation of the nanoparticle with a laser and the subsequent heating of the surrounding liquid. Image taken from the following reference [46].

Bubble nucleation can occur in two main ways. If the fluid is heated slowly enough and there are points that promote nucleation (small gas bubbles, corrugation, etc.), the fluid will boil normally at its boiling temperature. However, if the fluid is heated rapidly or if there is no nucleation promoters, it can reach temperatures well above its boiling temperature and remains in a metastable liquid state. In this last case, liquid-vapor phase transition from a metastable state of the liquid or when the fluid reaches the

spinodal temperature generates explosive boiling. The spinodal temperature of a fluid is at which the minimum of the Gibbs energy associated with the liquid state disappears, and only the one associated with the gaseous state exists [47]. This abrupt transition releases a huge quantity of mechanical energy.

Vapor explosion is relevant to the generation of plasmonic nanobubbles around laser irradiated nanoparticles [12, 48–52]. In turn, due to the nanoparticle interaction with its water environment, water may be heated up well above 100° its normal boiling point enabling thus to probe the behavior of metastable water. Here normal boiling does not occur as the nanoscale dimensions of the nanoparticle prevents the formation of microscale vapor nuclei and locally water may remain trapped in a metastable state. Investigating plasmonic nanobubbles is of fundamental interest for understanding the physics of phase transition at small scales and ultrafast time scales [12, 49, 51, 53].

On the more applied side, the possibility to convert light in energy has been exploited in several areas including nanoparticle assisted cancer therapy [54–56], micro and nano manipulation [57], and photoacoustic imaging [58,59]. In particular, due to their explosive nature, the generation of plasmonic nanobubbles is accompanied by the emission of intense acoustic waves which may destruct biological cellular components at a local scale [60–62]. Nevertheless, the physical mechanisms driving these phenomena are not well understood due to the difficulties to characterize the temperature field on the nanoscale and on sub-nanosecond time scales, and by the highly out-of-equilibrum conditions. This has motivated various investigations aimed at deepening our understanding of the physics of heat transfer phase change on the nanoscale.

Kotaidis et al. [12] first reported the formation of transient bubbles in an explosive way in picosecond time scales, based on time-resolved X-ray scattering experiments, when spherical Au nanoparticles are irradiated with a high intensity beam. After this seminal work, several groups investigated the generation and dynamics of nanobubbles around irradiated gold nanoparticles in different liquids [46,49, 50,52,63]. Most of these investigations concerned ultrafast laser irradiation, and continuous excitation has been considered by Orrit and coworkers [48,51]. Even in these conditions, nanobubble generation occurs explosively taking the form of transient, inertia-driven events reminiscent of the boling crisis phenomenon. Critical to these phenomena is the presence of dissolved gas which may facilitate nanobubble nucleation and affect nanobubble lifetimes as evidenced by high-speed imaging of the process [49].

The experimental effort has been accompanied by several computational modeling investigations, because both the relevant length and time scale match those accessible in atomistic simulations. Early investigations demonstrated the abscence of cavitation for small nanoparticle diameters [64–67]. The absence of cavitation for nanoparticle diameters smaller than typically 2 nm is interpreted by the huge Laplace pressure which brings the solvent locally to its supercritical state [64–66]. Nanocavitation has been observed around bigger nanoparticles wether by molecular dynamics simulations [32, 53, 68] or using phase field simulations [69, 70]. In particular, recently Pu et al. found, by considering a generic LJ fluid, that nanobubbles are generated faster around superhydrophobic nanoparticles as compared to superhydrophilic particles, indicating wetting effects on cavitation generation [32].

It was generally agreed that the nucleation temperature of the liquid surrounding the heated nanoparticle is the spinodal temperature of the fluid. In the case of water under a pressure of 1 atm the spinodal temperature is $\sim$ 573 K [47, 71]. Nevertheless, we will show in this thesis that the nucleation temperature strongly depends on the type of wetting between the nanoparticle and the fluid. We observed that while the wetting is weaker, the nucleation temperature is lower, being 100 K lower than the spinodal temperature for weak wetting. In addition, we observed that nanoparticle size and geometry factors also affect nucleation properties of the fluid.

Due to the possibility to synthesize nanoparticles having different sizes, different geometries, and different wetting, it is important to understand the influence of these parameters on the behavior of

their thermal properties. In this work, we study in detail the characteristics of the nucleation around plasmonic nanoparticles as a function of their size, geometry, and wetting of the nanoparticle. To this end, we perform non-equilibrium molecular dynamics simulations. The system of study consists of a gold-like nanoparticle immersed in water. The nanoparticle is abruptly heated periodically simulating heating by an ultra-short pulsed laser. We consider gold-like nanoparticles with different geometries, sizes, and wettability. The results show that there is a dependence of nanobubble nucleation on the size, geometry, and wetting of the nanoparticle.

Thus, we can summarize the work of this thesis in the different questions that arose during my doctoral studies. Regarding systems in thermodynamic equilibrium, it is worth asking: up to what lower limit on the number of particles and size of the system does thermodynamics still is valid? Is it possible to use methodologies in MD simulations with isobaric conditions that do not invoke artifacts that complicate the interpretation of the Lagrangian of the system? How efficient can this methodology be compared to existing ones? Regarding in the heat transport between plasmonic nanoparticles and an aqueos medium, we ask ourselves: Is it possible to study heat transfer at the nanoscale using MD simulations? What are the main characteristics in thermal transport that are modified when considering different sizes, geometries, and wetting of the nanoparticles? How does the cavitation phenomenon develop around plasmonic nanoparticles that are heated by ultra-short laser pulses? How does solving these questions help so that these types of systems can be used for practical purposes for the benefit of society? Keeping in mind these main questions, is how we work during the development of this thesis.

The thesis is structured as follows. Chapter 2 explains the objectives, which are stated in a general way in this introduction, and the hypotheses of this thesis. Chapter 3 explains the methodologies used to study the various points of interest. Chapter 3.1 deals with the methodology for the simulations retained to thermal equilibrium. It also describes the proposed method to perform isobaric simulations in molecular dynamics. Chapter 3.2 explains the methodology for the case of non-equilibrium simulations, with which thermal transport properties are studied for nanoparticle-fluid interfaces.

Chapter 4 presents the data concerning the testing of thermodynamics for nanometric systems of a few tens of molecules and the barostat proposal. It is shown that the proposed barostat gives densities close to the experimental value for the imposed temperature and pressure conditions. Furthermore, we show that for a system of a little more than 100 water molecules simulated with DFT and confined in a nanometer volume, their thermal properties are close to the experimental bulk values.

Chapter 5 presents the data regarding the study of the effect of nanoparticle size on interfacial thermal transport under moderate heating. In Chapter 6 the results on the phenomenon of cavitation around plasmonic nanoparticles immersed in an aqueous medium are presented. We show that the characteristics of the nucleation phenomenon strongly depend on the type of wetting, the size, and the geometry of the nanoparticle. This is in contrast to the common belief that it is the spinodal temperature that must be reached for cavitation to occur around plasmonic nanoparticles.

Finally, Chapter 7 presents the conclusions reached in this work. It is concluded that thermodynamic is still valid for systems of a few tens of molecules in a nanometric volume. Regarding the interfacial thermal transport at the nanoscale, it is concluded that its properties relatively increase by decreasing the dimensions of the nanoparticle is due to a better bonding of the interface atoms and to an exacerbation of the low vibration frequencies modes. Finally, we conclude that the phenomenon of bubble nucleation around plasmonic nanoparticles depends on the nanoparticle structure, geometry, and wetting factors, this being particularly evident for the minimum nucleation temperature.

Chapter 2

Objective and hypothesis

The objective of the thesis is to study thermal properties of matter at the nanoscale. One point is to prove the lower thermodynamic limit at which the postulates of classical thermodynamics remain valid. To this end, we use molecular dynamics simulations using a system of a few tens of water molecules in combination with a hybrid theoretical framework, provided by the density functional theory (DFT) and the laws of classical mechanics. Our hypothesis is that the postulates of thermodynamics are still valid for nanometric systems of a few tens of molecules. At the same time, we propose a methodology for Molecular Dynamics simulations under isobaric conditions using physical concepts more in line with experiments. Our hypothesis is that we can find methods for isobaric simulations in which the number of artificial effects can be reduced to achieve the desired thermodynamic conditions.

In parallel, we have the objective to study the interfacial heat transfer between metallic nanoparticles and an aqueous medium using Molecular Dynamics simulations. This study is motivated by the recent development of experiments where a plasmonic nanoparticle immersed in water is heated after the irradiation by a laser pulse. Different phenomena may occur in water due to the high level of local heating, among which water cavitation and/or nanoparticle fragmentation. The physics of these phenomena is, however, poorly understood.

In order to delve into the physics of these types of phenomena, we study different physical properties to characterize and understand the flux of heat at interfaces in the nanoscale, where experimental progress is currently difficult. The hypothesis is that we can rely on Molecular Dynamics in order to study interfacial thermal transport at the nanoscale for phenomena of interest. Following this, it is possible to assess the validity at the nanoscale of models of the continuum that seek to explain thermal transport phenomena.

Hence, we can summarize the objective of this thesis as an extension of the knowledge of the thermal properties of matter at the nanoscale, testing different methodologies and systems. We do this through the study of the thermodynamic and interfacial thermal properties for nanometric systems. Also, we seek to support the task of ensuring the practical application of nanoparticle suspensions in aqueous mediums. Finally, we want to show that we can rely on the Molecular Dynamics technique in order to answer questions of transport properties of matter at small scales.

Chapter 3

Methods

This section explains the methodologies to carry out Molecular Dynamics simulations. In general, the thesis deals with nanometric systems both in thermal equilibrium and non-equilibrium. In case of equilibrium situations, we use our own code written in Fortran and CUDA languages. In case of non-equilibrium situations, we use the open and free-source package Large-scale Atomic/Molecular Massively Parallel Simulator (LAMMPS) [72]. The reason for using different programs to perform the simulations is to test different scenarios for the execution of simulations in Molecular Dynamics.

Thus, we will divide the Methods Chapter into two sections. The first section explains the methodology used for the thermal equilibrium simulations. For this case, we use a program written by the group. The second section explains the methodology used for non-equilibrium simulations, which are performed using LAMMPS.

3.1 Systems in thermodynamic equilibrium

For this type of simulation, we consider 126 water molecules that are confined in a "test tube" with a mobile cover in one of its side. The intra and inter molecular interaction of water molecules are described using the density functional theory (DFT). The cover has an atomistic-like description and interacts with the water molecules through an exponential potential. A constant force is applied to the cover so that it acts on the water molecules with a desired pressure. In this way, we look for the way to generate and propose a methodology in which systems are simulated under isobaric conditions. The simulations are performed in thermal equilibrium, by considering conditions of fixed pressure and fixed volume. All specifications of this system and the proposed methodology for isobaric simulations are described in this section.

3.1.1 Interactions of hydrogen and oxygen atoms with density functional theory (DFT)

The interactions between water molecules and between atoms of the same water molecule are simulated with the density functional theory, DFT. We use the BLYP functional and the basis 6-31g*. For these simulations, we use the TeraChem software with mixed precision and energy convergence of 3×10^{-5} units. We have that the potential is the following:

$$V_{\text{quantum}} = V_{DFT} + \text{confinement potentials} \tag{3.1}$$

where the meaning of *confinement potentials* will be explained in later sections. The force and equations of motion for an atom i of a water molecule are as follows:

$$\mathbf{F}_i = m_i \frac{d^2\mathbf{r}_i}{dt^2} = -\nabla_i V_{\text{quantum}}. \tag{3.2}$$

Solving the previous equation for $\mathbf{v}_i$ and $\mathbf{r}_i$, we obtain the dynamics of the water molecules.

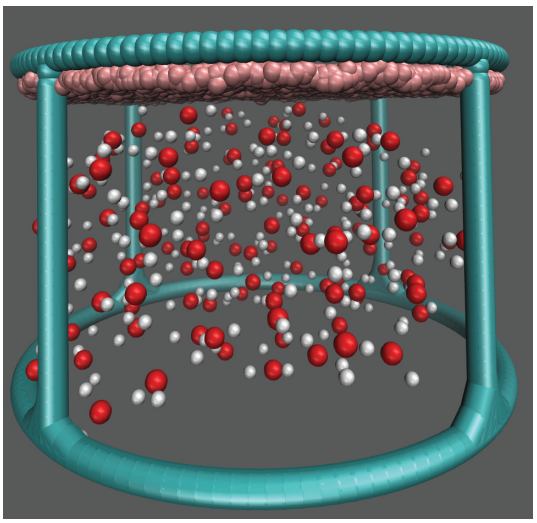

Figure 3.1: System of 126 water molecules confined in a cylindrical volume with a cover at the top. In the upper part it is the confinement cover with an atomistic-like description. The green bars are for illustrative purposes to show the boundaries of the confinement volume and they do not influence in the dynamics.

3.1.2 Cylindrical confinement potentials

The water molecules are confined in a container having a cylindrical geometry that is along the z axis, as seen in Fig. 3.1. This confinement is described by an exponential potential, it is just repulsive, and it simulates impenetrable walls at the boundaries of our simulation box, which in this case has cylindrical geometry. This potential has the following functional form:

$$V_{\text{cyl}}(r_i) = V_0 \exp\left[\alpha(r_i - R_{cyl})\right], \qquad r_i = (x_i^2 + y_i^2)^{1/2} \tag{3.3}$$

where $V_0 = 1.255$ Kcal/mol, R_{cyl} is the cylinder radius, r_i the radial distance from the cylinder's vertical axis to the i atom in a plane perpendicular to the vertical axis, and the growing rate of the potential is given by α with value 8 Å^{-1}. Fig. 3.2 shows a graph for this confinement potential, where it can be seen how the potential increases rapidly when an atom of a water molecule approaches $R_{cyl} = 10.5$ Å. Since the slope of the curve tends to infinity as we approach R_{cyl}, which is related with the force exerted by the potential $\mathbf{F}_{\text{cyl}} = -\nabla_{\mathbf{r}_i} V_{\text{cyl}}(r_i)$, it is possible through this method to confine atoms.

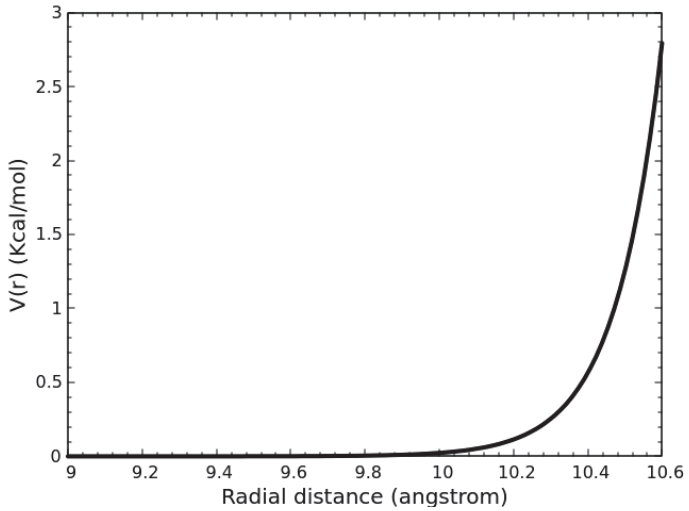

Figure 3.2: Graph of potential 3.3.

The bottom of the cylinder is also simulated with an exponential function as follows:

$$V_{\text{bottom}}(r_i) = V_0 \text{exp}[-\alpha(z_i - z_{lim})] \tag{3.4}$$

with z_{lim} the lower limit of the cylinder that in our case is -11 Å. The cylindrical confinement of the water atom i having position x_i, y_i, z_i is achieved with the sum of the previous potentials, that is:

$$V_{\text{conf}} = V_{\text{cyl}} + V_{\text{bottom}}. \tag{3.5}$$

3.1.3 Confinement cover specifications

In order to develop a methodology to perform simulations under isobaric conditions, we present a model that consists of a cover that has an atomistic-like description and is mobile. We consider a confinement of the water molecules with this cover in the top of the cylinder, with which a constant pressure is applied to the confined fluid. The details will be explained in this section.

The interaction between the atoms of the water molecules and the atoms of the cover are of exponential type, this is:

$$V_{\text{cover}}(r_{ij}) = V_0 \text{exp}\left(-\alpha r_{ij}\right) \tag{3.6}$$

with r_{ij} the distance between the water atom i and the cover atom j. The coverage has the function of exerting pressure on the system under study that is confined. This is analogous to the case where a mobile piston with a specific weight pushes on a fluid exerting a constant pressure.

This cover has an explicit structure and is simulated as follows. We consider a circular layer of atoms as the cover, and its radius is equal to the radius of the confining cylinder. Each cover's atom has the mass of a gold atom and are initially generated on a grid, where the atoms are spaced 0.15 Å apart from each other, as seen in Fig. 3.3. As can be seen in Fig 3.3, the cover's atoms are very close one from each other. The reason of this is due to the interaction potential with the confined fluid atoms, Eq. 3.6. The exponential function decays rapidly, so if the cover's atoms are spaced far apart, the cover would have "holes" through which the fluid's atoms could escape. This puts technical limitations, since increasing the radius of the cylinder increases the number of atoms quadratically. However, with the constant and recent technological advances in the area of computing, this is no longer a problem.

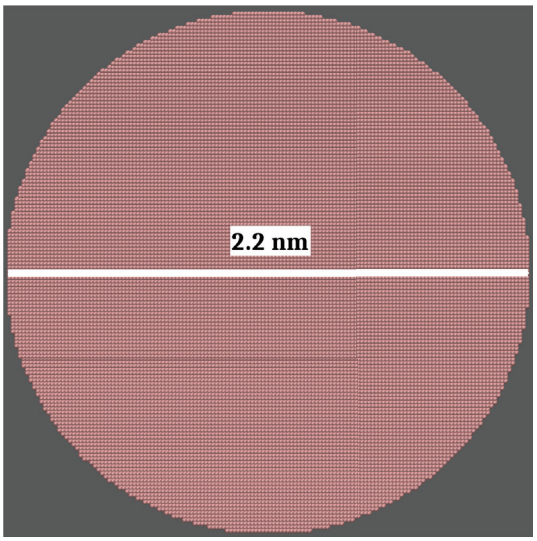

Figure 3.3: Cover with which the water molecules are confined at a constant pressure.

In order to reduce computational time, a relatively simple force field describing the interaction between

cover atoms is proposed. First, we consider harmonic interactions with the eight nearest neighbors of each atom. This is:

$$V_{hc}(r_{ij}) = \frac{k_{cr}}{2}(r_{ij} - r_{c0}^{(ij)})^2. \tag{3.7}$$

The constant $k_{cr} = 63.0$ Kcal mol^{-1}/Å^2 and the relaxation distance $r_{c0}^{(ij)}$ is the one that the cover atoms have at the beginning of the simulation, so each pair of atom i and j do not necessarily have the same relaxation distance $r_{c0}^{(ij)}$.

In order to impose the rigidity of the top cover, an exponential potential is used so that each atom in the cover is confined to its initial position in the plane x, y. The potential has the following functional form:

$$\begin{aligned} V_{cc} = V_0 \{&\exp\left[\alpha(x_i - (x_{0i} + \delta_x))\right] + \exp\left[-\alpha(x_i - (x_{0i} - \delta_x))\right] + \\ &\exp\left[\alpha(y_i - (y_{0i} + \delta_y))\right] + \exp\left[-\alpha(y_i - (y_{0i} - \delta_y))\right]\} \end{aligned} \tag{3.8}$$

with $V_0 = 1.255$ Kcal/mol, $\delta_x = \delta_y = 0.03$ Å.

Since the cover has only the role of exerting a pressure and confining the atoms of the fluid with a constant pressure, its atomistic structure is to some extent irrelevant. One could then think of simulating an explicitly gold cover where the cover has an FCC crystalline structure, for example. However, what is relevant is the interaction between the atoms of the cover and the atoms of the confined fluid, since this energy must be taken into account when calculating the thermal properties of the system, as it will be explained in more detail later. If we simulate a gold-like cover, for example, the interaction between the cover-fluid atoms is of van der Waals type. We consider a repulsive and an attractive contribution to our potential. This interaction induces structuring near the solid-liquid interface, which, although small, can affect the physical properties of the fluid when the system has nanoscale dimensions, as seen in Fig. 3.4. To plot this latter figure we consider a thermalized system, and we use water shells of 2 Å of width. This is the reason why we choose an exponential type of interaction between the cover atoms and the fluid atoms, Eq. 3.6, since this potential does not induce structuring near the interface, as seen in Fig. 3.4.

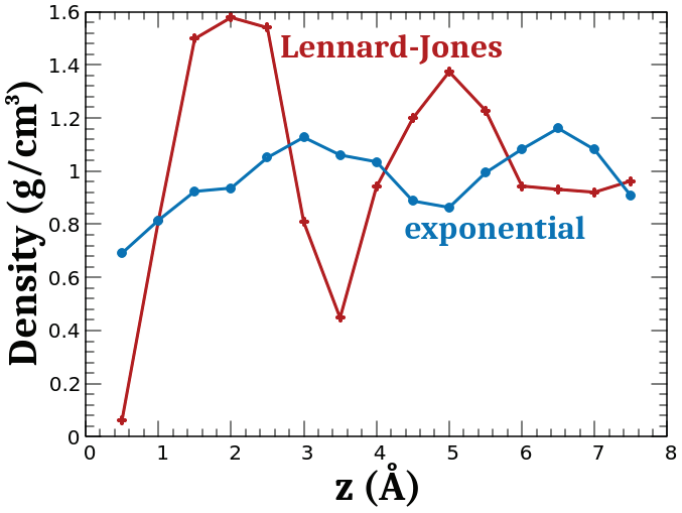

Figure 3.4: Comparison of the water density profile along the z-axis for two types of interactions with the cover atoms. The cover is located at $z \approx 0$.

Finally, we explain how we apply pressure to the confined system. For this purpose, following the idea of how pressure is measured experimentally, we make use of the definition of the mechanical pressure given by:

$$\text{pressure} = \frac{\text{force}}{\text{area}}. \tag{3.9}$$

Since we assume that Pascal's principle applies to our system, we then have that the pressure that is applied to the confined fluid through pressing with the cover, must be the same for the entire system. From the cover, we know its area and the total mass $M_c = N_c M_{\text{Au}}$, with the total number of cover atoms, $N_c = 15361$, and M_{Au} the mass of the gold atom. Taking this into account, we apply a pseudo-gravity g to the cover atoms such that it generates a weight $M_c g$ that acts on the fluid with the desired pressure P, that is:

$$P = \frac{M_c g}{\pi R_{cyl}^2}. \tag{3.10}$$

In this case, the specific value of g is 6.98528×10^{-13} fs/Å^2. Then we have that on the atoms of the cover a gravity-like potential energy is exerted that generates the desired pressure. This potential energy over the cover atom i is:

$$V_g = -m_i g z_i. \tag{3.11}$$

Hence, the potential energy of the cover atom i is the sum of Eqs. 3.6, 3.7, 3.8, and 3.11:

$$V_{\text{icov}} = V_{hc} + V_{cc} + V_{\text{cover}} + V_g, \tag{3.12}$$

where the first two terms correspond to the internal interactions of the cover atoms, the third to the interaction with the water molecules, and the fourth to the pseudo-gravity. It is worth mentioning that the fourth term, V_g, derives the force that generates the desired pressure, and the third term, V_{cover}, ensures the transmission of the force from the cover to the fluid.

The force and the equation of motion on the cover atom i is:

$$\mathbf{F}_i = m_i \frac{d^2 \mathbf{r}_i}{dt^2} = -\nabla_i V_{\text{icov}}. \tag{3.13}$$

3.1.4 System specifications and simulation methodology

In this section the details of the simulations under thermodynamic equilibrium are explained, including as the integrators, how the simulations are carried out and the data collection.

First, we have to write the incomplete terms for the potential energy V_{quantum} of the water molecules. With what was previously described about confinement potentials, we can now rewrite Eq. 3.1 with all its terms explicitly:

$$V_{\text{quantum}} = V_{DFT} + V_{\text{cyl}} + V_{\text{bottom}} + V_{\text{cover}}. \tag{3.14}$$

It is necessary to note that the potential V_{quantum} has a hybrid character, since one of its terms contains information of quantum nature coming from DFT, while the others are of classical nature. We could even include Coulomb and/or Lennard-Jones in Eq. 3.14 type interactions for the interaction with other classical atoms. This would allow simulating larger systems in which the atoms of main interest would be simulated with the DFT, and the atoms of lesser interest, which could be the surrounding medium for example, would be simulated using the classical theory.

Having discussed the previous point, we now proceed to explain the methodology retained in the simulations.

Integrators

We choose two regions according to the radial position of the atom of the water molecule, as shown in Fig. 3.5. The radius of the inner circle, that corresponds to the region occupied by Newton atoms, is 7.5 Å while the region occupied by Langevin atoms extends from 7.5 Å to the limit of the cylinder having a radius of 10.5 Å. As a consequence, the thickness of the Langevin region is 3 Å. The Langevin atoms play the role of the atoms in contact with an external thermal bath that keeps a constant temperature of the total system.

Regarding the atoms that are in the central region, their positions and their velocities are updated according to the following Eqs.:

$$\begin{aligned} v_i(t_n + \Delta t) &= v_i(t_n) + \frac{1}{2m_i}[F_i(t_n + \Delta t) + F_i(t_n)]\Delta t + O(\Delta t^2), \\ x_i(t_n + \Delta t) &= x_i(t_n) + v_i(t_n)\Delta t + \frac{1}{2m_i}F_i(t_n)\Delta t^2 + O(\Delta t^3), \end{aligned} \tag{3.15}$$

where F_i is given by Eq. 3.2. We name these atoms as Newton atoms. The previous algorithm described to evolve velocities and positions is known as Velocity-Verlet and is widely used in Molecular Dynamics simulations [73].

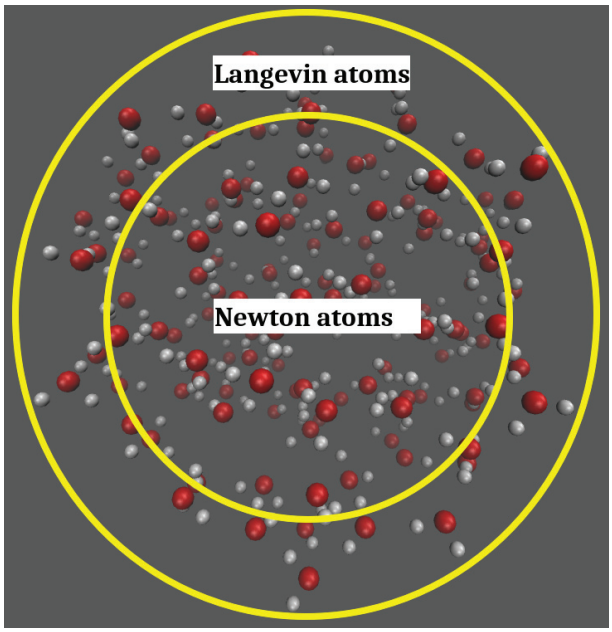

Figure 3.5: Representation of the regions considered for the algorithm of numerical integration of the velocities and positions. The yellow circles are for visualization and illustrative purposes only.

The atoms found in the Langevin region evolve according to the Langevin equation:

$$m_i\frac{d^2x_i(t)}{dt^2} + \gamma\frac{dx_i(t)}{dt} - G_i(t) - F_i(t) = 0 \tag{3.16}$$

with $\gamma dx_i(t)/dt$ is a friction force, G_i a stochastic force, and F_i is given by Eq. 3.2. The atoms that are in the Langevin region play the role of simulating the interaction with a thermal bath which maintains the system at a desired temperature, that is, they play the role of a thermostat. The velocities and positions of the atoms that are in the Langevin region evolve with the following Eqs.:

$$\begin{aligned} v_i(t_n + \Delta t) &= c_0 v_i(t_n) + (c_1 + c_2)\frac{F_i(t_n)}{m_i}\Delta t + \frac{1}{m_i}c_2 F_i(t_n + \Delta t)\Delta t + V_i, \\ x_i(t_n + \Delta t) &= x_i(t_n) + c_1 v_i(t_n)\Delta t + \frac{c_2}{m_i}F_i(t_n)\Delta t^2 + X_i. \end{aligned} \tag{3.17}$$

The values c_0, c_1, and c_2 are constants given by:

$$c_0 = e^{-\gamma\Delta t}, \qquad c_1 = (\gamma\Delta t)^{-1}(1 - c_0), \qquad c_2 = (\gamma\Delta t)^{-1}(1 - c_1). \tag{3.18}$$

The terms V_i and X_i are stochastic terms associated with the random force G_i. To calculate the stochastic terms, we use a Chandrasekhar bivariate distribution function where the correlation of velocities, positions and their product are taken into account [74]. These terms are given by:

$$X_i = \sqrt{\sigma_x^2}\eta_1, \qquad V_i = \sqrt{\sigma_v^2}\left(C_{xv}\eta_1 + \sqrt{1 - C_{xv}^2}\right)\eta_2, \tag{3.19}$$

where σ_x^2 y σ_v^2 are the variance of position and velocity, respectively. C_{ij} is the covariance between variables i and j with $i, j = x, v$. Finally, η_1 and η_2 are two independent random numbers with a Gaussian distribution with zero mean and unit variance. A more detailed derivation of Eqs. 3.17 and its related terms can be found in [74, 75].

It is important to mention that the atoms of the cover are always considered as thermostats, that is, they are always simulated with a fixed temperature using Eqs. 3.17. In this case, the force F_i on the cover atom i is given by Eq. 3.13.

Preparing the system

The time step used in all the simulations is 1 fs. We consider 126 water molecules confined in a cylinder having a radius of 10.5 Å. The height of the cylinder is variable and tends to oscillate around a constant value when the system reaches equilibrium. As mentioned above, the spacing between the cover atoms is 0.15 Å to prevent water molecules from escaping. The total number of cover atoms is 15739. We use temperatures between 275 to 350 K and a pressure of 1 atm.

After reaching a density close to 0.997 g/cm^3, we start running the simulations of interest. We let the simulation running so that it finishes the thermalization and a sufficient amount of data has been accumulated to carry out measurements of the physical parameters of interest. The typical simulation time, between equilibrating and data collection, ranges from 20 to 30 ps. We remark that for the simulation lasting 25 ps of our water system, it takes around 25 computing days with common GPUs. This puts a technical limitation that can be solved with the continuous technological advancement of the GPUs.

Calculation of the different physical quantities.

After reaching thermodynamic equilibrium, we started collecting data. The quantities of interest are the total energy U_{w} and enthalpy H_{w} of the water molecules, the density ρ_{w}, and the temperature T_w. To calculate the energy of the water molecules, we consider the following formula:

$$U_{\mathrm{w}} = \sum_i \left[\frac{1}{2} m_i v_i^2 + V^{(i)}_{\mathrm{quantum}} \right] = \sum_i \left[\frac{1}{2} m_i v_i^2 + V^{(i)}_{DFT} + V^{(i)}_{\mathrm{cyl}} + V^{(i)}_{\mathrm{bottom}} + V^{(i)}_{\mathrm{cover}} \right]. \tag{3.20}$$

The index i runs over all the atoms of the water molecules. The first term corresponds to the kinetic energy. The term $V^{(i)}_{DFT}$ comes from the DFT calculations, $V^{(i)}_{\mathrm{cyl}}$ corresponds to Eq. 3.3, $V^{(i)}_{\mathrm{bottom}}$ corresponds to Eq. 3.4, and $V^{(i)}_{\mathrm{cover}}$ to Eq. 3.6. We are careful not to count twice energies from pair interactions when calculating 3.20.

To calculate the enthalpy H_{w} we use its definition:

$$H_{\mathrm{w}} = U_{\mathrm{w}} + PV, \tag{3.21}$$

where U_{w} is given by eq. 3.20, P is the pressure of the system given by Eq. 3.10, and V is the volume of the confined system. The value of P is constant during isobaric simulations, and V varies around a constant value when the system is in equilibrium. To calculate V we use the formula $V = \pi R_{cyl}^2 h$, where R_{cyl} is the radius of the cylinder and h is the height of the system.

To obtain h, we calculate the upper and lower limits, l_u and l_l respectively, of the confined system as follows. For the upper limit l_u, we consider the 100 cover atoms that have the lowest position along the confinement axis (z in our case) and we calculate the positions of their center of mass. Then we consider the 100 atoms of the confined fluid that have the highest position along the confinement axis, and we calculate the position of their centers of mass. With these two lengths, l_u is calculated as the average of the positions of the center of mass of both groups of atoms along the confinement axis. To calculate the lower limit l_l, the 100 atoms of the confined fluid that have the lowest position along the confinement

axis are considered, and the position of their centers of mass is calculated. l_l is calculated as the average between the position of the center of mass along the confinement axis and the lower limit for the exponential confinement length z_{lim} given in Eq. 3.4. The absolute value of the difference between the upper limit and the lower limit is considered as the height of the confined system, this is $h = |l_u - l_l|$.

To calculate the mass density ρ_{w} of the system we use the definition:

$$\rho_{\mathrm{w}} = \frac{M_{\mathrm{w}}}{V}, \tag{3.22}$$

where M_{w} is the total mass of the confined water and V is the same as considered in the Eq. 3.21, and that has been previously defined.

To calculate the temperature T_{w} of the confined system, we use the following Eq.:

$$T_{\mathrm{w}} = \frac{2}{(3N_{\mathrm{aw}} - 6)k_B} \sum_i K^{(i)}. \tag{3.23}$$

The index i runs over all the atoms of the water molecules. N_{aw} is the total number of atoms of the water molecules, k_B is Boltzman's constant, and $K^{(i)} = m_i(v_{xi}^2 + v_{yi}^2 + v_{zi}^2)/2$ is the kinetic translational energy of atom i. The quantity $3N_{\mathrm{aw}} - 6$ is the number of translational degrees of freedom of the system.

The dynamics are run ~ 25 ps and the data collection time is ~ 15 ps.

3.2 Non-equilibrium simulations

The discussion in the previous section was centered around a system consisting of 126 water molecules in thermal equilibrium that are confined in a cylindrical volume. Now we will explain how Molecular Dynamics simulations are performed for systems in non-equilibrium.

Here, we study the thermal transport between a metallic nanoparticle and an aqueous medium. The nanoparticles have different sizes, geometries, and contact angles, in addition to being immersed in a pool of water. The simulations are performed using Large-scale Atomic/Molecular Massively Parallel Simulator (LAMMPS) following the methodology described in this section [72]. The time step used in all the simulations is 1 fs and all simulations are carried out with periodic boundary conditions in a cubic box.

3.2.1 Atomic and molecular structure

The water molecule is described by the TIP4P/2005-water model [76], with flexible covalent bonds OH and bond angles H-O-H. The covalent bonds and bond angles are simulated using the following harmonic potentials:

$$V_r = \frac{k_r}{2}(r - r_0)^2, \qquad V_\theta = \frac{k_\theta}{2}(\theta - \theta_0)^2, \tag{3.24}$$

whose parameters are $r_0 = 0.9572$ Å, $k_r = 600.0$ Kcal/(mol Å^2), $\theta_0 = 104.52^o$ and $k_\theta = 75.0$ Kcal/(mol rad Å). The non-bonded interactions are simulated with the Lennard-Jones (LJ) and Coulomb potentials:

$$V_{LJ}(r_{rij}) = 4\epsilon_{ij}\left[\left(\frac{\sigma_{ij}}{r_{ij}}\right)^{12} - \left(\frac{\sigma_{ij}}{r_{ij}}\right)^{6}\right], \qquad V_C(r_{ij}) = k_C\frac{q_i q_j}{r_{ij}}, \tag{3.25}$$

with $\sigma_{\mathrm{OO}} = 3.1589$ Å and $\epsilon_{\mathrm{OO}} = 0.1852$ Kcal/mol [76] for LJ potential, and the atomic charges are $q_O = 0$, $q_M = -1.1128e$, and $q_H = 0.5564e$ for oxygen, M-site, and hydrogen, respectively.

Thus, the potential energy associated with the water molecule in this case is:

$$V_{\mathrm{tip4}} = V_C + V_{LJ} + V_r + V_\theta, \tag{3.26}$$

and the force associated with the water molecule is:

$$\mathbf{F}_i = -\nabla_{\mathbf{r}_i} V_{\text{tip4}}. \tag{3.27}$$

The systems that we study consist of a gold-like nanoparticle having different geometries and sizes immersed in a pool of water. The gold-like nanoparticle has a FCC-type crystalline structure and initially occupies a volume fraction ranging from 1% to 10% of the total box volume. The volume fraction that the nanoparticle occupies depends on its size and will be specified in each case. The interactions among the gold atoms of the nanoparticle are described by the LJ potential with $\sigma_{\text{AuAu}} = 2.6290$ Å and $\epsilon_{\text{AuAu}} = 5.29$ Kcal/mol [77]. The interaction between the nanoparticle atoms and the water molecules is modeled by the LJ potential, with parameters $\sigma_{\text{NpO}} = \sigma_{\text{AuO}} = 2.8818$ Å and $\epsilon_{\text{NpO}} = \alpha\epsilon_{\text{AuO}}$, $\epsilon_{\text{AuO}} = 0.9898$ Kcal/mol. The dimensionless parameter α will be described in the next section. Both parameters σ_{AuO} and ϵ_{AuO} are given by the geometric-mean combination rule $\sigma_{ij} = (\sigma_{ii}\sigma_{jj})^{1/2}$ and $\epsilon_{ij} = (\epsilon_{ii}\epsilon_{jj})^{1/2}$ using the data from [76, 77]. The potential for the nanoparticle atom i is:

$$V_{\text{np}} = V_{LJ} = 4\epsilon_{ij}\left[\left(\frac{\sigma_{ij}}{r_{ij}}\right)^{12} - \left(\frac{\sigma_{ij}}{r_{ij}}\right)^{6}\right], \tag{3.28}$$

and the force is:

$$\mathbf{F}_i = -\nabla_i V_{\text{np}}. \tag{3.29}$$

All the interactions are truncated at a cut-of radius of $r_c = 11$ Å, and the Coulomb interactions beyond this cut-off are calculated using the Ewald summation with a precision of 1×10^{-4}.

3.2.2 Integrators

For the out of equilibrium simulations, we use the LAMMPS package, so we make use of its integrators. Basically we use 3 types of integrators that represent a microcanonical ensemble NVE, an isothermal-isobaric ensemble NPT, and an isobaric-isoenthalpic ensemble NPH. For the microcanonical ensemble, we use Eqs. 3.15 to update the positions and velocities of the atoms.

For the case where we consider the isobaric condition, we use the extended Lagrangian approach [78]. In this case, it is expanded the phase space of the particles by increasing the number of degrees of freedom in the system. In this way, we can simulate the effects of the surrounding medium on the nanoparticles with reduced computational cost. The rules governing extended phase spaces are similar to those governing real phase spaces, such as the fact that there is conservation of phase space volume [79]. The equations of motion are derived from the extended Lagrangian by applying the usual methodology of Lagrangian theory. In the extended Lagrangian, the additional degrees of freedom are associated with virtual particles that satisfy Newton-type equations of motion and are coupled with the real particles.

In general, a barostat and a thermostat impose pressure and temperature on the system by changing the distances between particles to achieve the appropriate volume and pressure, and scaling the particle speeds to reach the desired temperature. Following this general idea, two degrees of freedom are added to the Lagrangian. The degree of freedom associated with the barostat increases or decreases the interparticle distances to reach the required pressure, and the degree of freedom associated with the thermostat increases or reduces the particle speeds to attain the desired temperature. The extended Lagrangian takes the following form, considering the additional degrees of freedom with the symbols s and V:

$$\mathcal{L} = \sum_i \frac{m_i}{2} s^2 V^{2/3} \dot{q}_i^2 + \frac{M_s}{2}\dot{s}^2 + \frac{M_V}{2}\dot{V}^2 - U(\{V^{1/3}\mathbf{q}_i\}) - g k_B T_{eq} \ln s - P_{ext} V. \tag{3.30}$$

g denotes the total number of degrees of freedom of the system, which in this case is $3N+2$ independent variables, with $3N$ associated with the generalized coordinates q of the N real particles, plus the additional variables s and V. The variable V corresponds to the volume of the simulation box. The

dimensionless variable s is the thermostat variable that equilibrates the system to the temperature T_{eq}. The 'masses' M_V and M_s have the following units:

$$M_V := \text{energy} \times \text{time}^2/\text{volume}; \qquad M_s := \text{energy} \times \text{time}^2. \tag{3.31}$$

The terms containing the variables s and V play the role of an external field. However, these variables can be visualized as positions of virtual particles that have similar characteristics to real particles but with different units. That is why we can refer as the particle of the barostat to the ones described by the variable V, and the particle of the thermostat to the ones described by the variable s. The kinetic energy of these particles is given by the terms $M_V\dot{V}^2/2$ and $M_s\dot{s}^2/2$, in addition to the extended Lagrangian including the potential energy to which the virtual particles are subjected. In the case of the barostat particle, we have that the potential energy is proportional to PV, and for the thermostat particle, we have the expression $-k_BT_{eq}\ln s^g$.

The equations of motion are derived according to the Lagrangian formulation:

$$\frac{\mathrm{d}}{\mathrm{dt}}\pi_x = \frac{\mathrm{d}}{\mathrm{dt}}\left(\frac{\partial\mathcal{L}}{\partial\dot{x}}\right) = \frac{\partial\mathcal{L}}{\partial x}; \qquad x = q_i, s, V; \qquad i = 1, ..., N, \tag{3.32}$$

with $\mathcal{L}$ from Eq. 3.30. Considering the derivative with respect to time of the conjugate moment $\pi_x = \partial\mathcal{L}/\partial\dot{x}$ and taking into account the conjugate force $\partial\mathcal{L}/\partial x$, it can be shown that the equations of motion are given by:

$$\begin{aligned}
\frac{\mathrm{d}}{\mathrm{dt}}\pi_i &= 2m_is\dot{s}V^{2/3}\dot{q}_i + \frac{2}{3}m_is^2\frac{\dot{V}}{V^{1/3}}\dot{q}_i + m_is^2V^{2/3}\ddot{q}_i \\
\frac{\mathrm{d}}{\mathrm{dt}}\pi_s &= \textstyle\sum_i m_isV^{2/3}\dot{q}_i^2 - gk_BT_{eq}/s \qquad . \\
\frac{\mathrm{d}}{\mathrm{dt}}\pi_V &= \frac{1}{3V}\left[\textstyle\sum_i m_is^2V^{2/3}\dot{q}_i^2 - \sum_i q_iV^{1/3}\frac{\partial U(\{q_iV^{1/3}\})}{\partial(q_iV^{1/3})}\right] - P_{ext}.
\end{aligned} \tag{3.33}$$

The first expression gives the equations of motion for the real particles, while the second and third terms give the equations of motion for the thermostat particle and the barostat particle, respectively.

Now we proceed to calculate the Hamiltonian associated with the extended Lagrangian using Legendre transformations, as follows:

$$\begin{aligned}
\mathcal{H} = \textstyle\sum_i \dot{q}_i\pi_i + \dot{s}\pi_s + \dot{V}\pi_V - \mathcal{L}(\{q_i,\dot{q}_i\}, s, \dot{s}, V, \dot{V}) = \sum_i \frac{\pi_i^2}{2m_is^2V^{2/3}} + \frac{\pi_s^2}{2M_s} + \frac{\pi_V^2}{2M_V} \\
+U(\{q_iV^{1/3}\}) + gk_BT_{eq}\ln s + P_{ext}V,
\end{aligned} \tag{3.34}$$

where was considered the relation $\pi_x = \partial\mathcal{L}/\partial\dot{x}$. Similar to the case of the extended Lagrangian, the above Hamiltonian describes a system of N real particles plus two virtual particles that control the pressure and temperature. The evolution equations using the Hamiltonian formulation are given by the following expresions:

$$\frac{\mathrm{d}}{\mathrm{dt}}q_i = \frac{\pi_i}{m_is^2V^{2/3}}; \qquad \frac{\mathrm{d}}{\mathrm{dt}}\pi_i = -V^{1/3}\frac{\partial U(\mathbf{r}_i)}{\partial r_i}; \qquad \frac{\mathrm{d}}{\mathrm{dt}}s = \frac{\pi_s}{M_s};$$

$$\frac{\mathrm{d}}{\mathrm{dt}}\pi_s = \frac{1}{s}\left[\sum_i \frac{\pi_i^2}{m_is^2V^{2/3}} - gk_BT_{eq}\right]; \quad \frac{\mathrm{d}}{\mathrm{dt}}V = \frac{\pi_V}{M_V}; \quad \frac{\mathrm{d}}{\mathrm{dt}}\pi_V = \frac{1}{3V}\sum_i\left[\frac{\pi_i^2}{m_is^2V^{2/3}} - r_i\frac{\partial U(\{\mathbf{r}_i\}}{\partial r_i}\right] - P_{ext}. \tag{3.35}$$

The variables (q_i, π_i) are not the positions and velocities in real space (r_i, p_i), since the variable s is intertwined with position and momentum. It is necessary to find a relationship between the real variables (r_i, p_i) and the set (q_i, π_i) in such a way that the equations of motion take on a Newtonian shape. For r_i, we have the following relationship:

$$r_i = q_iV^{1/D} \tag{3.36}$$

with D the dimensionality of the system, that typically is 3. The variable q_i takes values between 0 and 1, so r_i has a value between 0 and $V^{1/3}$.

The variable s is designated to rescale time through the following relationship:

$$dt = sdt'. \tag{3.37}$$

If we consider t' as the real time, we rewrite the equations in 3.35 with derivatives with respect to the time t', and after rearranging expressions, it is possible to demonstrate that the relationship between p_i and π_i is as follows:

$$p_i = \frac{\pi_i}{sV^{1/3}}. \tag{3.38}$$

The connection between r_i and p_i is obtained from $\mathrm{d}r_i/\mathrm{d}t' = \mathrm{d}(q_i V^{1/3})/\mathrm{d}t'$ and considering the expression $V^{1/3}\mathrm{d}q_i/\mathrm{d}t' = p_i/m_i$, as follows:

$$\frac{\mathrm{d}}{\mathrm{d}t'}\mathbf{r}_i = V^{1/3}\frac{\mathrm{d}\mathbf{q}_\mathrm{i}}{\mathrm{d}t'} + \mathbf{q}_i\frac{V^{1/3}}{3V}\frac{\mathrm{d}V}{\mathrm{d}t'} = \frac{\mathbf{p}_i}{m_i} + \mathbf{r}_i\frac{\mathrm{d}\varepsilon}{\mathrm{d}t'}. \tag{3.39}$$

Finally, the connection between $\mathbf{p}_i$ and the force $\mathbf{f}_i$ is given by:

$$\frac{\mathrm{d}\mathbf{p}_\mathrm{i}}{\mathrm{d}t'} = \mathbf{f}_i - \mathbf{p}_i\left(\frac{\pi_s}{M_s} + \frac{1}{3V}\frac{\mathrm{d}V}{\mathrm{d}t'}\right) \tag{3.40}$$

We can write the previous expression in a more familiar form by recognizing the coefficients of momentum as thermodynamic friction coefficients, ζ and ε, for the thermostat and barostat, respectively, as follows:

$$\frac{\mathrm{d}\mathbf{p}_\mathrm{i}}{\mathrm{d}t'} = \mathbf{f}_i - \mathbf{p}_i(\zeta + \dot{\varepsilon}); \qquad \zeta = \frac{\pi_s}{M_s}; \qquad \frac{\mathrm{d}\varepsilon}{\mathrm{d}t'} = \frac{1}{3V}\frac{\mathrm{d}V}{\mathrm{d}t'}, \tag{3.41}$$

where the evolution equation for ζ is given by:

$$M_s\frac{\mathrm{d}}{\mathrm{d}t'}\zeta = \sum_i \frac{\mathbf{p}_i^2}{m_i} - gk_BT_{eq} \tag{3.42}$$

By numerically solving these previous equations for a set of particles, we can simulate a system under isobaric-isothermal conditions with low computational cost.

3.2.3 Tuning the wettability

In order to study the effect of wetting on thermal transport at interfaces, we consider different wettability between the nanoparticle and the water molecules. For this purpose, we introduce a dimensionless parameter α that controls the intensity of the interaction between the nanoparticle atoms and water molecules. The parameter α is associated with the potential well value of the LJ potential, $\epsilon_{\mathrm{NpO}} = \alpha\epsilon_{\mathrm{AuO}}$.

We consider different values of α and characterize its effect on wetting by calculating the contact angle between a drop of water and a planar surface. The planar surface is made of the same atoms as the nanoparticle and has also an FCC crystalline structure. We consider three different values of α and obtain the following: i) strongly wetting nanoparticle with $\alpha = 1.0$, corresponding to a contact angle of 19^o, ii) intermediate wetting nanoparticle with $\alpha = 0.5$, corresponding to a contact angle of 39^o, and iii) weakly wetting nanoparticle with $\alpha = 0.3$, corresponding to a contact angle of 71^o.

We are interested in calculating an approximate value of the contact angle in order to characterize the type of wetting. The simulations to calculate the contact angles follow the next methodology. Initially, half of a sphere with 4384 water molecules and a radius of 40 Å is deposited on the planar surface. The system is then allowed to thermalize and relax for 1 ns using the Nose-Hoover barostat at 300 K and 1 atm. When the system is thermalized, the contact angle is calculated for each case. The pictures diplayed in Fig. 3.6 correspond to the final relaxed states of the droplets. While we are aware that this is not the best methodology to calculate contact angles, it allows us to characterize in a general way the differences between the different wettabilities we use.

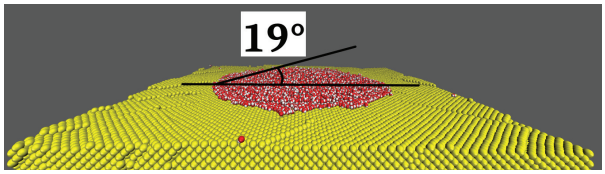

(a) Strong wetting, $\alpha = 1.0$

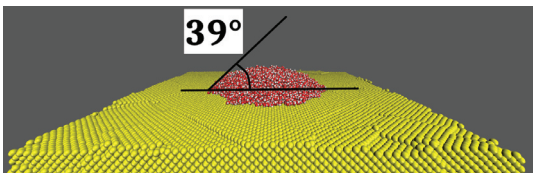

(b) Intermediate wetting, $\alpha = 0.5$

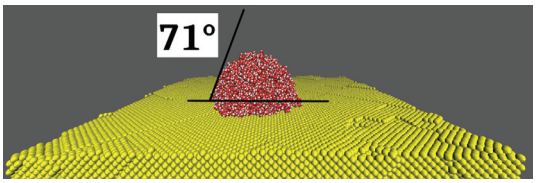

(c) Weak wetting, $\alpha = 0.3$

Figure 3.6: Contact angles measured for the different wetting interactions obtained by considering different values of α.

3.2.4 Methodology for the study of the size effects in thermal transport

In this case, we consider spherical nanoparticles of different diameters ranging from 1 to 8 nm occupying a volume fraction of $\sim 2\%$. With the purpose to prevent the displacement of the nanoparticle due to the Brownian motion, a spring potential with constant $k_s = 100.0$ Kcal/(mol Å^2) is applied to each atom of the nanoparticle. In a first stage, all the simulated systems are thermally equilibrated in the NPT ensemble, with $P = 1$ atm and $T = 300$ K. The Nose-Hoover barostat-thermostat approach is used. In the final stage of the thermalization, the same temperature is employed in the NVT ensemble using the Nose-Hoover thermostat approach. Once the thermal equilibrium is achieved, two types of simulations are unfolded considering constant volume. These simulations are: simulations with a steady heat flux and transient cooling simulations.

For the simulations with a steady heat flux, the nanoparticle is heated up to 500 K, nonetheless, the water molecules that are in a region far from the nanoparticle were maintained with the temperature 300 K. For both cases we use the Nose-Hoover thermostat. The function of the water in this region far from the nanoparticle is to dissipate the heat of the system (heat sink), simulating its dissipation in the surrounding medium, as seen in Fig. 3.7. For these cases, the heat sink is considered to have a spherical geometry and has radius according to the diameter of the nanoparticle. These radii ranges from 1.8 nm for a nanoparticle with a diameter of 1 nm to 10.4 nm for a nanoparticle with a diameter of 8 nm. The water molecules between the heat-sink region and the nanoparticle, which we call the water intermediate region, are simulated by considering an NVE ensemble.

Due to the existence of heat flux from the nanoparticle to the heat sink, the temperature of the water decreases radially. When the temperature at a fixed radial distance converges to a fixed value, a steady heat flux is considered to have been reached. The simulations are running long enough in the steady heat flux situation to obtain a significant amount of data for the quantities of interest. The total simulation times take from 0.7 up to 2 ns depending on the nanoparticle size.

In the transient cooling simulations, after the thermalization stage, the nanoparticle is heated up at 500 K for 20 ps using the Nose-Hoover thermostat. At the same time, the same thermostat is applied to the water molecules, but with a temperature of 300 K. After these 20 ps, the thermostat is removed from the nanoparticle and it is allowed to evolve in an NVE ensemble. In turn, the thermostat of the water at the intermediate region is removed, evolving its positions and velocities with the NVE ensemble. Finally, the water molecules in the region of the heat sink are left with the thermostat at a temperature of 300 K.

The dynamics are run such that the system reaches the equilibrium. The time to reach equilibrium

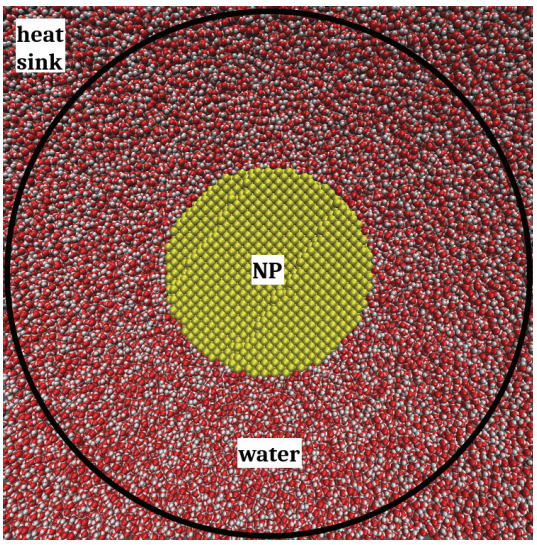

Figure 3.7: Illustration of a typical system: a gold-like nanoparticle surrounded by liquid water. The black circle delimits the location of the heat sink. This specific case corresponds to a nanoparticle of 8 nm of diameter.

depends on the size of the nanoparticle and on the wetting. The typical cooling times of the systems range from 30 ps to 100 ps. For transient cooling simulations, the statistics on the cooling kinetics was improved with 10 independent simulations for each nanoparticle and each wetting.

3.2.5 Methodology for the cavitation study

In this case we consider spherical, cubic (nanocube), and cylindrical (nanorod) nanoparticles. The diameters of the spherical nanoparticles range from 6 to 11 nm. The nanorod has a radius of 30 Å and a length of 95 Å, while the nanocube has sides of 64.5 Å. In order to compare properties between different geometries that occupy a similar volume, we build the nanocube, nanorod, and the nanosphere of 8 nm of diameter with a similar volume. In the case of the nanocube, nanorod, and spherical nanoparticles with a diameter between 6 to 9 nm, the volume fraction occupied by the nanoparticle initially is $\sim 2\%$. In the case of the nanoparticle with a diameter of 11 nm, the volume fraction that it initially occupies is $\sim 10\%$. The total number of atoms ranges from 5×10^5 to 9.9×10^5 atoms.

The systems are thermalized in the NPT ensemble using the Nose-Hoover thermostat-barostat for 300 ps, with a temperature of 300 K and a pressure of one atmosphere. After thermalization, isobaric dynamics are carried out in the NPH ensemble using the Nose-Hoover barostat. As previously explained, three wetting regimes are considered for the simulations: i) strong wetting, ii) intermediate wetting, and iii) weak wetting.

At each step, we translate the origin of the simulation box to the center of mass of the nanoparticle, taking this translation into account for all the atoms in the system. For cubic and cylindrical nanoparticles, we set their angular momentum equal to zero. This last operation is done so that the geometric regions defined to calculate the density and temperature profiles of the fluid are not affected by a possible rotation of the nanoparticles.

In this case, we do an in-silico simulation similar to the one carried out in a laboratory with ultra-short pulsed lasers. For this, we do the following. Every 40 ps the temperature of the nanoparticle is rescaled to temperatures in the range of 2000 K to 7000 K, depending on the case, through the rescaling of the velocities of its atoms. This temperature rescaling simulates laser pulsing, and the time interval between each rescaling (pulse) is fixed for all simulations. At the same time that we heat the nanoparticle (every 40 ps), we rescale the temperature of the water in the heat sink region at 300

K. This procedure is also done by rescaling the velocities of the atoms, and it helps to dissipate the excess of heat by simulating the medium in which it is dissipated. In the time interval between each heating of the nanoparticle, the system is allowed to relax in the NPH ensemble.

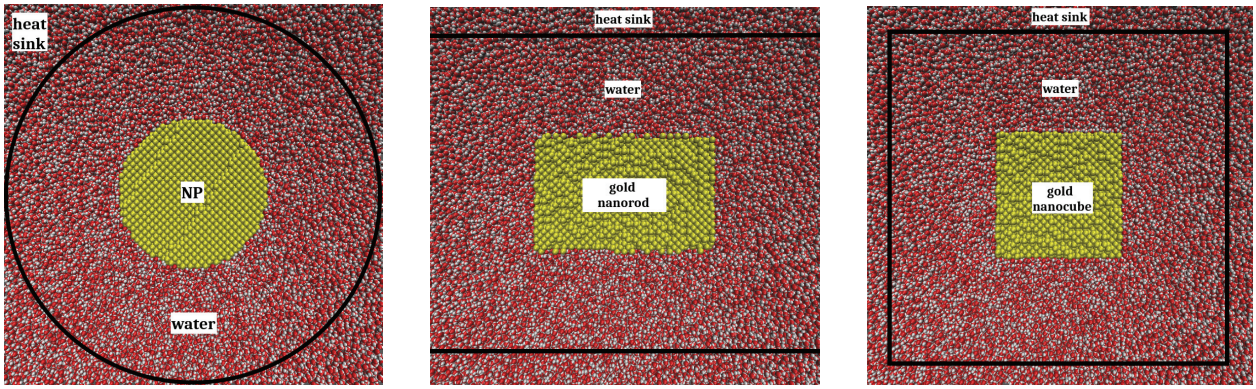

(a) Nanosphere (b) Nanorod (c) Nanocube

Figure 3.8: Cross-sections of the different systems considered. The black solid lines indicates the frontiers of the heat sink.

The specific region of the heat sink for each simulation depends on the geometry of the nanoparticle and are the following. For the spherical geometry, we consider the water at radial distances from the center of the nanoparticle that are larger than 10.5 nm for the nanoparticles of 6, 7, and 8 nm of diameter, 12.3 nm for the nanoparticle of 9 nm of diameter, and 9.5 nm for the nanoparticle of 11 nm of diameter. For the cubical geometry, we consider the water in the region outside the cube defined by the limits -10.4 nm to 10.4 nm for each spacial dimension. For the cylindrical region, we consider the water in the region outside a cylinder with 10.0 nm of radius, its axis is along the x direction with limits in -10.0 nm and 10.0 nm. This can be seen in Fig. 3.8.

3.2.6 Data collection and analysis

For the spherical nanoparticle, the data are collected from concentric spherical shells to evaluate the temperature and the density profiles. The region of interest goes from r_i to r_{hs}, with $r_i = R_{\mathrm{np}}/2$ and r_{hs} is the radius for the heat sink. This region is divided in shells like $[r_i, r_i + 2.0]$, $[r_i + 0.5, r_i + 2.5]$, $[r_i + 1.0, r_i + 3.0]$ Å, etc. For the cubical nanoparticle, the data is collected from concentric cubical geometry shells. The region of interest goes from $L_{x_i} = L_{\mathrm{cub}}/2$ to $L_{hs}/2$, with x_i representing each spatial dimension x, y or z, L_{cub} the cubic's length, and L_{hs} is the length of the cube that defines the heat sink region. For the cylindrical nanoparticle, the data is collected from concentrical cylindrical geometry shells. The region of interest goes from $r_i = R_{\mathrm{cyl}}/2$ to r_{hs}, with R_{cyl} the radius of the nanocylinder and r_{hs} the radius of the heat sink. For the cubic and cylindrical geometries, the shells are spaced just as for the spherical case, only respecting their specific geometry. The profiles are constructed by recording an instantaneous value of the temperature and the density every 50 fs for a time interval of 1 ps. At the end of the 1 ps time interval, the instantaneous values are averaged.

Chapter 4

Atomistic simulations in isothermal, isobaric, and isochoric conditions

In this Chapter, we will discuss the results concerning systems in thermodynamic equilibrium. In this case we seek to test the thermodynamic limit with respect to the smallest dimensions for which it is still valid. To this end, we use a system of 126 water molecules which interactions are simulated with DFT calculations. These water molecules are confined in a cylindrical volume that is built with exponential potentials and on top of it has a mobile cover. We propose a methodology to simulate dynamics under isobaric conditions by imposing the pressure across this mobile cover, in a way similar to a movable piston exerting a constant force on a confined fluid. We perform simulations under equilibrium conditions considering different temperatures between 300 and 360 K at one atmosphere, as well as constant volume simulations. With these simulations, we calculate the thermodynamic parameters of interest of the system, which are the heat capacities at constant volume C_V and pressure C_P, and the isothermal κ and isobaric α compressibility coefficients. We show that they are in good agreement with the experimental data, in addition we obtain the equation of state of the system.

We present the different ways to determine thermodynamic variables. In general, we make use of thermodynamic relationships to measure thermodynamic properties using data from Molecular Dynamics simulations. We consider temperatures in the range 300 - 360 K, pressure 1 atm, and also constant volume simulations.

4.1 Isobaric simulations

We impose a pressure of 1 atm through a constant force acting on the atoms in the cover. This force is of the gravitational type $F_i = m_i g$, where F_i is an external/artificial force exerted on the atoms of the cover and generates the pressure in water. In our case, the cover has a radius of 10.5 Å and 15361 atoms with a mass equal to the mass of gold. The gravity that generates a pressure of 1 atm is $g = 6.98528 \times 10^{-13}$ fs/Å^2. For more information, please check section 3.1.3.

4.1.1 Density of the systems

We let the system evolve until the cover stays in a position along the axis of the cylinder (z axis). When the height h of the cylinder is on average constant, the density of the water is also on average constant, since they are related by the formula $\rho = M_T/V = M_T/(\pi R_{\text{cyl}}^2 h)$ with M_T the total mass of the water molecules. In Fig. 4.1, we show graphs of the typical behavior of the density, temperature, and energy of water when it reaches a state of equilibrium. For the particular case shown there is an equilibrium temperature of 307.2 K, and for the other temperatures the behavior of the water density, temperature, and energy is found to be similar.

For the specific simulation of the data shown in Fig. 4.1, we impose a target temperature of 310 K for the Langevin atoms (see section 3.1.4). We get the water equilibration temperature at 307.2 K with

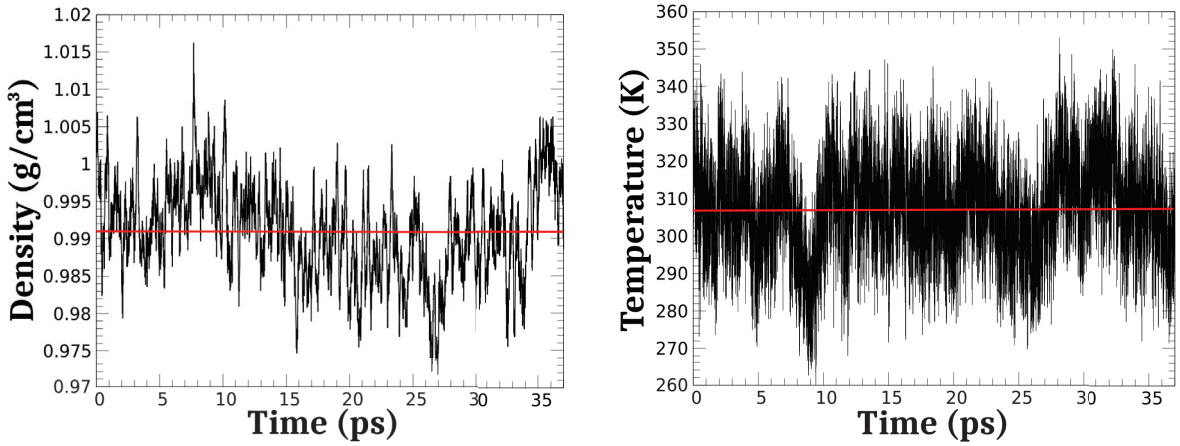

(a) Mass density

(b) Temperature

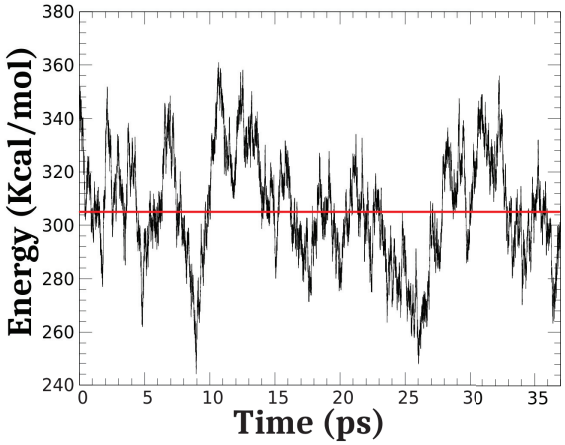

(c) Total energy

Figure 4.1: Typical behavior of the water density (Fig. 4.1a), temperature (Fig. 4.1b), and energy (Fig. 4.1c) when the system is equilibrated. This particular case corresponds to an equilibrating temperature of 307 K at a pressure of 1 atm.

an error bar of $\Delta T = \pm 12.4$ K. As seen in Fig. 4.1a, the density reaches an equilibrium value of 0.991 $\pm$ 0.006 g/cm^3 at a temperature of 307.2 $\pm$12.4 K. The experimentally measured density of water at 307 K is 0.994 g/cm^3 [87], so our calculation is very close to the experimental value. It is important to emphasize that we simply impose a constant force on the water molecules that, when divided by the area of action, gives a pressure of 1 atm. As seen in Fig. 3.1, the cover shows slight corrugations due to its atomistic-like structure. However, this corrugation can be neglected, and we can consider that the area of action of the cover on the water is the area of the confinement circle, πR_{cyl}^2. Up to a certain point, the cover is free to move to any point along z axis. Nevertheless, our methodology yields an equilibrium height of the cover that, in general, gives a water density close to the experimental value, as seen Fig. 4.2.

4.1.2 Isobaric response coefficients

Having reached thermodynamic equilibrium, we proceed to measure the thermal properties of interest. For these simulations under isobaric and isothermal conditions, we propose to calculate the heat capacity at constant pressure C_P, the coefficient of isobaric expansion α, and the coefficient of isothermal expansion κ.

To calculate the heat capacity C_P, we use two methodologies and compare their results. The first

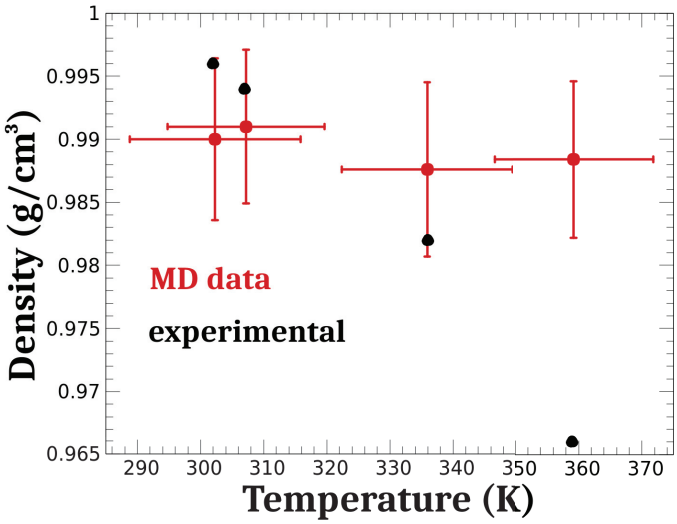

Figure 4.2: Density of water as a function of temperature. The red data are from MD simulations, and the black are the experimental data taken from Ref. [87].

methodology consists of using the definitions given by the thermodynamic. This definition is as follows:

$$C_P = \left(\frac{\partial H_{\mathrm{w}}}{\partial T}\right)_P = m_{\mathrm{w}} c_P, \tag{4.1}$$

where H_{w} is the water enthalpy calculated with Eq. 3.21, m_{w} the total mass of the water molecules, and c_P the specific heat capacity at constant pressure. Fig. 4.3 shows the enthalpy H_{w} as a function of the temperature for simulations under isobaric-isothermal conditions. The value of c_P obtained in our simulations is $c_P = 5.43 \pm 0.42$ J/(g K), while the experimental value is 4.18 J/(g K) [88]. These values are presented in Tab. 4.1. However, we must consider the limitations inherent to our system, in which our thermodynamic system consists of only 126 water molecules.

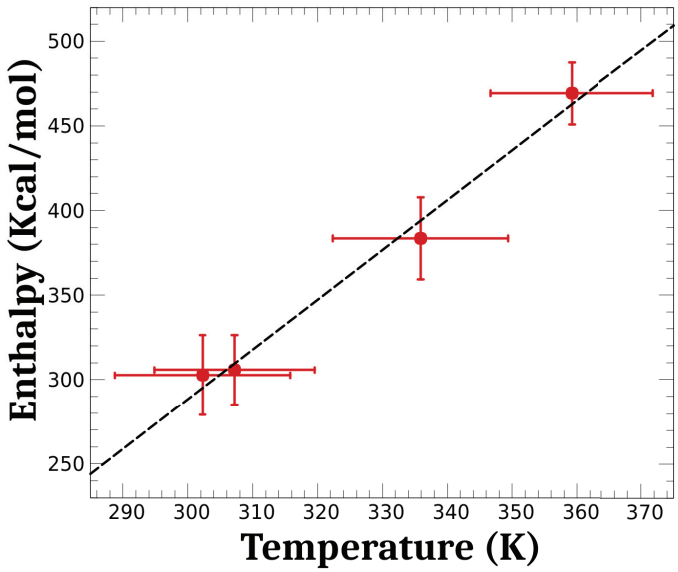

Figure 4.3: Enthalpy of water as a function of temperature.

The other methodology to calculate c_P is based on the concepts borrowed from statistical mechanics. As observed in Fig. 4.1, the data of the thermodynamic variables display fluctuations around their average values. We can construct an histogram of the enthalpy H values for each time and associate the

dispersion of the data with the heat capacity c_P. To this end, let us consider the following relationship:

$$\frac{\sigma_H^2}{\overline{H}} = \frac{\langle (H - \overline{H})^2 \rangle}{\overline{H}} = \frac{\langle H^2 \rangle - \overline{H}^2}{\overline{H}}. \tag{4.2}$$

We represent the average enthalpy of the system as $\overline{H} = \langle H \rangle$ and σ_H^2 the variance of H. We consider an isobaric-isothermal ensemble NPT with probability density of the states $\mathcal{P}$ which obeys a Maxwell distribution normalized by the partition function Z_{NPT}. This is $\mathcal{P} = \exp(-\beta H_i)/Z_{NPT}$, with $\beta = 1/(k_B T)$. To calculate $\sigma_H^2/\overline{H}$, we first calculate $\langle H^2 \rangle$ as follows.

$$\langle H^2 \rangle = \frac{1}{Z_{NPT}} \sum_i H_i^2 e^{-\beta H_i} = \frac{-1}{Z_{NPT}} \frac{\partial}{\partial \beta} \sum_i H_i e^{-\beta H_i}. \tag{4.3}$$

We note that $\sum_i H_i e^{-\beta H_i} = Z_{NPT} \overline{H}$, and then we have:

$$\langle H^2 \rangle = \frac{-1}{Z_{NPT}} \frac{\partial}{\partial \beta} \left(Z_{NPT} \overline{H} \right) = -\overline{H} \frac{\partial \ln Z_{NPT}}{\partial \beta} - \frac{\partial \overline{H}}{\partial \beta} \tag{4.4}$$

The first derivative on the right hand side is the average enthalpy $-\overline{H}$, and the second one can be related to the heat capacity at constant pressure C_P by its definition in the following way:

$$C_P = \frac{\partial \overline{H}}{\partial T} = \frac{\partial \beta}{\partial T} \frac{\partial \overline{H}}{\partial \beta} = -\frac{1}{k_B T^2} \frac{\partial \overline{H}}{\partial \beta}. \tag{4.5}$$

Now we can find the relation between the variance σ_H^2 and C_p by collecting each result:

$$\sigma_H^2 = k_B T^2 C_P \qquad \Longrightarrow \qquad C_P = \frac{\sigma_H^2}{k_B T^2}. \tag{4.6}$$

The previous equation allows us to connect data from the simulations with the concepts of statistical mechanics to calculate thermodynamic properties, in this case the values of C_P or c_P. However, this analysis is equally valid to calculate C_V or κ [89], as we will see later. It is worth mentioning that we can use the data from the MD simulations since we make the assumption that the ergodic hypothesis is valid, that is, time averages and ensemble average are equivalent.

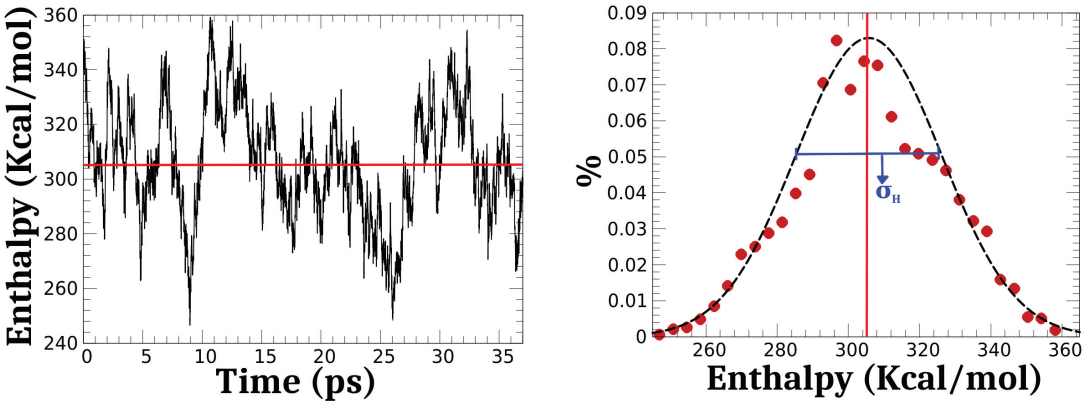

(a) (b)

Figure 4.4: Left: typical evolution of the enthalpy of the system as a function of time. Right: typical histogram built with the enthalpy values considering the data of Fig. 4.4a and the black dashed line is the Gaussian function associated. This specific case corresponds to the thermalized system at 307.2 K at 1 atm.

We consider different simulations under isobaric-isothermal conditions using different equilibrium temperatures. These simulations are the same with which the data shown in Fig. 4.3 is obtained.

The typical behavior of the enthalpy histogram is shown in Fig. 4.4. For each of these simulations, we calculate a value of c_P, and with these values we calculate an average value. The average value is $c_P = 4.29 \pm 1.21$ J/(g K). In this methodology, the value we obtain is closer to the experimental value, 4.18 J/(g K), as compared with the previous method that uses the thermodynamic relationship $C_P = (\partial H/\partial T)_P$ (see Tab. 4.1).

To calculate the isobaric expansion coefficient, we use its thermodynamic definition:

$$\alpha = \frac{1}{V}\left(\frac{\partial V}{\partial T}\right)_P. \tag{4.7}$$

To calculate α, we build a graph of the volume occupied by the water molecules as a function of their temperature, as shown in Fig. 4.5. We fit a curve to the data given by a second degree polynomial of the form $V(T) = A + BT + CT^2$. As is observed in Fig. 4.5, the volume as a function of temperature is shown to have a maximum at ~ 345 K. This behavior is also observed in Ref. [5].

Considering the simulation data when the system equilibrates at 307.2 K with a volume of 3.8038 nm^3, we obtain the value $\alpha = 0.1350 \times 10^{-3}$ K^{-1}. The experimental value of α is 0.2728×10^{-3} K^{-1} [5], so our result is in the expected order of magnitude but with a factor of 2 of difference with the value measured in the laboratory, as seen in Tab. 4.1.

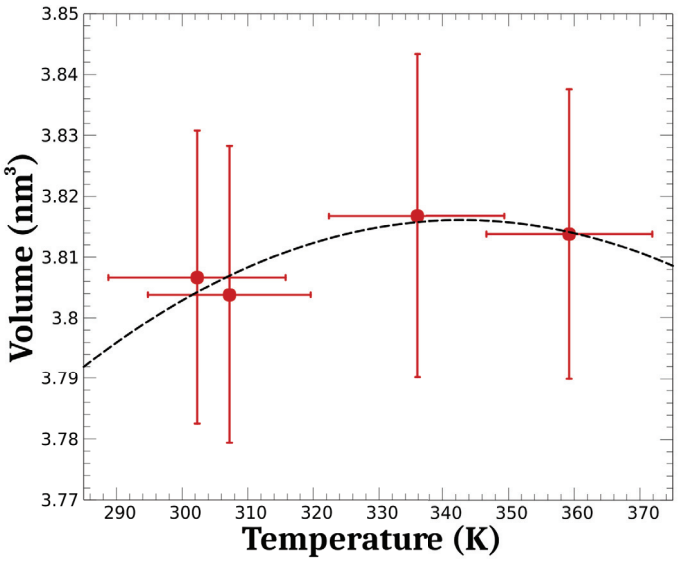

Figure 4.5: Volume occupied by the water molecules as a function of temperature. The black dashed lines correspond to the fitting with a second degree polynomial.

Finally, we calculate the coefficient of thermal compressibility κ using relations from statistical mechanics. We can follow a path similar to the one we took to obtain Eq. 4.6 and derive a relation for κ with the volume variance σ_V^2. The result is the following [89]:

$$\kappa = \frac{\sigma_V^2}{k_B T \overline{V}}. \tag{4.8}$$

We consider the isobaric - isothermal simulations and $\overline{V}$ is the average volume. Taking into account the data from the simulations in Fig. 4.3, we obtain the value of $\kappa = 0.0359 \pm 0.0037$ GPa^{-1}. The experimental value of κ is 0.4511 GPa^{-1} [5], so our result is one order of magnitude smaller than the laboratory value, as seen in Tab. 4.1. However, it should be noted that the units we work with are GPa^{-1}, that is, there is a factor of 10^9 Pa involved in the term. This large factor implies that small variations appear with considerable changes.

coefficient	formulas				experimental value
c_V [J/(g K)]	$\left(\frac{\partial U_{\mathrm{w}}}{\partial T}\right)_V$:	6.19 ± 0.35	$\frac{\sigma_U^2}{k_B T^2}$:	3.46 ± 0.89	4.13 [88]
c_P [J/(g K)]	$\left(\frac{\partial H_{\mathrm{w}}}{\partial T}\right)_P$:	5.43 ± 0.42	$\frac{\sigma_H^2}{k_B T^2}$:	4.29 ± 1.21	4.18 [88]
κ [GPa^{-1}]	$-\frac{1}{V}\left(\frac{\partial V}{\partial P}\right)_V$:	2.7916	$\frac{\sigma_V^2}{k_B \overline{V} T}$:	0.0359 ± 0.0037	0.4511 [5]
α [K^{-1}]	$\frac{1}{V}\left(\frac{\partial V}{\partial T}\right)_P$:	0.1350×10^{-3}	–	–	0.2728×10^{-3} [5]

Table 4.1: Values of the response coefficients calculated with different methodologies for the thermodynamic system of 126 water molecules compared with the corresponding experimental values.

4.2 Isochoric simulations

After reaching thermodynamic equilibrium under the isobaric - isothermal condition, we make the cover atoms static. The cover atoms can interact with the atoms of the water molecules, but they do not change their position during these simulations. In order to calculate thermodynamic properties of the system of 126 confined water molecules, we now proceed to calculate different quantities.

To calculate the specific heat at constant volume C_V we keep constant the volume of the system and vary its temperature. When the system is in equilibrium, we calculate the water total energy and plot it as a function of temperature. Fig. 4.6 shows water energy as a function of temperature from constant volume simulations.

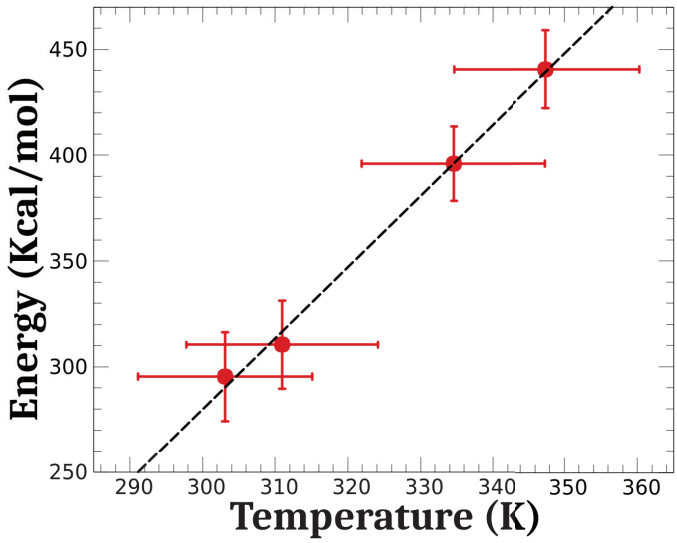

Figure 4.6: Total energy of the water molecules as a function of temperature.

We calculate the specific heat capacity c_V of the system using the following thermodynamic definition:

$$C_V = m_{\mathrm{w}} c_V = \left(\frac{\partial U_{\mathrm{w}}}{\partial T}\right)_V, \tag{4.9}$$

with U_{w} calculated using Eq. 3.20. The value we measure is $c_V = 6.19 \pm 0.35$ J/(g K), and the experimental value of c_V is 4.13 J/(g K). We conclude that our result is close to the experimental

value, as seen in Tab. 4.1.

As for the heat capacity at constant pressure, we can rely on statistical mechanics relations to calculate c_V and be able to compare with the previous results. Following a path similar to the one followed to obtain Eq. 4.6, only interchanging H_w to U_w, we obtain the following expression for C_V:

$$C_V = \frac{\sigma_U^2}{k_B T^2}. \tag{4.10}$$

We consider different constant volume simulations with different temperatures and calculate the variance of the water internal energy σ_U^2, thus obtaining several values for c_V. The average of these values and the standard deviation is $c_V = 3.46 \pm 0.89$ J/(g K). Again, this value is in the order of magnitude expected from experimental data as seen in Tab. 4.1. As in the case of c_P, the value measured with this method is closer to the experimental value than the one measured using thermodynamic relations.

4.3 Equation of state of the system

It is possible to find an equation of state for our system of confined water molecules using the Vinet equation [90]:

$$U_\mathrm{w} = E_k + E_p = \frac{N k_B T}{V} + a(T) + b(T) e^{\gamma(T) V^{1/3}} + c(T) V^{1/3} e^{\gamma(T) V^{1/3}}. \tag{4.11}$$

The first term corresponds to the kinetic energy of the system and the other terms to the potential energy of the system. The parameters $a(T)$, $b(T)$, $c(T)$, and $\gamma(T)$ depend on the temperature and can be obtained through a fitting to the data of potential energy as a function of volume considering all systems with the same temperature. Fig. 4.7 shows the potential energy of water as a function of volume considering a constant temperature of ~ 305 K. After obtaining the parameters, we can derive the equation of state using the thermodynamic relation $P = -\left(\partial U_\mathrm{w}/\partial V\right)_T$.

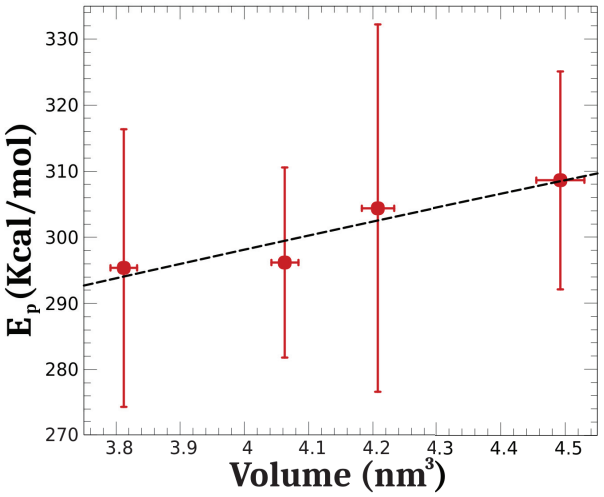

Figure 4.7: Potential energy of water molecules as a function of the total volume for a temperature of ~ 305 K. The black dashed lines correspond to the fit of the potential energy given by the Vinet equation, Eq. 4.11.

Using the equation of state 4.11 we can calculate the coefficient of isothermal expansion considering

the thermodynamic relations:

$$\kappa(V,T) = -\frac{1}{V}\left(\frac{\partial V}{\partial P}\right)_T = -\frac{1}{V\left(\frac{\partial P}{\partial V}\right)_T},$$
$$\kappa(V,T) = \left[\frac{Nk_BT}{V} + e^{\gamma V^{1/3}}\left(\frac{b\gamma^2}{9V^{1/3}} + \frac{c\gamma^2}{9} - \frac{2b\gamma}{9V^{2/3}} - \frac{2c}{9V^{2/3}}\right)\right]^{-1}. \tag{4.12}$$

Considering the fit to the data shown in Fig. 4.7, we obtain the following values of the parameters at $T \approx 305$ K: $a = 43.1421$ Kcal/mol, $b = 82.326$ Kcal/mol, $c = 36.6395$ Kcal/(mol nm), and $\gamma = 0.37553$ nm^{-1}. For a volume of 3.8119 nm^3 and temperature of 305 K, we obtain $\kappa = 2.7916$ GPa^{-1}. This value is one order of magnitude bigger than the experimental value, as seen in Tab. 4.1.

4.4 Time averages and ensemble averages

The ergodic hypothesis tells us that ensemble averages are equivalent to time averages. With this premise, we propose to calculate the total energy of the system and the square of the energy in order to compare temporal averages and ensemble averages. From Statistical Mechanics we know that for a system in the NVT ensemble whose distribution of states is given by a Maxwell distribution, its average energy is as follows:

$$\langle E\rangle = \frac{\sum_i E_i e^{-\beta E_i}}{\sum_i e^{-\beta E_i}} = \frac{\sum_i E_i e^{-\beta E_i}}{Z_{NVT}}. \tag{4.13}$$

where $Z_{NVT} = \sum_i e^{-\beta E_i}$ is the partition function, $\beta = 1/(k_BT)$, and E_i is an energy accessible by the system. If we replace E_i by E_i^2, we get $\langle E^2\rangle$. On the other hand, if we consider E_i as the energies of the system at each instant of time of our simulations, we can calculate $\langle E\rangle$ considering arithmetic averages, that is:

$$\langle E\rangle = \frac{1}{N_d}\sum_i^{N_d} E_i \tag{4.14}$$

with N_d the total number of data. Let's consider the case where the system is at constant volume and thermalizes at ~ 303.1 K. Table 4.2 shows the values of $\langle E\rangle$ and $\langle E^2\rangle$ when calculated considering Eqs. 4.13 and 4.14. For both cases, we consider for E_i the data that come from the simulation. As can be seen, the values of $\langle E\rangle$ and $\langle E^2\rangle$ that are predicted by Eqs. 4.13 and 4.14 are different, and when we inspect graphically Fig. 4.8 we see that the value derived from the ensemble average the ensemble is wrong.

	eq. for average	
	$\langle A\rangle = \sum_i A_i e^{-\beta A_i}/\sum_i e^{-\beta A_i}$	$\langle A\rangle = \sum_i A_i/N_d$
$\langle E\rangle$ [a.u.]	0.38465	0.47178
$\langle E^2\rangle$ [(a.u.)^2]	0.14795	0.22372
c_V [J/(g K)]	0.008	4.56

Table 4.2: Values of $\langle E\rangle$, $\langle E^2\rangle$, and c_V obtained by different routes.

When we proceed to calculate c_V considering a relation similar to Eq. 4.2, we obtain the value of 0.008 J/(g K) considering Eq. 4.13 and 4.56 J/(g K) with Eq. 4.14. The value calculated considering an average over time is in the order of the expected value. Nevertheless, the value considering an ensemble average is three orders of magnitude less than the experimental value.

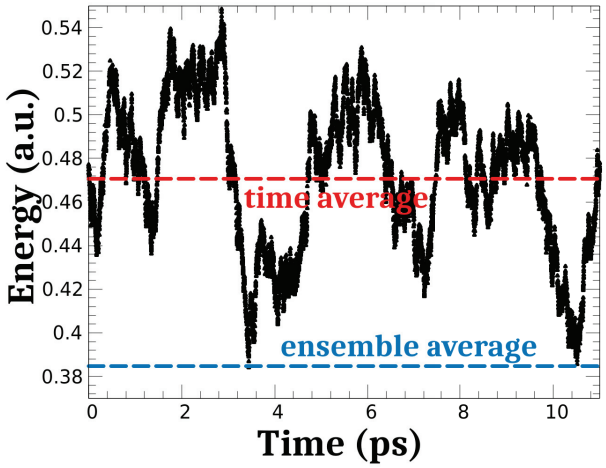

Figure 4.8: Water total energy as a function of time in the NVT ensemble. The blue dashed line is the average calculated with Eq. 4.13 and the red one is calculated using Eq. 4.14.

4.5 Discussion and summary

The objective of this section has been twofold: first, to asses the validity of the thermodynamic for systems of a few molecules and to test a methodology to impose the pressure in MD simulations. As shown in Fig. 4.2, the equilibrium density of the system of 126 water molecules confined with a pressure of 1 atm is very close to the experimental value. Except for the data calculated at the equilibrium temperature of ~ 358 K, the experimental value of the density falls within the error bar of the simulation data. It is worth mentioning that the error bar for the density is not greater than 0.7% of the mean value, so that even for the data that is outside the error bar, its value is still close enough, above 2.3% of the experimental value.

Except for the isothermal expansion compressibility κ, the thermodynamic response coefficients of the system are in the expected order of magnitude and close to the experimental values. The thermodynamic definition of κ involves second derivatives of the energy of the system in the denominator, that is:

$$\kappa = -\frac{1}{V}\left(\frac{\partial V}{\partial P}\right)_T = \frac{1}{V}\frac{1}{-\left(\frac{\partial P}{\partial V}\right)_T} = \frac{1}{V}\frac{1}{\left(\frac{\partial^2 U}{\partial V^2}\right)_T}. \tag{4.15}$$

The second derivatives are very sensitive to small variations, and if we take into account the fact that they are in the denominator, it is to be expected that the quantities associated with them are at least as sensitive to small changes. This could explain why for κ we calculate values having a difference of two orders of magnitude if we use the method of variances or the thermodynamic relationship.

Of the two methodologies to calculate c_V and c_P, it is found that the relation that uses the variances yields values closest to the experimental value. Furthermore, the results from this relation satisfy the thermodynamic condition $c_P > c_V$. When calculating c_V and c_P by considering thermodynamic relations, we obtain a value having the expected order of magnitude and close to the experimental value, but in this case $c_V > c_P$ which is not in accordance with thermodynamics. However, we must take into account the limitations inherent to our system. The uncertainty of the energy as a function of the number of particles is $\sigma_U/\overline{U} \propto N^{-1/2}$. As we see in Tab. 4.1, the uncertainties of c_V and c_P cause their values to fall within the error values. Therefore, it is expected that by increasing the number of atoms to reduce the variance, the discrepancies will be corrected.

Despite the discrepancies already mentioned, all the parameters we calculate are in general in agreement with experimental data, taking into account the small number of molecules that make up our system confined in a volume of a few nm^3. This leads us to think that thermodynamics is still valid even for a

system of a few tens of molecules occupying a nanoscale volume. The values of the parameters that we calculate can be improved if we increase the number of independent simulations in order to obtain a greater sampling of the system. However, a limitation is the computation time since here we consider the intra- and inter-molecular interactions of the water molecule using DFT. This limitation can be overcome with the rapid growth in computing efficiency, for example with the continuous optimization of GPUs. We could even limit ourselves to the case of using classical models for intra- and inter-molecular interactions, and thereby greatly speed up the computation time. However, the idea is to guide the technique in simulations of phenomena that from an analytical point of view are difficult to treat, for example mixtures in which there may be creation/formation of chemical bonds.

The philosophy behind the method that we use and propose is to perform simulations of physical phenomena without the need to use, as much as possible, complex concepts, such as a partition function for example, or methodologies to impose isobaric conditions that do not have a similarity with the physical reality. For example, if we add molecules different than water to our systems, we will obtain a system that is a mixture. We would have direct access to the thermal properties of the system, since we know all the necessary information in full-atomistic detail. We could even increase the system pressure and/or temperature in order to induce chemical reactions in the system considering isobaric or isochoric conditions. Furthermore, it is worth remembering that Molecular Dynamics is equally valid for systems out of equilibrium as in equilibrium, so the proposed methodology inherits this feature.

For example, to study a mixture using Statistical Mechanics, we would have to know its partition function. The less homogeneous the thermodynamic system to be studied, the more complex its partition function becomes to calculate. If, in addition to considering that we have a thermodynamic system that is a mixture, we consider that there is a chemical reaction with bond formation/breakage, the calculation of the partition function becomes a titanic task. And let's not even talk about systems out of equilibrium, which can be studied, to a certain extent, if and only if the perturbation that brings them out of equilibrium is small. In fact, for very few systems analytical solutions to the partition function are known and most of these systems are idealizations far from a real system.

Another point to be taken into account is that, just as the thermodynamic limit for macroscopic systems is well-defined, Statistical Mechanics requires $N \to \infty$ and $V \to \infty$ be satisfied. However, there is no defined lower limit that tells us to what extent the theory of Statistical Mechanics is valid. For thermodynamics, we have shown that its validity continues to hold for systems of a few tens of molecules. But in section 4.4, we show that an ensemble average and a time average of the energies of one of our systems do not lead to the same result. Even the discrepancy becomes so large that when calculating c_V we have orders of magnitude of difference between the temporal average and the ensemble average. This leads us to think that ensemble averages are more sensitive to the total number of particles that make up the system, and require a sufficiently large number of particles to become valid.

The Molecular Dynamics technique lends itself to avoid these difficulties. We can calculate the thermodynamic properties of the system for any type of mixture with a few tens of molecules. Furthermore, we can study out-of-equilibrium phenomena regardless of whether the perturbation that brings the system out of equilibrium is large or small. It is in this sense that it becomes necessary to propose methodologies for MD in which physical systems are simulated more in line with physical reality. The methodology that we propose to simulate isobaric conditions is in line with introductory thermodynamics courses when studying a fluid confined by a piston. We avoid, to a certain extent, the need to use fictitious particles that control the pressure of the system and its consequences of working with Lagrangians with a poor physical interpretation. The methodology shows that the thermodynamic properties of the system in which it is applied are in general in agreement with experimental data.

Nevertheless, some elements of the approach need to be improved. One of them is the type of interaction between the cover atom and the fluid molecule. In this case, we use an interaction through

an exponential potential, Eq. 3.6, that due to its nature decays quickly, which forces us to use a very dense cover in order to prevent fluid molecules from escaping due to porosity. To work with a very dense cover can be computationally expensive if we take into account that the cover is atomistic. Care needs to be taken how to choose this type of interaction since a van der Waals interaction induces layering of the fluid close to the cover, as shown in Fig. 3.4. If we consider nanoscale systems, this fluid layer with a different structure from the bulk can induce changes in its physical properties. Although this structure induced by the cover atoms when considering a van der Waals type interaction is more realistic, the idea of the proposed methodology goes in the direction of being able to calculate properties of the system when it has characteristics similar to those of the bulk. This is why it is necessary to devise an interaction cover atom - fluid molecule that disturbs the structure of the fluid to be studied as little as possible. However, if the interest turns to studying the changes in the thermal properties of the fluid due to the fluid structuring order by the van der Waals type interaction, the proposed method to simulate isobaric conditions is equally applicable.

Chapter 5

Heat transfer across gold nanoparticles in water: size effects and anharmonic effects

We have already presented the results and discussion concerning systems in thermal equilibrium, and we now turn our attention to studying systems out of thermal equilibrium. In this Chapter and the next, we present and discuss the results concerning non-equilibrium systems. More specifically, we focus on understanding heat transport between metallic nanoparticles having different wettability that are heated, and transfer heat to their aqueous environment.

First, we analyze the effects of size on metal nanoparticle-water interfacial thermal transport. The results show that for not very large nanoparticle heating, the interfacial heat transport is enhanced by reducing the nanoparticle size. In order to understand this effect, we analyze different physical quantities such as the interfacial potential energy, which shows that the smaller the nanoparticle is its interfacial atoms have stronger bonds with fluid molecules. We perform a spectral analysis and show that low frequency vibration modes are the dominant ones in the heat transport at the nanoparticle-water interface. Reducing the size of the nanoparticle exacerbates the vibrational modes at low frequencies, helping to explain the enhancement of interfacial heat transport by reducing nanoparticle dimensions. In turn, based on the spectral analysis, we show that the anharmonic contribution to heat transport is larger for weak wetting interactions. These results and others, as well as their discussion, are presented in the following sections.

5.1 Size effects

This section presents the results concerning the effect of size on the nanoparticle-fluid interfacial heat transport. In addition to the results, we present different interpretations in order to answer why by decreasing the size of the nanoparticle interfacial heat transport is more efficient.

5.1.1 Acoustic model for the size-dependent conductance

In order to predict size effect of the interfacial conductance, we will derive an analytical relation for the interfacial thermal conductance G_{K} defined in Eq. 1.4. The purpose of this section is to present a simple analytical model to predict the size-dependent thermal conductance at the interface of the nanoparticle and water. To this end, we employ a recent generalized acoustic mismatch model designed to tackle heat transport at the solid-liquid interface [91].

The thermal conductance is given by:

$$G_{\mathrm{K}} = \sum_{p} \int_{0}^{\omega_{\max}} k_B g_p(\omega) v_p(\omega) \tau_p(\omega) d\omega \tag{5.1}$$

p is an index denoting the transverse and longitudinal polarization, $\omega_{\max}$ is the maximal frequency of the vibrational spectrum of the nanoparticle, $g_p(\omega)$ is the nanoparticle vibrational density of states,

$v_p(\omega)$ the corresponding group velocity, and $\tau_p(\omega)$ is the phonon transmission function. It is convenient to adopt an acoustic model of τ_p given in [91, 92], which approximately explains the heat transfer at the interface of two media:

$$\tau_p(\omega) = \frac{Z_{\mathrm{np}}(\omega) Z_{\mathrm{wat}}(\omega)}{(Z_{\mathrm{np}}(\omega) + Z_{\mathrm{wat}}(\omega))^2 + \frac{\omega^2}{K^2(R_{\mathrm{np}})}(Z_{\mathrm{np}}(\omega) Z_{\mathrm{wat}}(\omega))^2} \tag{5.2}$$

$Z_{\mathrm{np}}(\omega) = \rho_{\mathrm{np}} v_{\mathrm{np}}$ and $Z_{\mathrm{wat}}(\omega) \rho_{\mathrm{wat}} v_{\mathrm{wat}}$ are the acoustic impedance of the nanoparticle and water, respectively (we omitted the polarization index for simplicity). ρ_i and v_i are the density and the sound velocity of the medium i.

We assume a harmonic interaction between the nanoparticle atoms and the water atoms with a spring stiffness given by $K(R_{\mathrm{np}})$ [91, 92]. The spring stiffness may be written as the product of the interface potential curvature $\frac{d^2V}{dr^2}$ and the number of gold-water contacts per surface unit, $\sigma(R_{\mathrm{np}})$. To estimate how this latter quantity depends on the nanoparticle radius R_{np}, we adopt a simple model proposed by Jimenez et al. [93]. Let us consider a water molecule interacting with the gold nanoparticle as represented in Fig. 5.1.

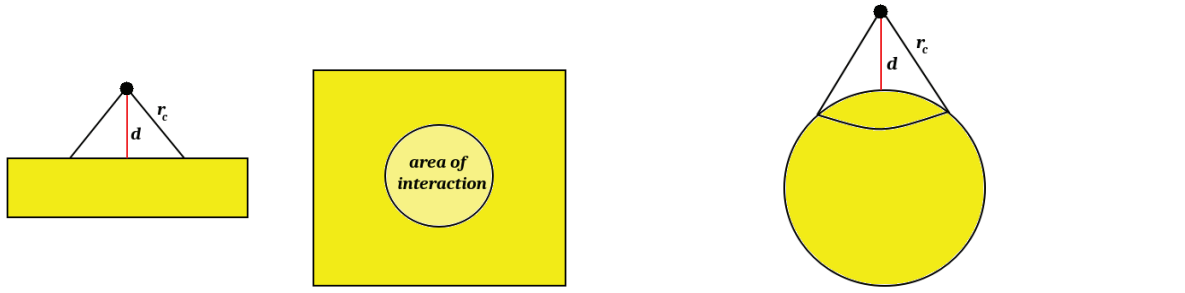

Figure 5.1: Illustration of the curvature dependent area of interaction at the water-gold interface. Left: planar interface. Right: curved interface. These illustrations are inspired by [93].

We assume a simple model where a water molecule interacts with a gold atom if their distance δ is smaller than the cut-off radius r_c. Below the cut-off the interaction is supposed to be constant, independent on the distance δ. We now give the expression of the area of interaction $s_{\mathrm{R_{np}}}(\delta)$, defined as the area of gold atoms interacting with a water molecule at a distance δ from the interface. First, for a planar interface, it can be proven that:

$$s_{R_{\mathrm{np}} \to \infty}(\delta) = \pi(r_c^2 - \delta^2) \tag{5.3}$$

For a curved interface, the area of interaction is increased with respect to the planar case:

$$s_{R_{\mathrm{np}}}(\delta) = \pi \frac{(r_c^2 - \delta^2)}{(1 + \delta / R_{\mathrm{np}})} \tag{5.4}$$

From these two equations, we conclude that the surface density of gold-water contacts $\sigma(R_{\mathrm{np}})$ may be written as:

$$\sigma(R_{\mathrm{np}}) = 1 / s_{R_{\mathrm{np}}}(\delta) = \sigma(\mathrm{R_{np}} \to \infty)\,(1 + \delta / \mathrm{R_{np}}) \tag{5.5}$$

$\sigma(R_{\mathrm{np}} \to \infty) = 1/(\pi(r_c^2 - \delta^2))$ is the surface density corresponding to a flat interface, and we denoted with δ the average interaction distance between a gold atom and a water molecule. From such considerations, we deduce that $K_{R_{\mathrm{np}}}$ may be expressed as:

$$K(R_{\mathrm{np}}) = K(\mathrm{R_{np}} \to \infty)\,(1 + \delta / R_{\mathrm{np}}) \tag{5.6}$$

with obvious notations.

In the limit where the binding stiffness is weak, one has the approximation:

$$(Z_{\rm np}(\omega)+Z_{\rm wat}(\omega))^2+\frac{\omega^2}{K^2(R)}(Z_{\rm np}(\omega)Z_{\rm wat}(\omega))^2\simeq\frac{\omega^2}{K^2(R_{\rm np})}(Z_{\rm np}(\omega)Z_{\rm wat}(\omega))^2$$

$$\tau_p(\omega)\simeq K^2(R_{\rm np})/\omega^2\propto(1/\omega^2)(1+\delta/R_{\rm np})^2 \tag{5.7}$$

After taking these considerations in Eq. 5.1, the resulting interfacial thermal conductance is:

$$G_{\rm K}(R_{\rm np})\simeq G_{\rm K}(\infty)\left(1+\frac{\delta}{R_{\rm np}}\right)^2 \tag{5.8}$$

$G_{\rm K}(\infty)$ is the conductance of the corresponding flat interface. We thus predict a quadratic dependence of the conductance. Alternatively, we will compare the MD simulation data to the empirical relation proposed in [36]:

$$G_{\rm K}(R_{np})=G_{\rm K}(\infty)\left(1+\frac{\delta}{R_{np}}\right) \tag{5.9}$$

5.1.2 Calculation of interfacial thermal conductance $G_{\rm K}$ from MD

In order to determine the interfacial thermal conductance using MD, we consider transient simulations. The nanoparticle is first heated up to 500 K for 40 ps. Later, it is allowed to cool down as previously described in Sec. 3.2.4, and we register the nanoparticle temperature every 25 ps. At the same time, the water in the heat sink region is fixed at 300 K using the Nose-Hoover thermostat. The nanoparticle temperature, $T_{\rm np}$, in the cooling process as determined from the MD simulations is employed to determine the interfacial thermal conductance, $G_{\rm K}$, from the Eq. below:

$$C_p\frac{dT_{\rm np}(t)}{dt}=-A_{\rm np}G_{\rm K}\left(T_{\rm np}(t)-T_s\right), \tag{5.10}$$

C_p is the nanoparticle heat capacity, $A_{np}=4\pi R_{\rm np}^2$ the area of the nanoparticle, and T_s the water reservoir temperature. The general solution of Eq. 5.10 gives the nanoparticle temperature with time, $T_{np}(t)=C_1e^{-C_2t}+C_3$. The coefficients C_1, C_2, and C_3 are fitted from the MD simulation data. Thereby, we calculate $G_{\rm K}$ from $C_2=A_{np}G_{\rm K}/C_p$, which is obtained by substituting $T_{np}(t)$ in Eq. 5.10.

5.1.3 Size-dependent conductance

Thermal conductance from MD simulations

The conductance of gold nanoparticles as a function of their radius for the three wetting regimes - strongly wetting, intermediate, and weakly wetting- is illustrated in Fig. 5.2a. For all the types of nanoparticles, the conductance increases when the nanoparticle size decreases. Fig. 5.2a shows that both functional forms, the quadratic function of the acoustic model, Eq. (5.8), and the empirical formula proposed in [36], Eq. (5.9), provide a good description of the size effects of the nanoparticle-water interfacial thermal conductance. The values of the parameters $G_K(\infty)$ and δ are given in Tab. 5.1. The value of the infinite radius thermal conductance, $G_K(\infty)$, ranges from 49 MW/(K $\cdot$ m^2) for weakly wetting interfaces to 143 MW/(K $\cdot$ m^2) for strongly wetting interfaces.

The normalized interfacial thermal conductance of gold nanoparticles as a function of their radius for the three wetting regimes is illustrated in Fig. 5.2b. The normalized interfacial thermal conductance corresponds to the conductance divided by the maximal value, $\tilde{G}_{\rm K}=G_{\rm K}(R_{np},\theta)/G_{\rm K}^{(\max)}(\theta)$ with θ the contact angle in each case. The data of Tascini et al. [36] concerning the size-dependent conductance of gold nanoparticles in a Lennard-Jones fluid, and the data of Ong et al. [38] corresponding to an array crystal, are also included. Fig. 5.2b confirms that the quadratic expression, Eq. 5.8, of the acoustic model gives a good description of the data of Tascini et al. and Ong et al. The empirical linear model

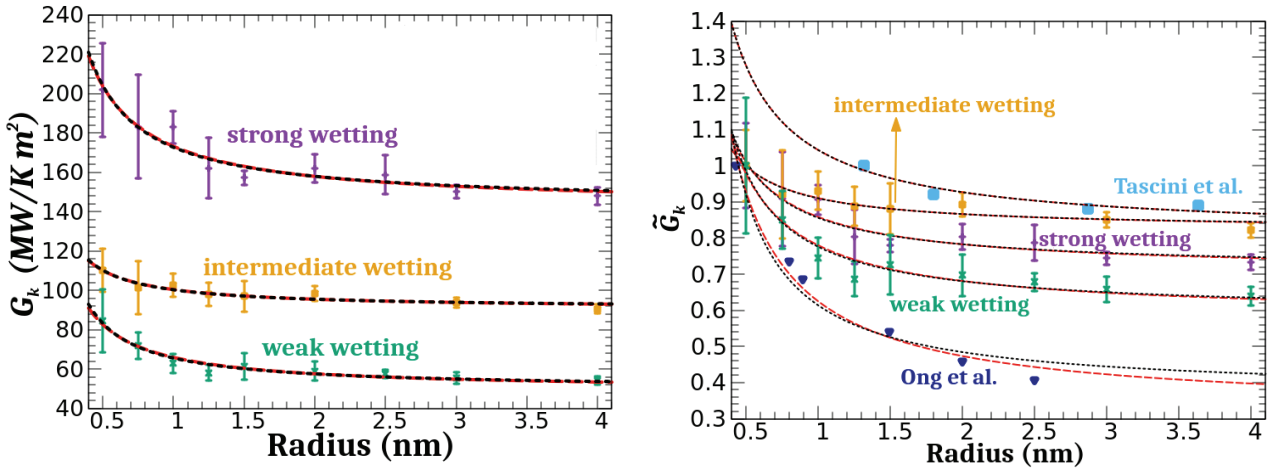

Figure 5.2: a) Gold-water thermal interface conductance, G_k, as a function of the gold nanoparticle radius for the different wettings. The values of the length δ and the conductance $G_K(\infty)$ are given in Tab. 5.1. b) Normalized interfacial conductance in terms of the nanoparticle radius. The MD data of Ong et al. [38] (dark blue symbols) and Tascini et al. [36] (light blue symbols with $F = 1$) are also included. Our MD data, and those of Ong, and Tascini are compared with Eqs. 5.8 and 5.9 (red dashed lines and black dashed lines, respectively).

fitting	$G_{\mathrm{K}}(\infty)$ (MW/K m^2)	δ (nm)
strongly wetting		
linear	142.583 ± 3.238	0.21 ± 0.03
quadratic	143.788 ± 3.102	0.10 ± 0.01
intermediate wetting		
linear	90.533 ± 1.342	0.11 ± 0.02
quadratic	90.755 ± 1.307	0.05 ± 0.01
weakly wetting		
linear	49.177 ± 1.433	0.34 ± 0.04
quadratic	49.948 ± 1.190	0.15 ± 0.01

Table 5.1: Parameters of the quadratic (Eq. 5.8) and linear (Eq. 5.9) models.

also provides a good description of such data, as already noticed in [36,38].

Two observations regarding the value of the length δ are important to remark. Firstly, the value of δ is approximately of the same order of magnitude as that of the water-molecule radius, which is consistent with the fact that the size effects of the thermal conductance are noticeable for small nanoparticles ($R_{\mathrm{np}} < 2$ nm). Secondly, for all the wetting regimes investigated in this work, we find $\delta > 0$, indicating that the thermal conductance increases when the nanoparticle size decreases. This result is consistent with the study of Tascini et al. [36] and Ong et al. [38], but is different from the work of Neidhart et al. [35], who reported the opposite behavior $\delta < 0$, i.e the thermal conductance decreases for small nanoparticles.

5.1.4 Relation thermal conductance-fluid density

It is generally argued that the thermal interface conductance G_{K} is strongly correlated with the density of the fluid at the interface [94,95]. For a graphene-water system, this relation is described by $G_{\mathrm{K}}(\rho_p) = (\rho_p + B)/A$, where ρ_p is the first peak of the fluid density profile, and A and B are two constants which depend of the system type. We should mention, however, that the correspondence

between the interface conductance and the fluid density is not universal, and may even break down as discussed in [95–97].

To discuss the relevance of the relation between the interfacial thermal conductance G_{K} and the fluid density ρ_p, we have analyzed the behavior of G_{K} as a function of ρ_p. Fig. 5.3a shows the first peak of the water density in terms of the nanoparticle radius under a steady heat flow situation. It is observed that for small nanoparticles, the amplitude of the first peak increases. The size dependence of the density of the water layer surrounding the nanoparticle is well described with the functional form $\rho_p(R_{np}) = A\exp(-BR_{np}) + C$. This form describes an exponential decay of the fluid density with the radius of the nanoparticle, leading to $\rho(R_{np}) = C$ when $R_{np} \to \infty$. This result is qualitatively different from a similar study [98], where the density of the nanolayer for spherical Ag nanoparticles increases as the radius of the nanoparticle increases, reaching a fixed value in the flat-interface limit. The authors of [98] propose a relation between the density of the nanolayer and the diameter of the nanoparticle taking the form $\rho(D_{np})_p = a\exp(-b/D_{np}^c)$ where a, b and c are constants. In our gold-water system, the exponent of D_{np} is $c = -1$ and we have an independent constant associated with the density of the nanolayer of the corresponding flat surface.

We discuss the relation between G_{K} and ρ_p. Figs. 5.3b and 5.3c exhibit the interfacial thermal conductance as a function of the water nanolayer density ρ_p. Our results show that, for a fixed nanoparticle radius R_{np}, the evolution of G_{K} with the contact angle (or wetting) is well described by $G_{\mathrm{K}}(\rho_p) = (\rho_p + B)/A$. Such a relation changes to $G_k(\rho_p) = (\rho_p + B')/A'$ ($A \neq A'$ and $B \neq B'$) when the contact angle is fixed, and the diameter changes. Therefore, we conclude that the relation between the interfacial conductance and the first peak density is not universal, and depends on both the nanoparticle curvature and its wetting properties.

5.1.5 Interpretation

In order to interpret the size effects of the thermal conductance as represented in Fig. 5.2, we analyze the different physical quantities that control interfacial heat transport between the nanoparticle and water.

Interfacial potential energy

First, let us consider the potential energy characterizing the gold-water interface. Heat is transferred between these two media through the interaction between the atoms of the nanoparticle and the atoms of the fluid. Fig. 5.4a shows the potential energy per atom of the nanoparticle due to the interaction with water as a function of the nanoparticle radius. There is a shell around each gold atom with radius 11 Å and all the water molecules inside this radius are considered in the calculation of the potential energy. The total potential energy calculated in this way is divided by the total number of the gold atoms that interact with water. From Fig. 5.4a it is observed that the potential energy is lower for small nanoparticles. In addition, at a fixed value of R_{np}, the interfacial potential energy is lower for strongly wetting nanoparticles. This result is consistent with the fact that strongly wetting nanoparticles should be characterized by a high work of adhesion, as compared to weakly wetting nanoparticles. Finally, the size dependence of the potential energy is more pronounced for strongly wetting nanoparticles. The more negative potential energy observed for small nanoparticles indicates a stronger bonding of the gold-water interface, which should lead to increased thermal conductance.

The average number of neighbor oxygens, obtained after dividing the total number of gold atoms that interact with water, is shown in Fig. 5.4b. We observe that the number of neighbors increases for small nanoparticles. Due to these increased interactions, the potential energy becomes more negative, partially explaining the behavior outlined in Fig. 5.4a. After observing Figs. 5.4a and 5.4b, we conclude that there is a correlation between the interfacial potential energy and the number of oxygen neighbors.

Another important observation concerns the relation between the interfacial conductance and the

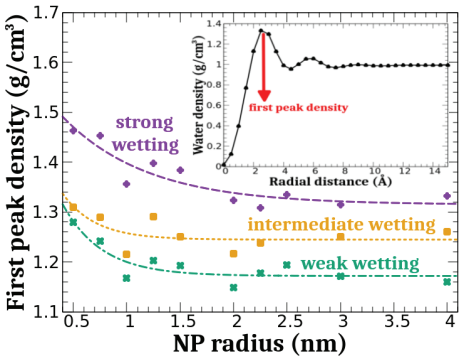

(a)

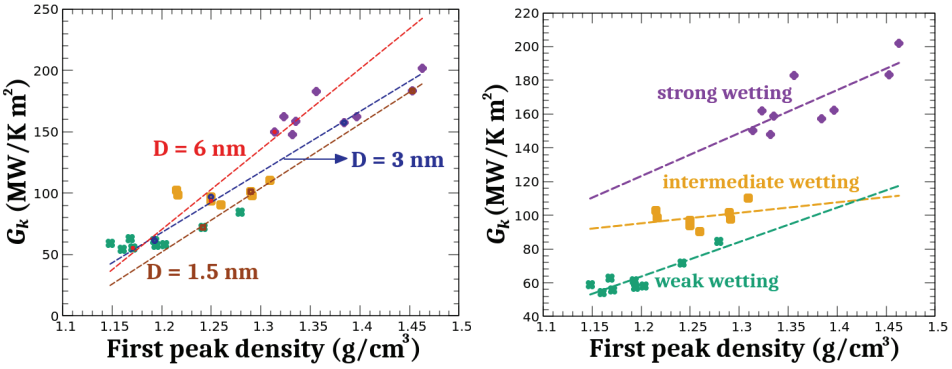

(b) (c)

Figure 5.3: Fig. 5.3a shows the water-solvation first peak as a function of the nanoparticle radius. A typical water density profile around the nanoparticle is shown in the inset. Figs. 5.3b and 5.3c show the interfacial thermal conductance as a function of the first density peak for several nanoparticle diameters and for a fixed wetting, respectively. The data are shown for all the nanoparticles sizes in each wetting regime. The function $G_k(\rho_p) = (\rho_p + B)/A$ is also represented in both figures. This function describes the simulation data for the three different wetting regimes and for nanoparticles having diameters $D_{\rm np} = 6, 3$ and 1.5 nm.

coordination number of the interfacial atoms. The smaller the nanoparticle, the higher the coordination number due to the increased curvature. Indeed, this behavior is also explained by a recent work where is studied $G_{\rm K}$ and the density depletion length [99]. In our case, we observe in Fig. 5.4c that the thermal conductance increases when the coordination number increases. This conclusion is compatible with the results of Jiang et al. [100], in spite of the fact that they consider different nanoparticle shapes without changing the nanoparticle size, and a monoatomic Lennard-Jones fluid. The correlation between the interface conductance and the coordination number seems to have general character regardless of the fluid molecular structure, at least for relatively simple molecular fluids.

Density of states

Up to now, we have analyzed the enhancement of the thermal conductance of strongly curved nanoparticles in terms of the potential energy and interface bonding. Interfacial heat transfer depends also on the vibrational density of states (DoS) of the two media. In the following, we examine the DoS of the gold nanoparticle $P_{np}(\omega)$ and of the oxygen atoms of the fluid $P_O(\omega)$.

We compute the DoS from the velocity autocorrelation function, $f_{\rm vac}$, by:

$$\widehat{f}_{\rm vac}(\omega) = \int_0^{t_{max}} \frac{f_{\rm vac}(t)}{f_{\rm vac}(0)}\, e^{i\omega t} dt \tag{5.11}$$

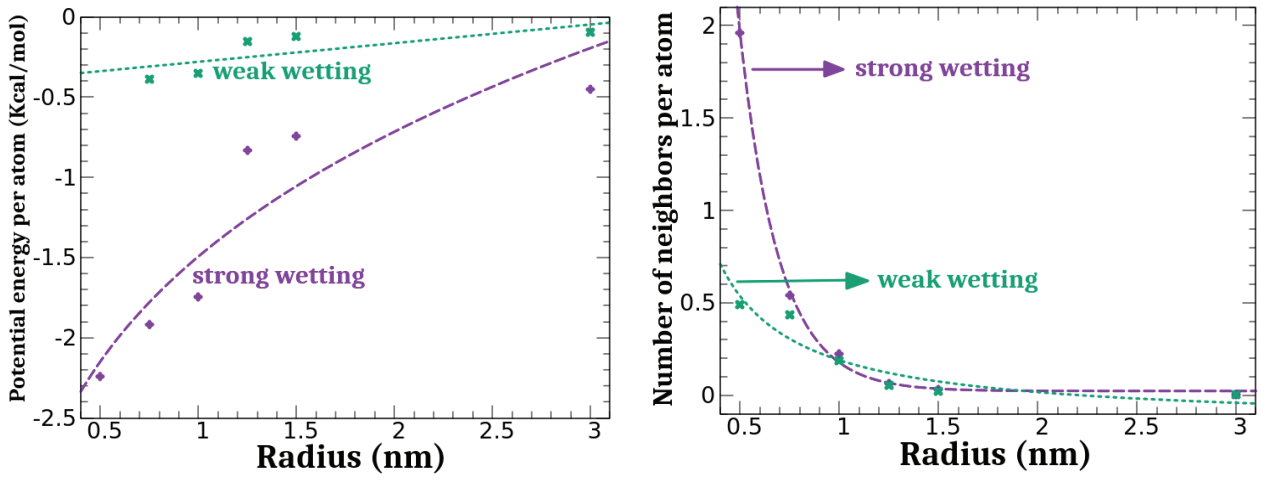

Figure 5.4: Fig. 5.4a shows, for the different wetting regimes, the potential energy (due to the interaction with water) per gold atom, as a function of the nanoparticle size. Fig. 5.4b shows the average number of neighbor oxygens of the gold atoms. Fig. 5.4c shows the thermal conductance as a function of the number of neighbor oxygens of the gold atoms.

$t_{\max} = 10$ ps in the simulations. The f_{vac} has been calculated under steady heat flux conditions using ten different trajectories. The integral is discretized in time intervals of 1 fs, so we collect 10,000 values from each trajectory. The f_{vac} is computed in the following way:

$$f_{\text{vac}}(t) = \langle \mathbf{v}(t) \cdot \mathbf{v}(0) \rangle = \frac{1}{3N_m} \sum_{k=1}^{N_m} \mathbf{v}_k(t) \cdot \mathbf{v}_k(0) \tag{5.12}$$

N_m is the total number of atoms of species m (oxygen or gold atoms), and the factor 3 corresponds to the system dimensionality.

Since we are interested in interfacial heat transfer, we calculate f_{vac} for atoms located at the interface of the nanoparticle-water system. We consider the oxygens that are in the first solvation layer. These oxygens are located close to the first peak of the water density profile surrounding the nanoparticle, as shown in the upper right corner of Fig. 5.3a. Typically, this first solvation layer is 5 Å thick. As concerns the atoms of the nanoparticle, we consider only those that are in the interval $0.90R_{\text{np}} \leq r \leq 1.0R_{\text{np}}$. The density of states derived from Eqs. (5.11) and (5.12) is:

$$P(\omega) = |\widehat{f}_{vac}(\omega)|. \tag{5.13}$$

The most striking feature displayed by the nanoparticle DoS as seen in Figs. 5.5a and 5.5c is the enhancement of the low frequency peak for small nanoparticles for both wetting regimes. This peak corresponds to the low frequency van Hove singularity and has been previously observed in other works [35,67]. As the dimensions of the nanoparticles are reduced, the peak located at the frequency ~ 3.2 THz is shifted to lower frequencies. For big nanoparticles, one can observe a second peak at high frequency ~ 4.8 THz corresponding to the longitudinal singularity of gold, and this peak is faded out for the 1 nm nanoparticle.

Concerning the DoS characterizing the oxygen atoms, Figs. 5.5b and 5.5d show that when the nanoparticle radius decreases, firstly the amplitude of the low frequency peak (~ 1.6 THz) is enhanced and secondly, a plateau structured appears for intermediate frequencies, between 3.2 THz and 8 THz. This plateau has been also observed in previous studies [101, 102].

In order to quantify the overlap of vibrational states between two media, we introduce the following quantity [103]:

$$\text{Overlap} = \frac{\int P_{\text{np}}(\omega) P_O(\omega) d\omega}{\int P_{\text{np}}(\omega) d\omega \int P_O(\omega) d\omega} \tag{5.14}$$

$P_{\text{np}}(\omega)$ and $P_O(\omega)$ are the DoS of the nanoparticle atoms and of the oxygen atoms at the interface, respectively. The resulting overlap is presented in Fig. 5.5e. As the diameter of the nanoparticle decreases, the overlap increases. Such overlap is related to the good matching between the low frequency peak in the nanoparticle DoS (around 1.9 THz) and low frequency peak of oxygen atoms (around 1.6 THz). This enhanced overlap contributes partly to facilitate the interfacial heat transfer between small nanoparticles and liquid water.

Fig. 5.5f shows the maximal value of the DoS function as a function of the nanoparticle diameter, and in the inset the angular frequency corresponding to the low frequency DoS peak as a function of the nanoparticle diameter. As can be seen, while the size of the nanoparticle decreases, the amplitude of the first peak increases and the frequency at which this peak occurs shifts to lower frequencies.

5.1.6 Transient simulations: comparison with the continuum model

Once we determined the size dependent thermal conductance, we assess here the accuracy of continuous heat equations model to describe heat transfer around very small nanoparticles heated at high temperatures. To this end, we use transient molecular dynamics of small nanoparticles initially heated up at different temperatures and free to cool down, as described in section 3.2.4. The nanoparticles have diameters ranging from 1 to 3 nm, and have either strong wetting or weak wetting interaction with water.

We consider the following continuum medium model for the nanoparticle and water. The heat diffusion equation and the initial condition for the nanoparticle are:

$$\frac{\partial^2 (rT_{np})}{\partial r^2} = \frac{1}{\alpha_{np}} \frac{\partial (rT_{np})}{\partial t}, \qquad \frac{\partial T_{np}(r,t)}{\partial r}|_{r=0} = 0, \qquad T_{np}(r,0) = T_{np0}. \tag{5.15}$$

The boundary condition between the nanoparticle and water at the interface is given by the expression:

$$-\lambda_{np} \frac{\partial T_{\text{np}}(r,t)}{\partial r}|_{r=R_{\text{np}}} = G_k \left(T_{\text{np}}(R_{\text{np}},t) - T_{\text{w}}(R_{\text{np}},t) \right).$$

On the other side, the heat diffusion equation and the initial condition for water are:

$$\frac{\partial^2 (rT_{\text{w}})}{\partial r^2} = \frac{1}{\alpha_{\text{w}}} \frac{\partial (rT_{\text{w}})}{\partial t}, \qquad T_{\text{w}}(r \to \infty, t) = T_{\text{w}0}, \qquad T_{\text{w}}(R_{\text{np}},0) = T_{\text{w}0}. \tag{5.16}$$

The boundary condition between the nanoparticle and water at the interface satisfies the following expression:

$$\lambda_{np} \frac{\partial T_{\text{np}}(r,t)}{\partial r}|_{r=R_{\text{np}}} = \lambda_{\text{w}} \frac{\partial T_{\text{w}}(r,t)}{\partial r}|_{r=R_{\text{np}}}$$

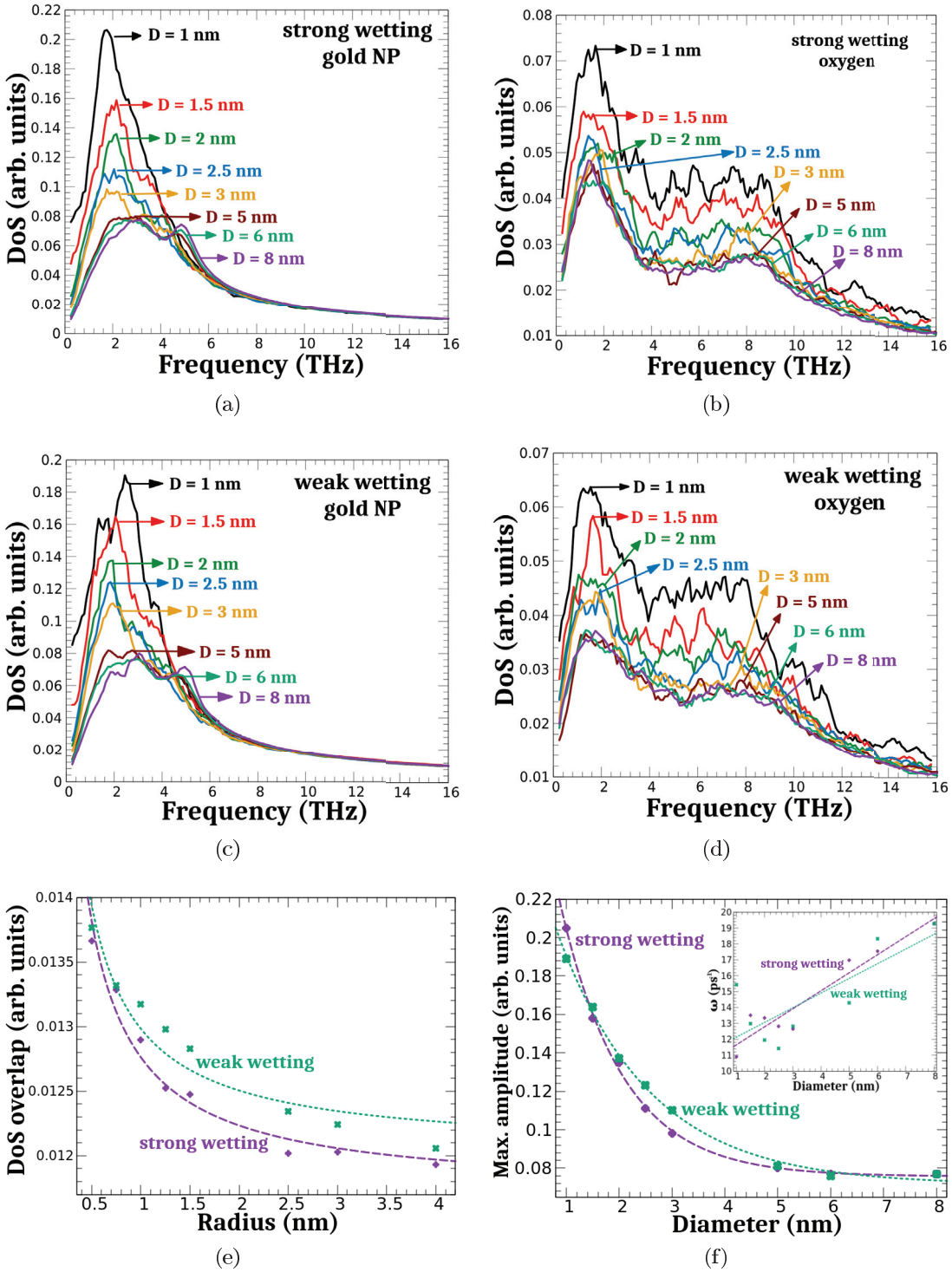

Figure 5.5: Figs. 5.5a and 5.5b represent the Density of States (DoS) of the interfacial gold and interfacial oxygen atoms, respectively, for strongly wetting nanoparticles of varying diameters, D. The same is shown for weak wetting in Figs. 5.5c and 5.5d. Fig. 5.5e displays the DoS overlap between the interfacial gold atoms and the oxygen atoms as a function of the nanoparticle radius. Fig. 5.5f shows the maximal value of the DoS function as a function of the nanoparticle diameter. The angular frequency corresponding to the low frequency DoS peak as a function of the nanoparticle diameter is also provided.

$T_{\rm np}$ is the temperature of the nanoparticle at a distance r and time t, $\alpha_{\rm np}$ is the nanoparticle thermal diffusivity, $R_{\rm np}$ is the nanoparticle radius, and λ_{np} the thermal conductivity. Similar definitions of T_w and α_w are adopted for water. The thermal diffusivities are defined by $\alpha = \lambda/(\rho c_p)$, where λ is the thermal conductivity, ρ is the density, and c_p the specific heat capacity. The value $T_{\rm np0}$ is the initial temperature of the nanoparticle.

A finite-difference method is employed to solve the coupled Eqs. 5.15 and 5.16. The thermophysical parameters of the fluid and the nanoparticle are provided in Tab. 5.2. We also use the values of $G_{\rm K}$ determined in a previous section, which were reported in Fig. 5.2. We focus attention on the

Parameter	**Value**	**Reference**
λ_{np}	1.7 W/(m K)	[67,104,105]
$\lambda_{\rm w}$	1.01 W/(K m)	[106]
$c_{p,np}$	129 J/(K kg)	[107]
$c_{p,w}$	4184 J/(K kg)	[108]
ρ_{np}	19.3 g/cm^3	[109]
ρ_w	–	MD data

Table 5.2: Physical parameters of the continuum model.

temperature evolution of water at a distance of 4 Å from the nanoparticle surface. The predictions of the continuum model together with the molecular dynamics data are depicted in Fig. 5.7.

Fig. 5.6 shows the cooling time of water in the vicinity of 4 Å from the surface of the nanoparticle. When the water temperature is lower than 301 K according to the continuum model, water is considered to be cooled down.

The cooling time increases with the nanoparticle size, as seen in Fig. 5.6. The cooling time is longer for weakly wetting nanoparticles than for strongly wetting nanoparticles. For example, for the 3 nm nanoparticles we have 20 - 30 ps difference in the cooling time for initial temperatures of 600 and 1200 K. We also observe one order of magnitude difference in the cooling time of the 1 and 3 nm nanoparticles for both wetting situations.

In order to evaluate the deviations between the molecular dynamics data and the predictions of the continuum model, we introduce the following average:

$$\% \text{ deviation} = \frac{1}{N}\sum_{t} |1 - \frac{T_{\rm MD}(t)}{T_{\rm CM}(t)}| \times 100 \tag{5.17}$$

where N is the number of MD data collected until the water (at a distance 4 Å of the nanoparticle) cools down at a temperature < 301 K according to the continuum model, $T_{\rm CM}(t)$. The temperature $T_{\rm MD}(t)$ is the temperature obtained from the MD data.

Fig. 5.8 shows the deviations between the T_{MD} and T_{CM}. The deviations increase with the initial nanoparticle temperature, without exceeding 5% in any of the considered cases. For the smallest nanoparticle, the deviations are almost constant and independent of the initial temperature.

5.2 Anharmonic effects on thermal transfer

In a very general way, for low temperatures we can conceive the approximation that interfacial heat transport is carried out with the transmission of acoustic waves at the region where the different materials are in contact. This leads us to deduce that the interfacial thermal transport is a consequence of the collision of the phonon acoustic waves at the interface. These collisions transfer the energy from

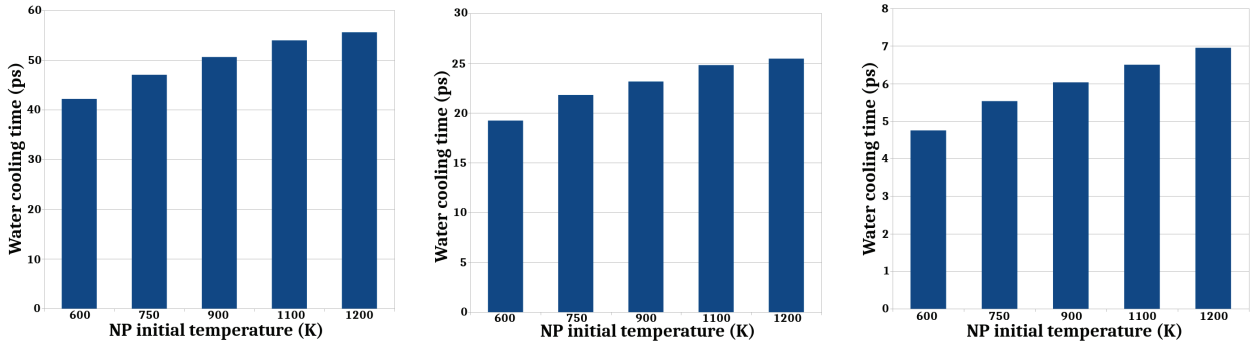

(a) Strongly wetting nanoparticle of 3 nm of diameter.

(b) Strongly wetting nanoparticle of 2 nm of diameter.

(c) Strongly wetting nanoparticle of 1 nm of diameter.

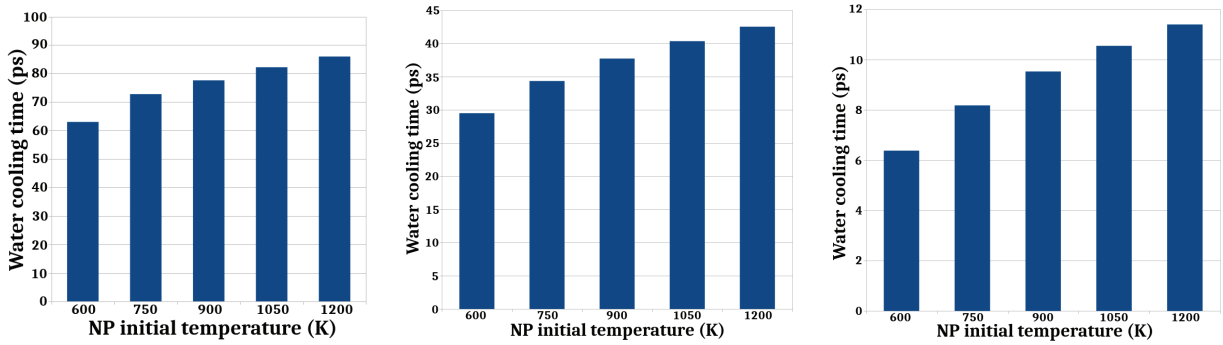

(d) Weakly wetting nanoparticle of 3 nm of diameter.

(e) Weakly wetting nanoparticle of 2 nm of diameter.

(f) Weakly wetting nanoparticle of 1 nm of diameter.

Figure 5.6: The insets show the cooling time of water vs the initial temperature of the nanoparticle. In this process the temperature of the water corresponds to that of the water molecules in the vicinity of 4 Å from the surface of the nanoparticle. Several insets are given for the different nanoparticle sizes, and the different wetting regimes.

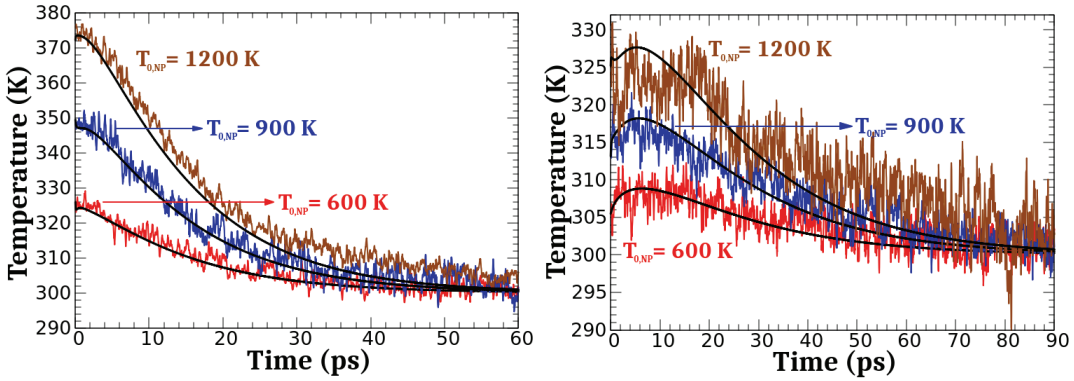

(a) (b)

Figure 5.7: Predictions of the continuum model (solid black lines) of the temperature evolution of water at a distance of 4 Å of the nanoparticle surface. Figs. 5.7a and 5.7b correspond to the strongly wetting and weakly wetting nanoparticle with diameters of 3 nm, respectively. Three different values of the initial nanoparticle temperatures are considered: 600 K (red data), 900 K (blue data), and 1200 K (brown data).

phase 1 to phase 2. When two solids are in contact, thermal transport at the solid-solid interface takes place mainly through elastic collisions, that is, between similar modes of vibration [110, 111].

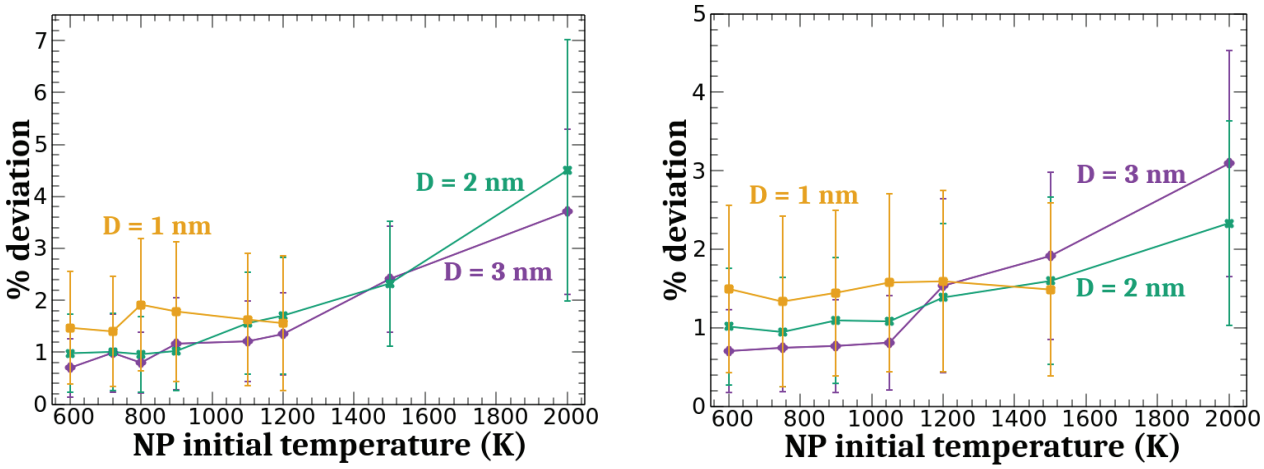

Figure 5.8: Deviations between the continuum model temperature and the molecular dynamics temperature, as given by Eq. 5.17, during the cooling stage of the water molecules surrounding the nanoparticle in the vicinity of 4 Å from the nanoparticle surface. Different initial temperatures of the nanoparticle, with three different diameters were considered. Fig. 5.8a corresponds to the strongly wetting case, and Fig. 5.8b to the weakly wetting case.

Considering that the interfacial heat transport through elastic collisions is controlled by the harmonic contribution, it is then understood that for a solid-solid interface a harmonic description of atomic vibrations turns out to be good enough, and we can neglect the other contributons for the interfacial heat transport. However, for a solid-liquid interface a harmonic description is not enough since the anharmonic contribution is more relevant than in a solid-solid interface. For the solid-liquid interface, the inelastic collisions of acoustic waves at the interface (energy transfer between different modes of vibration) are relevant and must be taken into account.

In order to understand the effect of the anharmonic contribution to thermal transport at a solid-liquid interface, we studied the thermal spectrum of the heat transfer and decompose it to analyze the harmonic and the anharmonic contributions. Also, we proceed to analyze which modes are the most relevant for nanoparticle-water interfacial heat transfer. For this, we calculate the spectral density of the heat flux and seek to relate it to other physical parameters such as the molecular mobility of the fluid close to the interface [112]. In the following sections, we will talk about this in more detail.

5.2.1 Thermal spectrum

The information on the potential energy and the vibrational density of states is encoded in the frequency dependent thermal flux defined as follows [113]:

$$q(\omega) = \frac{2}{A}\mathbf{Re}\left[\sum_{i\in Np}\sum_{j\in Ox}\int_0^{t_{max}} \langle \mathbf{F}_{ij}(\tau)\cdot\mathbf{v}_i(0)\rangle e^{i\omega\tau}d\tau\right], \tag{5.18}$$

where the real part of the quantity in brackets is considered. The nanoparticle surface area is A, $\mathbf{F}_{ij}$ is the force on the nanoparticle atom i due to the interaction with oxygen j, $\mathbf{v}_i$ the velocity of atom i, $\langle \mathbf{F}_{ij}(\tau)\cdot\mathbf{v}_i(0)\rangle$ is the correlation function between $\mathbf{F}_{ij}$ and $\mathbf{v}_i$, τ is the correlation time, and t_{max} is the maximum time.

To compute the thermal spectrum, we consider the nanoparticle atoms and oxygens in the region $[R_{\text{np}} - r_c,\ R_{\text{np}} + r_c]$, with R_{np} the nanoparticle radius and $r_c = 11.0$ Å the cut-off radius of the LJ interaction. The data is saved every 10 fs for a simulation time of 10 ps in a steady heat flux

situation. We consider 10 ps time interval for data collection because it gives enough time for the velocity autocorrelation function (VAF) to decay to zero of the oxygen near the interface, as shown in Fig. 5.9.

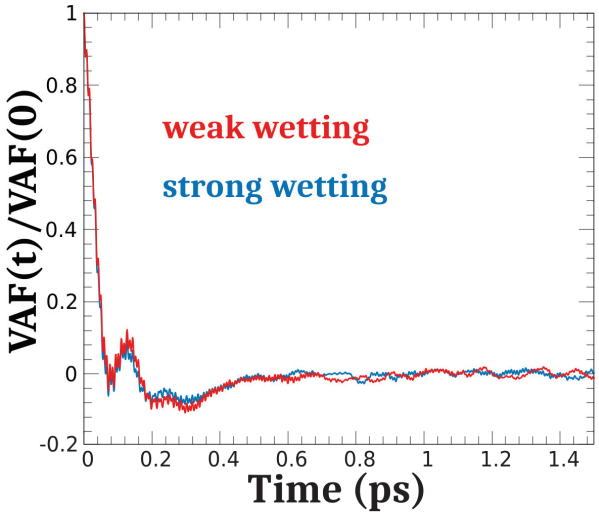

Figure 5.9: Typical behavior of the velocity autocorrelation function (VAF) of the oxygen near the interface. These cases correspond to 3 nm diameter nanoparticle with strongly and weakly wettability.

The correlation function is computed as follows:

$$\langle \mathbf{F}_{ij}(\tau) \cdot \mathbf{v}_i(0) \rangle = \frac{1}{3N_{\frac{1}{2}}} \sum_{l=0}^{N_{1/2}-1} \mathbf{F}_{ij}(\tau + l\Delta t) \cdot \mathbf{v}_i(l\Delta t) \tag{5.19}$$

$N_{1/2} = N_D/2$ with N_D the total number of data, so that each value has the same statistical weight. The factor 3 corresponds to the space dimensionality, Δt is the time interval between two data savings (every 10 fs), and t_{max} corresponds to $10ps/2$.

The frequency-dependent heat flux, $q(\omega)$, gives indication on the frequencies that dominate interfacial heat transfer. Figs. 5.10a and 5.10b show the thermal spectrum for nanoparticles with strong and weak wetting, respectively, and different diameters. The thermal spectrum displays a big peak at a frequency $\sim$ 1.6 THz independently of the type of wetting or diameter. The width of this peak is similar for all cases considered. This peak corresponds to the location of the low frequency peaks displayed by the gold atoms and the oxygen atoms, as seen in Figs 5.5a and 5.5c. This correspondance is also illustrated in Fig. 5.10c where the different density of states (DoS) have been superimposed to the thermal spectrum.

When considering nanoparticles with a diameter larger than 1 nm, a second peak is observed. In this case, the frequency of the second peak depends on wetting, and it is located at $\sim$ 5.2 THz for strong wetting and at $\sim$ 4.8 THz for weak wetting. This peak has a smaller amplitude compared to the first, and its width depends on wetting, being larger for weak wetting than strong wetting. Also, this second peak in thermal spectrum is related with the second peak in the gold DoS spectrum, as seen in Figs. 5.5a and 5.5c. In the case of the 1 nm nanoparticle, we do not mean that it does not have a second peak in its spectrum. For this nanoparticle, low frequencies become more relevant and widen the spectrum, which causes the second peak to merge with the first peak and consequently less perceptible. All these considerations highlight the role of low frequency vibrations in the enhanced heat transfer of small nanoparticles. But not only the position of the second peak in the spectrum changes when considering different wetting interactions. Another feature that changes is the amplitude of the spectrum. The amplitude of the spectrum is larger when considering stronger wetting, as observed in Fig. 5.10d. This may be explained by the strength of the interaction which is higher for strong wetting.

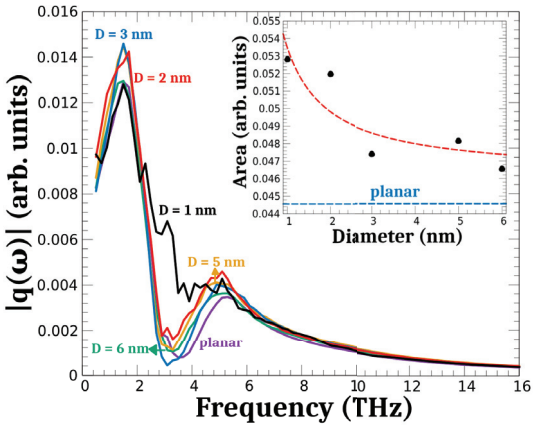

(a) Strong wetting

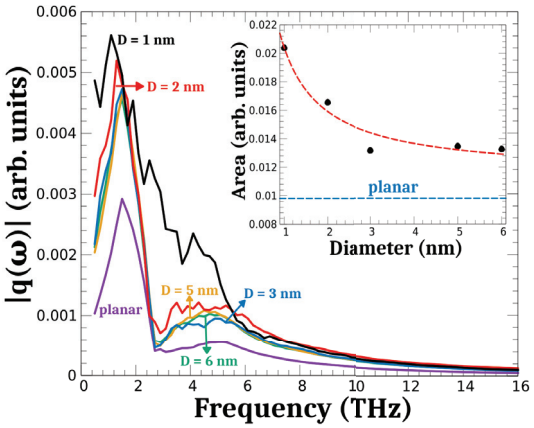

(b) Weak wetting

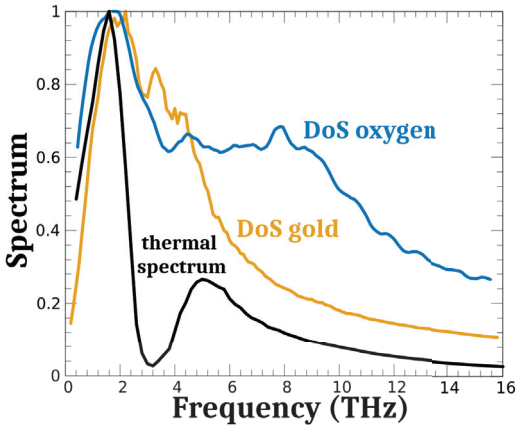

(c) Comparison of the thermal spectrum and the density of vibrational states of the oxygen and gold atoms near the interface.

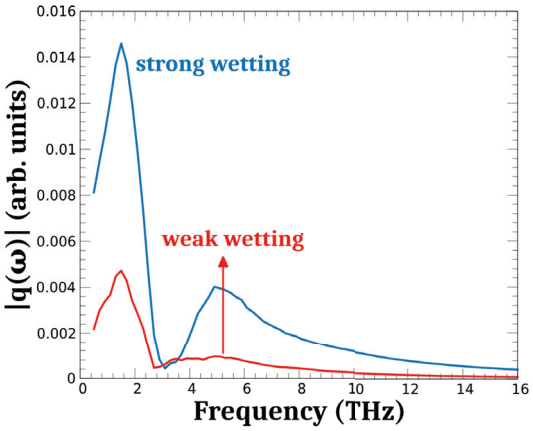

(d) Thermal spectra comparison between strong and weak wetting for the 3 nm diameter nanoparticle.

Figure 5.10: Thermal spectrum across the nanoparticle-water interface for different wetting interactions. Planar gold-water interface thermal spectrum is also shown.

5.2.2 Interfacial conductance calculated from the thermal spectrum

If we fix the type of wetting, we observe that the amplitude of the spectrum tends to be smaller when we increase the diameter of the nanoparticle. The decrease in amplitude as a function of nanoparticle diameter manifests itself as a smaller area under the curve, as shown in the inset of Figs. 5.10a and 5.10b. The thermal spectrum $q(\omega)$, given in Eq. 5.18, can be understood as the contribution of the mode ω in the flux of energy per unit time and unit area at the interface. The area under the curve of the thermal spectrum gives us the total flux of energy per unit area and unit time at the interface, J. Taking this into consideration, we can relate the area under the curve of the thermal spectrum to the interfacial thermal conductance G_{K} through the definition in Eq. 1.4 as follows [97, 110]:

$$J = \int_0^\infty \frac{d\omega}{2\pi}|q(\omega)| = G_{\mathrm{K}}\Delta T \qquad \Longrightarrow \qquad G_{\mathrm{K}} = \frac{1}{\Delta T}\int_0^\infty \frac{d\omega}{2\pi}|q(\omega)|, \tag{5.20}$$

where ΔT is the temperature jump at the interface. With all of the above, we calculate the value of G_{K} considering the thermal spectrum. Fig. 5.11 shows the value of G_{K} calculated using eq. 5.20.

As observed in Fig. 5.2, in this case also the interfacial conductance tends to increase its value as the size of the nanoparticle decreases following a behavior like $G_{\mathrm{K}} \sim 1/R_{\mathrm{np}}^n$ with $n > 0$. This result is in agreement with the fact that the amplitude of the thermal spectrum tends to decrease with increasing nanoparticle size. The values we obtain for G_{K} are lower than those presented in Fig. 5.2, however, they are still within the expected range according to experimental data [22].

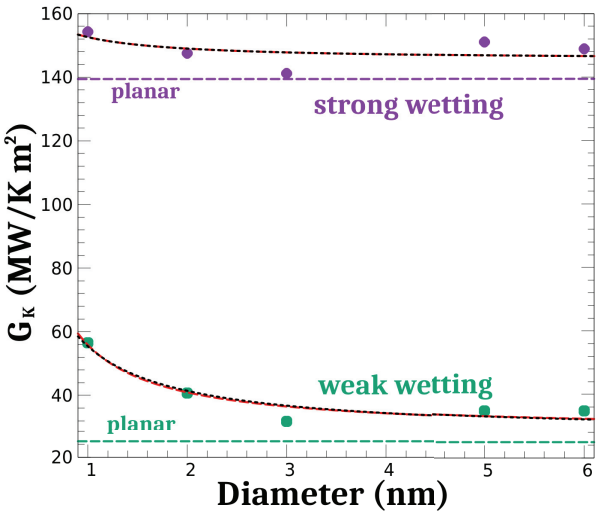

Figure 5.11: Value of the interfacial thermal conductance G_{K}, calculated using Eq. 5.20, as a function of the diameter of the nanoparticle. The red and black dashed lines correspond to the fitting of the Eqs. 5.8 and 5.9, respectively. The thermal spectra across the corresponding planar interfaces are shown as dashed lines.

5.2.3 Harmonic and anharmonic contributions

In order to study the harmonic contribution in the heat transport between the nanoparticles and the aqueous medium, we do the following. In our case, we consider that the interaction between the nanoparticle atoms and the water molecules is through a van der Waals type potential. This type of potential is characterized by having an attractive part and a repulsive part. We use the potential of Lennard-Jones 12-6 and the change from the attractive to the repulsive part occurs at distance $r_m = 2^{\frac{1}{6}}\sigma$, where σ is the distance at which the potential becomes zero.

At r_m the derivative of the potential, and therefore its associated force, is zero, and we can approximate the potential around r_m using Taylor series. Since we are interested in the harmonic contribution, we are left with only the quadratic term of the Taylor series, that is:

$$V_{LJ}(r_{ij}) - V_{LJ}(r_{ij}^{(0)}) \approx V_h(r_{ij}) = \frac{k_{ij}}{2}\left(r_{ij} - r_{ij}^{(0)}\right)^2 \qquad \text{with} \qquad k_{ij} = \frac{d^2V_{LJ}}{dr_{ij}^2}|_{r_{ij}^{(0)}}. \tag{5.21}$$

For the previous expression to be valid, $r_{ij}^{(0)}$ must be a distance close to r_m. If we consider other reference distances different than r_m, we must take into account the linear term in the Taylor series. Considering the previous expression, we propose to calculate the thermal spectrum associated with the harmonic contribution with Eq. 5.21 together with Eq. 5.18.

To calculate the harmonic contribution, we consider a time window of length of 10 ps for data collection, and we save the data every 10 fs. We calculate the average distance, $r_{ij}^{(0)}$, between the atom of nanoparticle i and the oxygen j during these 10 ps, and only consider the contribution of the pair of atoms whose average distance $r_{ij}^{(0)}$ is close to the value r_m, this is $r_m - \Delta \leq r_{ij}^{(0)} \leq r_m + \Delta$. To calculate the value of Δ we consider the distance at which V_h deviates ~ 20 % from the V_{LJ} value, and this is $\Delta = 0.25$ Å.

Fig. 5.12 shows the comparison between the total thermal spectrum and the harmonic contribution for a 5 nm diameter nanoparticle with strong and weak wetting. The behavior observed for the other diameters is similar. What we observe is that the harmonic contribution is greater for strong wetting than for weak wetting. This should be related to the fact that for strong wetting, the mobility of water molecules in the vicinity of the nanoparticle is reduced. Due to this, the water molecules have little excursion around their average positions, contributing thus to the harmonic thermal spectrum.

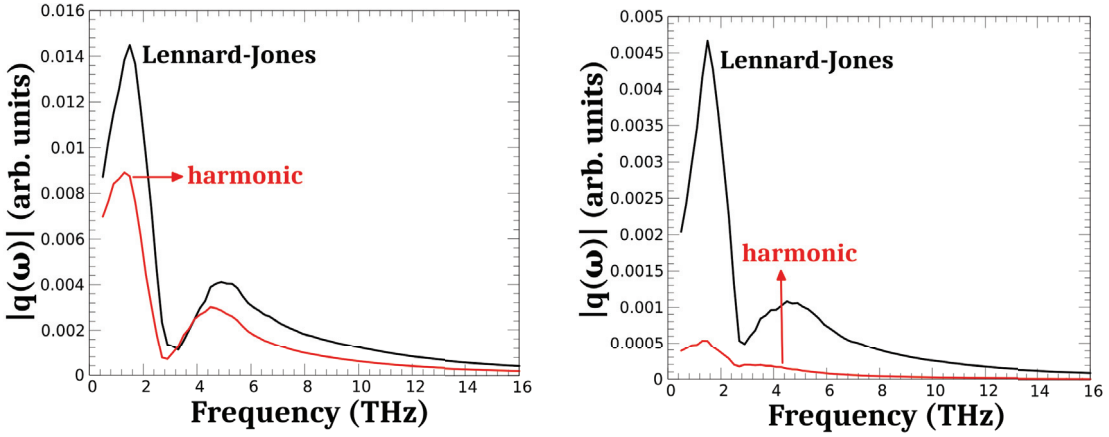

(a) Strong wetting

(b) Weak wetting

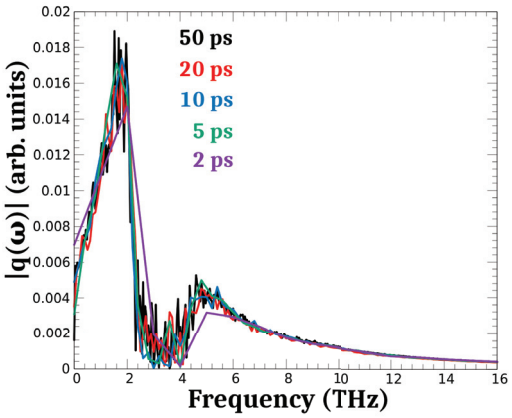

(c)

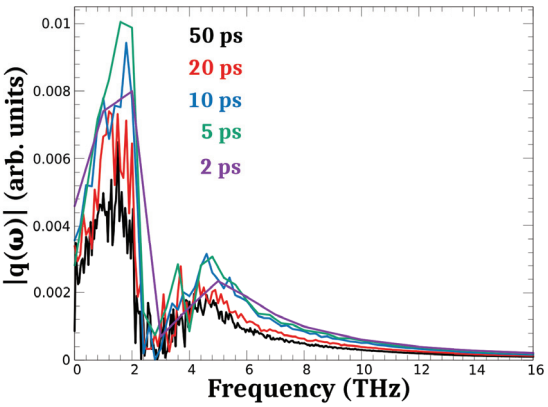

(d)

Figure 5.12: Comparison of the total thermal spectrum and the harmonic contribution for strong wetting (Fig. 5.12a) and weak wetting (Fig. 5.12b). Comparison of the thermal spectrum for different data collection time windows for the total spectrum, Fig. 5.12c, and the harmonic contribution, Fig. 5.12d. Here we consider a 5 nm diameter nanoparticle.

In order to verify that the time interval we used to collect the data is a well interval, we calculate the thermal spectra considering different time windows. The Figs. 5.12c and 5.12d show the thermal spectrum considering different data collection time windows for the total spectrum and the harmonic contribution, respectively. As observed in Fig. 5.12c, the total thermal spectrum does not show a significant change for the different time windows. In this case, the amplitude of the spectrum and the positions of its maximums are, in general, the same. Nevertheless, regarding the harmonic contribution, we see that the spectrum can change if we consider different time windows. For the 2, 5, and 10 ps time windows, the harmonic spectrum does not change significantlty. But for the 20 and 50 ps time windows, the spectrum starts to decrease in amplitude and the second maximum shifts slightly to lower frequencies. This, together with the decay of the velocity autocorrelation function shown in Fig. 5.9, allowed us to consider a time window of 10 ps.

We want to analyze the harmonic contribution calculating the ratio between the area under the curve associated with the harmonic contribution, and the area corresponding to the total spectrum. Fig. 5.13 shows the ratios of harmonic and anharmonic contributions for heat transfer. The ratio for anharmonic contribution is defined as follows:

$$\text{anharmonic ratio} = 1 - \frac{\text{harmonic contribution}}{\text{total contribution}} = \frac{\text{anharmonic contribution}}{\text{total contribution}}. \tag{5.22}$$

For strong wetting, we observe that as the size of the nanoparticle increases, the harmonic contribution increases. The harmonic contribution is even greater than 50% for strong wetting nanoparticles bigger than 3 nm in diameter, a maximum for the planar surface around $\sim$ 62%. For weak wetting, the harmonic contribution is always smaller than 18%, and we observe that the planar surface has the smallest contribution. The absence of a trend for weak wetting data may be related with the fact that the harmonic contribution is small as compared to the case of strong wetting.

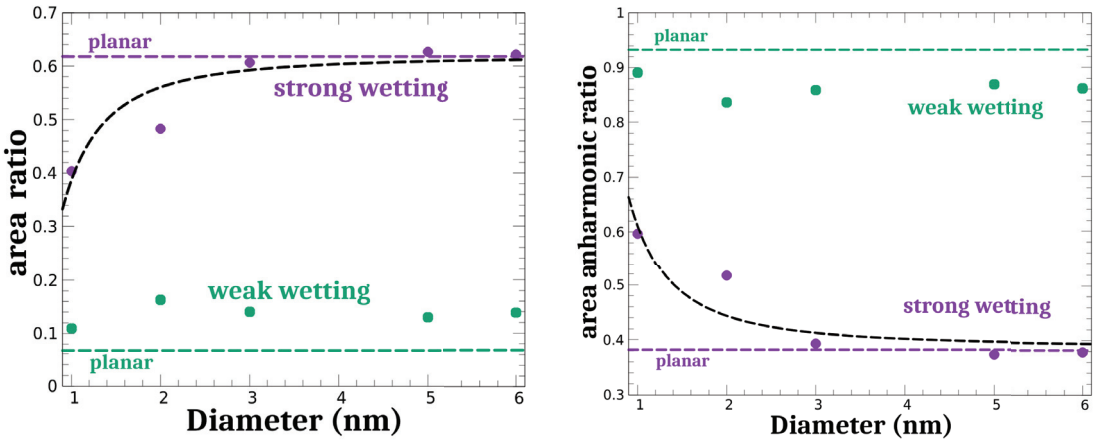

(a) (b)

Figure 5.13: Harmonic contribution, Fig. 5.13a, and anharmonic contribution, Fig. 5.13b, as a function of the diameter. The dashed black line is an exponential fit for strong wetting data.

5.2.4 Mean Square Displacement (MSD)

We aim at quantifying the relation between anharmonic interfacial heat transport and the mobility of fluid molecules near the interface. To this end, first we calculate the mean square displacement (MSD), defined as:

$$\mathrm{MSD}(t) = \frac{1}{3N}\sum_{i=1}^{N} |\mathbf{r}_i(t) - \mathbf{r}_i(0)|^2 \tag{5.23}$$

where $\mathbf{r}_i(t)$ and $\mathbf{r}_i(0)$ correspond to the position of the oxygen atom at time t and time $t = 0$, respectively, the 3 correspond to the dimensionality, and N is the number of oxygen atoms considered. We are concentrated in the MSD of the water molecules that are located in a distance smaller than 11 Å from the nanoparticle surface. When steady heat flux has been reached, the MSD is calculated every 100 fs over a period of 100 ps. The data presented are obtained after averaging over 10 different simulations for each nanoparticle size.

For times longer than $\sim$ 5 ps, MSD has a linear behavior, as observed in the inset of Fig. 5.14. This allows us to define an effective diffusion coefficient as:

$$D_{\mathrm{eff}} = \lim_{t\to\infty} \frac{d\mathrm{MSD}}{dt}. \tag{5.24}$$

In Figs. 5.14a and 5.14b, the values of D_{eff} are shown as a function of the diameter for strong wetting and weak wetting, respectively. We observe that for strong wetting, the value of D_{eff} tends to decrease with increasing nanoparticle size. Let us remember that when the size of the nanoparticle decreases, the interfacial thermal conductance G_{K} tends to decrease, as observed in Fig. 5.2. Therefore, the fact that D_{eff} decreases as well as G_{K} when the size of the nanoparticle increases could have some relation. Recent works have shown that there is a dependence between the mobility of fluid molecules and interfacial thermal conductance when considering graphene-water and graphene-perfluorohexane

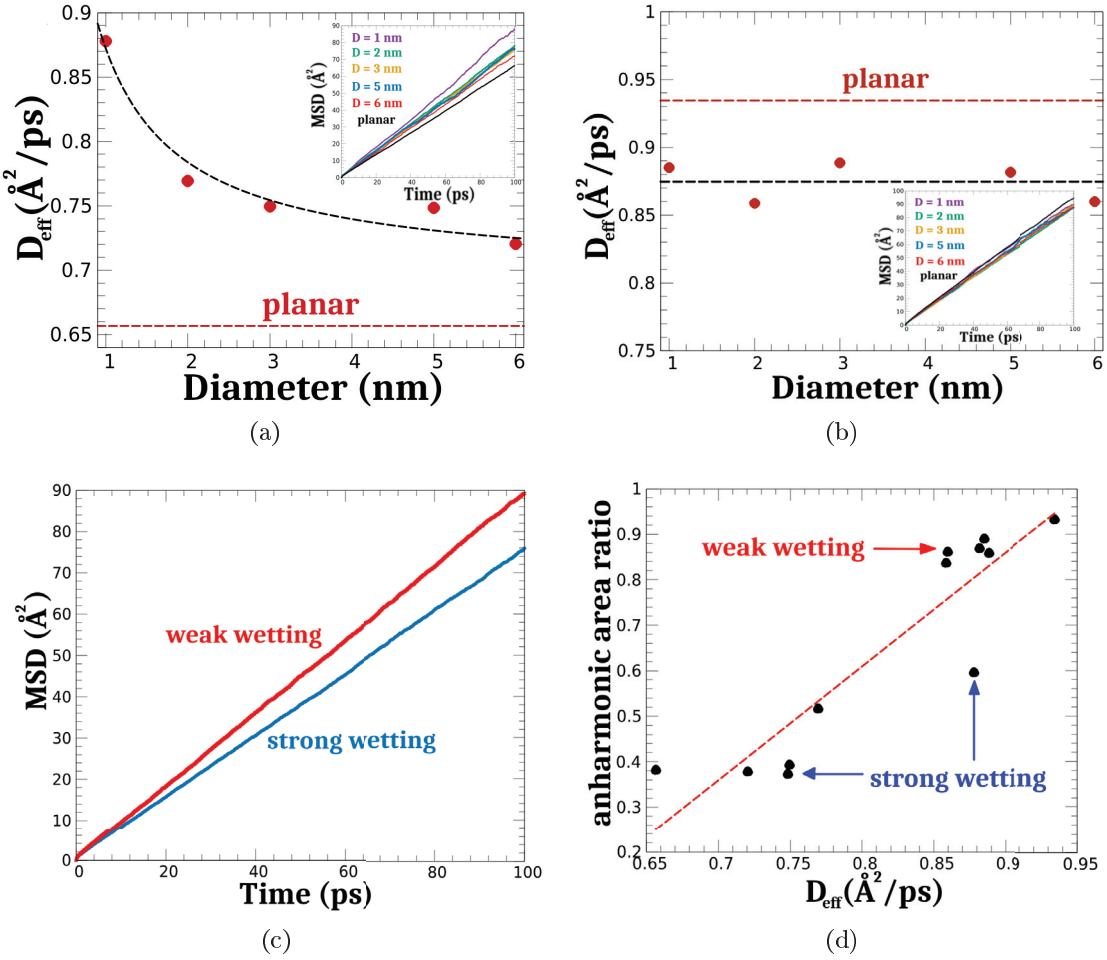

Figure 5.14: Effective diffusion coefficient D_{eff} for strong wetting, Fig. 5.14a, and weak wetting, Fig. 5.14b, as a function of the nanoparticle diameter. The error bars are smaller than the symbol sizes. In the inset of Figs. 5.14a and 5.14b, it is shown the MSD of the water near the interface as a function of time for the different nanoparticles. Fig. 5.14c shows a comparison of the MSD for the two types of wetting for the 3 nm diameter nanoparticle. A similar behavior is observed in the other cases. Fig. 5.14d shows the relation between the anharmonic area ratio of Fig. 5.13b and D_{eff}.

interfaces [112]. However, in the case of weak wetting we don't observe a strong dependence of D_{eff} with the nanoparticle diameter. Nevertheless, for G_{K} we observe that its value decreases as a function of the diameter.

In order to relate the anharmonicity of the thermal spectrum to D_{eff}, we show in Fig. 5.14d the area ratio of the anharmonic contribution, which we obtained in Fig. 5.13a, as a function of D_{eff}. The general trend we observe is a linear relation between area ratio and D_{eff}, regardless of the type of wetting. This indicate that there is a correlation between the anharmonicity of interfacial heat transfer and the mobility of water molecules in the vicinity of the nanoparticles.

Anharmonic heat transfer is relatively important for interfaces for which the mobility of water molecules is high, which correspond to planar non-wetting surfaces. Note also that, for strong wetting, the relative anharmonic contribution is high when the effective diffusion coefficient is large, which is observed for strongly curved interfaces. These considerations shed light on the origin of anharmonic heat transfer at solid-liquid interfaces. At solid-solid interfaces, anharmonic interfacial heat transfer is associated to phonon scattering taking place at the interface. By contrast, at solid-liquid interfaces, anharmonic interfacial heat transfer is mainly driven by the mobility of the liquid molecules.

5.3 Summary

With all of the results above, we can summarize the main results as follows. The metal nanoparticle-water interfacial heat transport is enhanced for small nanoparticle size. We observe this in a greater interfacial thermal conductance G_{K} when reducing the diameter of the nanoparticle. An analytical model for G_{K} is proposed to describe the simulation data taking into account, among other things, the bond strength as a function of the curvature of the interface. In order to interpret these results, different physical parameters are analyzed. A plot of the potential energy per atom at the interface shows that reducing the size of the nanoparticle increases the energy. This is due to the fact that the number of atom nanoparticle - fluid molecule bonds increases as dimensions are reduced, which makes heat transport more efficient. The spectral analysis indicates that the low frequencies of the vibration modes are the ones that contribute the most to the interfacial thermal transport for this phenomenon, being exacerbated the smaller the nanoparticle. Finally, we analyze the anharmonic contribution to the thermal transport, showing that it decreases when considering stronger wetting conditions. This can be interpreted with the fact that the fluid molecules are more strongly bound to the nanoparticle atoms, which is reflected in a lower mobility of the water molecule near the interface. This low mobility allows the atom nanoparticle - water molecule interaction to be carried out with greater approximation to a harmonic type description, which makes the anharmonic contribution to the transport of heat less relevant.

Chapter 6

Cavitation around heated nanoparticles in water: effects of wetting, size, and shape

When the heating of the nanoparticle is strong, it can promote the liquid-vapor phase transition of the surrounding fluid. In this Chapter, we will present the results and their discussion for the case in which the heating of the nanoparticle is high enough to generate a liquid-vapor phase transition of the surrounding water. The nanoparticles we consider have different sizes, geometries, and wetting conditions, as well as being immersed in a pool of water. Our results show that the minimum liquid temperature for nucleation strongly depends on the type of wetting, and it can be 100 K lower than the spinodal temperature for weak wettability. Furthermore, we show that the nucleation temperature depends not only on the type of wetting, but also on the geometry and size of the nanoparticle.

First, we focus on studying the effects of wetting on the nucleation phenomenon around metallic nanoparticles, and later we analyze the effect of the size and geometry. The nanoparticles are abruptly heated every 40 ps, recreating ultra-short pulsed laser experiments. The main results we obtain are presented below.

6.1 Effect of wetting on cavitation

Here, we first consider a nanoparticle of 11 nm in diameter that initially occupies a volume fraction of 10%. The phenomenon of nucleation and cavitation around a metallic nanoparticle as a function of its wetting shows the following characteristics.

6.1.1 Explosive nanocavitation

When analyzing the temporal evolution of the volume of the system, we observe that it has a strongly pronounced growth when nanocavitation begins, as seen in Fig. 6.1. It is also observed that the time to start the nanocavitation depends on wetting, and is the shortest for strong wetting. We are considering three different wetting regimes: strong, intermediate, and weak wetting. For any of these regimes, nanocavitation occurs in an explosive way. What is different is the time to reach nanocavitation. Strong wetting nanoparticles transfer their energy to the liquid more efficiently than weak wetting nanoparticles, which is reflected in the nanocavitation time, as we will also analyze later on.

6.1.2 Temporal evolution

The radial profiles of water density are different for the different regimes, as seen in Fig. 6.2. For the strong wetting case, it is observed that a $\sim$ 1 nm width layer of water near the nanoparticle surface shows pronounced layering, as seen in Fig. 6.2a. This layering may be characterized by the peaks in the density profile in the regions close to the surface of the nanoparticle, and is partially lost when the nanoparticle begins to heat up. However, a $\sim$ 6 Å width layer maintains a high density compared to distant regions. This water layer has been observed previously [32,114], and it is a stable superheated

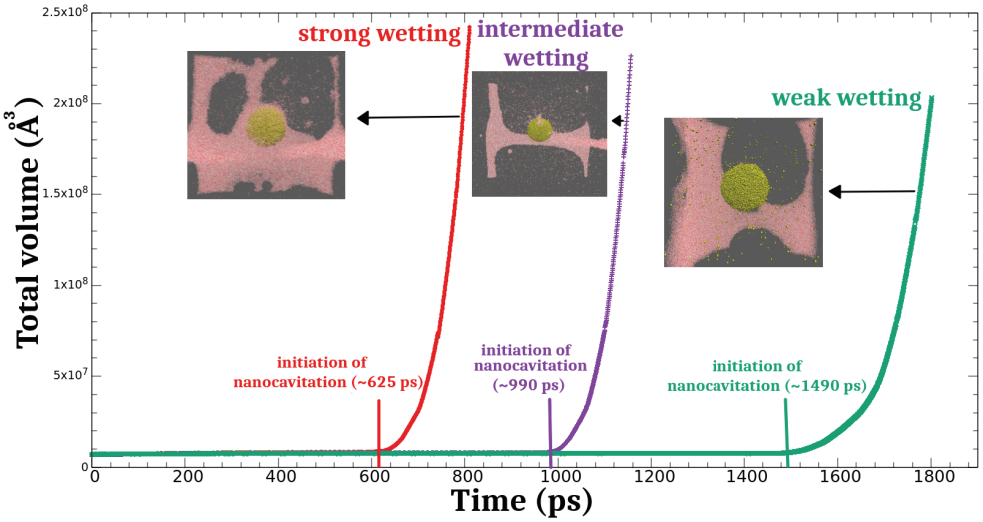

Figure 6.1: Temporal evolution of the total volume of the system for the different wetting regimes when the nanoparticle is heated up at 2500 K.

liquid layer that it is related to the strong interaction between nanoparticle atoms and water molecules.

For strong wetting, the nanobubble nucleation does not begin next to the nanoparticle surface, but at a distance of $\sim$ 1 nm from it. This is also related with the strong interactions at the interface, which keep the superheated layer 'stuck' to the surface. For the intermediate wetting, also there is initially a spatial ordering of the fluid near the interface, as seen in Fig. 6.2b. However, the peaks have lower amplitude than in the strong wetting. Furthermore, the superheated liquid layer is also observed for this wetting.We observe that nucleation begins at distant regions, but the effect is less pronunced than for the strong wetting case. For the weak wetting, an ordering of the density profile is also observed. However, it is lost more quickly when the nanoparticle begins to be heated as compared with the other cases, as seen in Fig. 6.2c. This is related with the weak interactions. In this case, there is no superheated liquid layer, and nanocavitation begins in the regions next to the nanoparticle surface.

For each wetting, it is observed that when heating the nanoparticle, the water close to the interface tends to move away from it. This is observed for the region between the surface of the nanoparticle and the first layer of superheated water. This creates a thin vapor layer that surrounds the nanoparticle, and its width depends on the wetting. This vapor layer is shown in Fig. 6.3, and the difference in width as a function of wetting is explained qualitatively with the form of the LJ potential. For short distances, the LJ potential is repulsive and when the system begins to be heated, the water molecules move away from the nanoparticle surface and enter the attractive region of the LJ potential. This attraction region is stronger for strong wetting and weaker for weak wetting, which explains why this vapor layer is thinner in the first case.

The existence of a vapor layer has been observed in other works [32,53], and here it can be observed in the radial density profiles 6.2a, 6.2b, and 6.2c. Even for weak wetting, there is a vapor layer around the nanoparticle before the first pulse, what it is seen in 6.2c for the profile computed at 20 ps. We observe that the thin vapor layer is spherical and envelops the nanoparticle. For all wetting, this thin vapor layer precedes nanocavitation and has is relatively stable before explosive growth as seen in Fig. 6.3.

For weak wetting, it is observed that the thin vapor layer lasts longer than 1 ns before nanocavitation, besides that its radius is bigger than for the other wetting. Therefore, it can be thought that for this regime it would be easier to detect experimentally the vapor layer. Also, it has been related that the generation of the vapor layer around the nanoparticle decreases the interfacial thermal

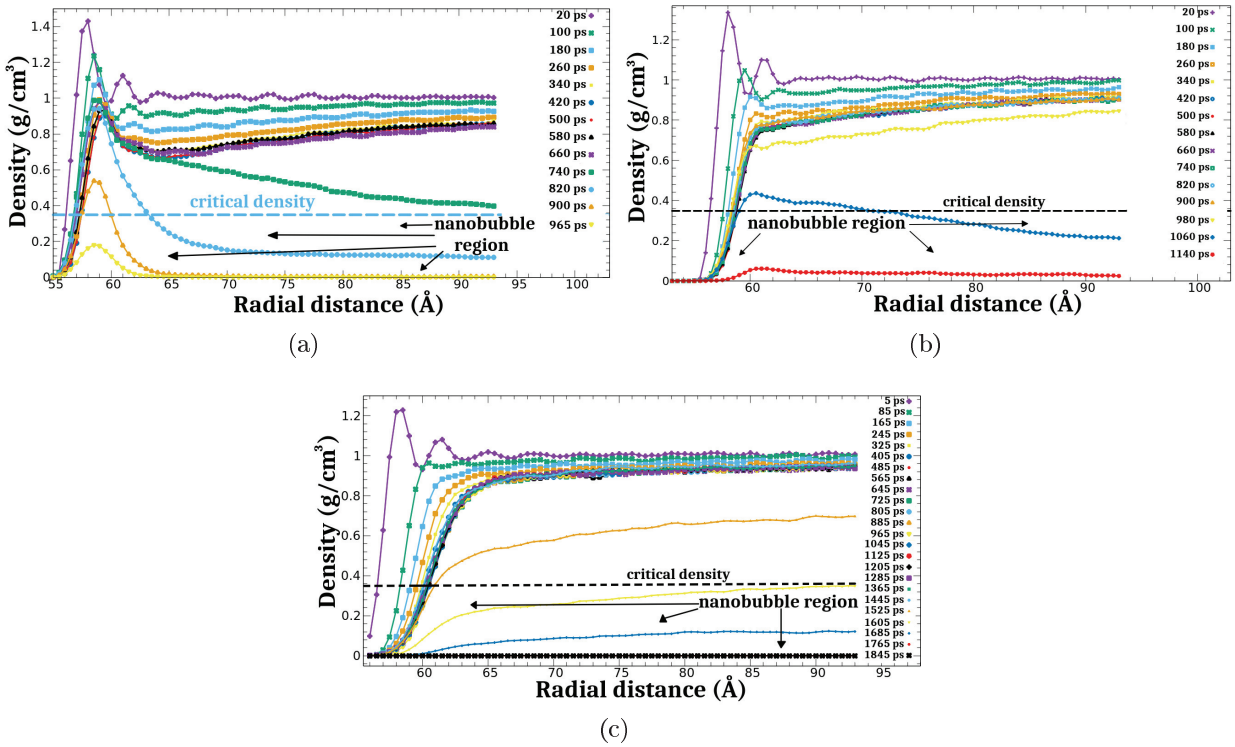

Figure 6.2: Radial water density profiles at different times for strong wetting, Fig. 6.2a, intermediate wetting, Fig. 6.2b, and weak wetting, Fig. 6.2c. The nanoparticle heating temperature is 2500 K for all these cases.

conductance [46, 48]. This is because the vapor phase has a lower thermal conductivity than the liquid, so the vapor layer around the nanoparticle plays the role of an insulator. This phenomenon could be related with a boiling crisis phenomenon, that happens when a liquid is in contact with a very hot surface. When the vapor layer is generated on the nanoparticle surface, it increases the insulating effect. This induces a critical heat flux and then drops, as temperature and the vapor film thickness increases [48]. Eventually, when nanocavitation begins, the vapor layer grows rapidly and becomes a nanobubble, as seen in the inset in Fig. 6.1 and in the rapid growth of the radius of the vapor layer surrounding the nanoparticle when cavitation begins presented in Fig. 6.3.

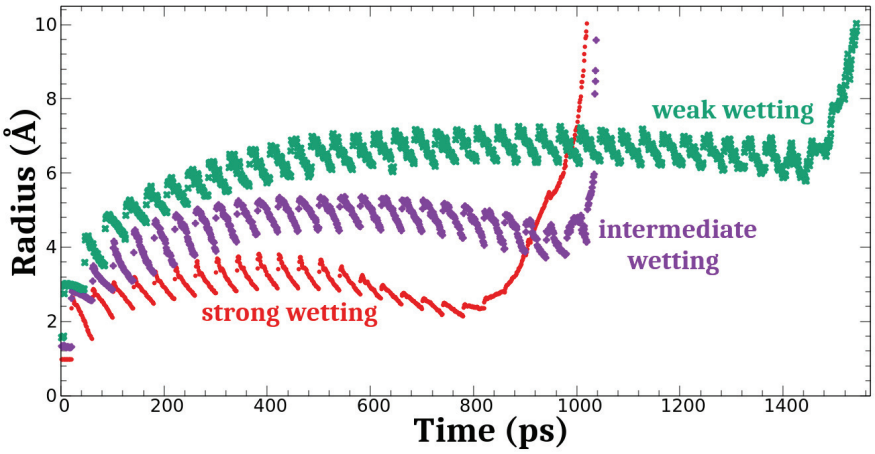

Figure 6.3: Evolution of the vapor layer before nanocavitation when the nanoparticle heating temperature is 2500 K.

We can highlight the effect of wetting when analyzing the evolution in time of the temperature and density of water surrounding the nanoparticle surface. It is observed that, for each wetting, water follows locally different paths, as seen in Fig. 6.4. Regarding the temperature, it is observed that it first increases until reaching a maximum value, and then it begins to decrease until nanocavitation starts. This behavior is more evident for strong wetting. The maximum temperature reached depends on the contact angle and is higher for strong wetting and lower for the weak wetting, as seen in Fig. 6.4. The decrease in the value of water temperature occurs even though the nanoparticle is being heated up every 40 ps.

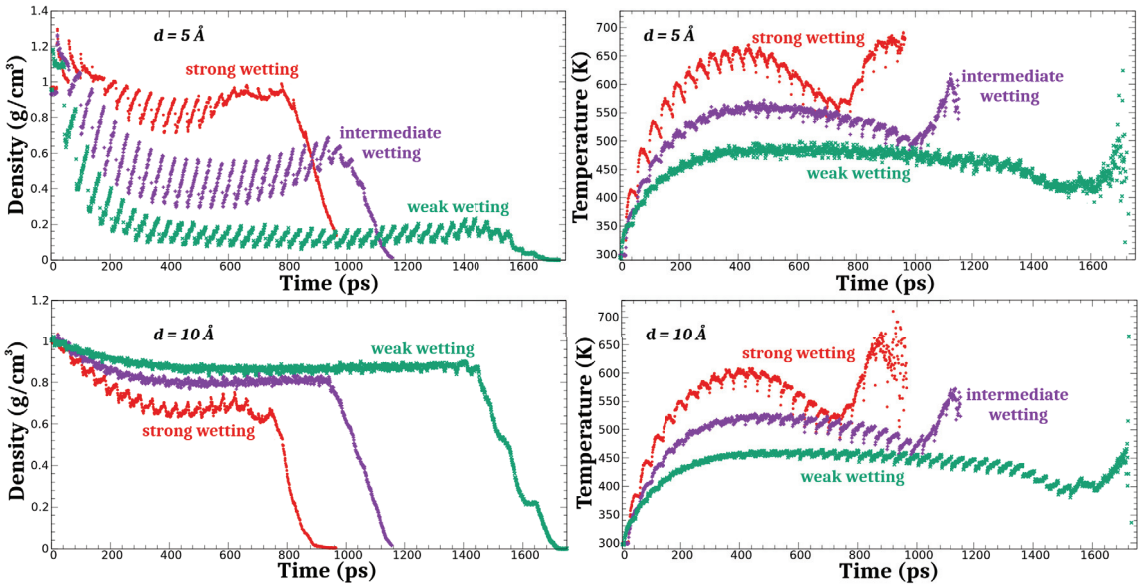

Figure 6.4: Temporal evolution of water density and temperature at different distances from the nanoparticle surface, for the three wetting regimes. The nanoparticle heating temperature is 2500 K.

To explain this behavior, we have to make several considerations. One of them is the drop of the heat flux from the nanoparticle to water. This drop in the energy flux should be related with reduction of the intefacial thermal conductance. Fig. 6.5a shows the variation in time of the interfacial thermal conductance G_{K}. We calculate this quantity by making a fit to the following exponential function $T_{NP}(t) = C_1 e^{-C_2 t} + C_3$, for the temperature of the nanoparticle when it is cooling between two consecutive heating pulses, as seen in Figure 6.5b. This exponential function corresponds to the solution of the equation $C_p \frac{dT_{NP}(t)}{dt} = -4\pi R_{NP}^2 G_{\mathrm{K}}(T_{NP}(t) - T_s)$, where $C_2 = 4\pi R_{NP}^2 G_{\mathrm{K}}/C_p$ with C_p the nanoparticle heat capacity. It is important to remark that the values G_{K} are obtained with the fitting of the data at times $t \geq 500$ fs after the nanoparticle heating. As seen in Fig. 6.5b, the first point that corresponds to the instant of the heat pulse is not taken into account because for $t < 500$ fs after the pulse, there is an internal energy distribution inside the nanoparticle that is not described by $T_{NP}(t)$.

Regarding the behavior of the interfacial thermal conductance G_{K}, it is observed that its value is not constant in time and decreases as time progresses. The decrease is strongly dependent on the wetting regime, being more evident for strong wetting, which is around 11 times smaller than at the beginning, and less for the weak wetting, which the corresponding decrease is a factor of 2. The decrease of G_{K} has been previously reported in experimental works [12,48].

6.1.3 Comparison with continuum models

This section compares several continuum models that describe the evolution of the temperature of water and of the nanoparticle. All these models consider the jump of temperature at the interface. The first one, takes into account the variation of the temperature within the nanoparticle and we call

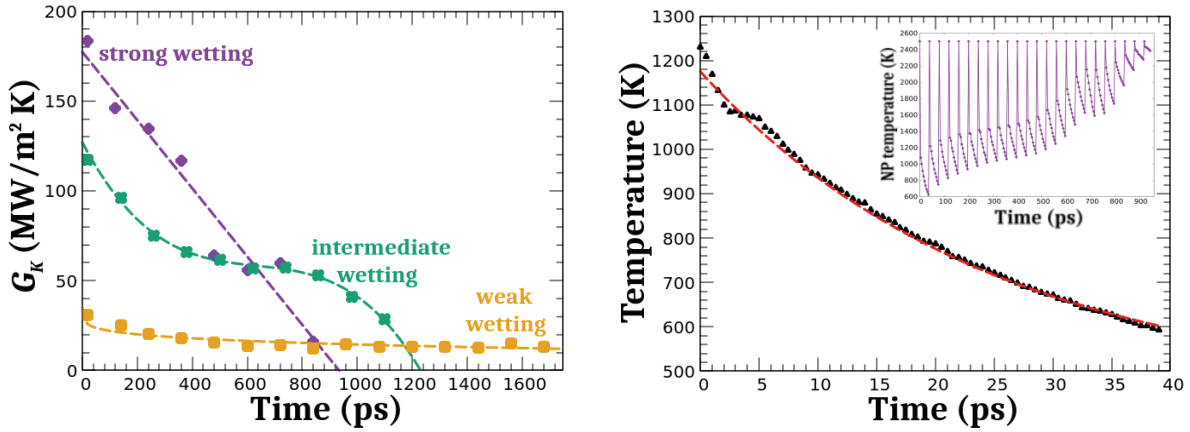

(a) (b)

Figure 6.5: Left: Interfacial thermal conductance G_{K} as a function of time. Right: Typical nanoparticle temperature profile between each heating pulse. The red dashed line corresponds to the function $T_{NP}(t) = C_1 e^{-C_2 t} + C_3$ which describes the MD data and from which we obtain G_{K}. The nanoparticle heating temperature is 2500 K.

it *Model 1*. The equations 5.15 and 5.16 in section 5.1.6 are of diffusive like.

In all the models, the value T_{np0} is considered as an "effective temperature". As previously explained, we heat the nanoparticle to a fixed temperature by rescaling the velocities of its atoms. In a time interval $t < 500$ fs, the energy supplied purely through kinetic energy is distributed internally in the nanoparticle also in the form of potential energy. This internal distribution of energy causes the temperature of the nanoparticle to drop to an effective temperature, as shown in Fig. 6.5b. We use the value of this effective temperature to set the value of T_{np0}.

The values of the interfacial thermal conductance for the Model 1, which are assumed to be constant, are the following: *i*) strong wetting: $G_{\mathrm{K}} = 138.175$ MW/(m^2 K), *ii*) intermediate wetting: $G_{\mathrm{K}} = 95.04$ MW/(m^2 K), and *iii*) weak wetting: $G_{\mathrm{K}} = 59.4$ MW/(m^2 K). These values were obtained through independent simulations for the systems used in this work with transient simulations methodology. For Model 1, we also considered the case $G_{\mathrm{K}} \to \infty$.

We consider another model, called Model 2, which takes into account that the temperature of the nanoparticle is uniform [70]. The equations are the following:

$$V_{np} C_{np} \frac{dT_{np}(t)}{dt} = -A_{np} G_k \left(T_{np}(t) - T_s(t)\right) - \Delta H_f \frac{H(T_{np} - T_f)}{\tau_f} \exp\left(-\frac{t - t_f}{\tau_f}\right) \tag{6.1}$$

where V_{np} is the volume of the nanoparticle, $C_{np} = 2.5 \times 10^6$ J/(m^3 K) is the volumetric heat capacity, A_{np} the surface of the nanoparticle, $\Delta H_f = h_m V_{\mathrm{np}}$ with $h_m = 1.24 \times 10^9$ J/m^3 the bulk melting enthalpy of gold, $H(T_{np} - T_f)$ is the Heaviside step function, $\tau_f = 30$ ps is the characteristic gold melting time. t_f is the last time when the nanoparticle exceeds the gold melting temperature, than in our case is considered as $T_f = 1200$ K taking into account size effects. $T_s(t)$ is the instantaneous surface liquid temperature obtained with Eq. 5.16.

The last model is basically the Model 2 but takes into account the variation of the interfacial conductance given in Fig. 6.5a, and we call it *Model 3*.

If we compare the predictions of the continuum medium models with the MD data, it is observed that initially they agree for the strong and intermediate wetting, as seen in Figs. 6.6a and 6.6b. However, for these two wettings, Model 1 and Model 2 predictions begin to deviate from the MD data, and this discrepancy begins at shorter times for the intermediate wetting. Model 3 describes all the

simulation data for the strong and intermediate wetting situations.

For weak wetting, the continuum medium models somehow fail to describe the MD data. This could be related with the existence of a thin vapor layer surrounding the nanoparticle, that is thicker as compared to the others wettabilities (see Figs. 6.2c and 6.3). This vapor layer acts as an insulating layer, hence heat transport for weak wetting interfaces appears to be hindered and strongly non-uniform, and continuum medium models cannot describe it.

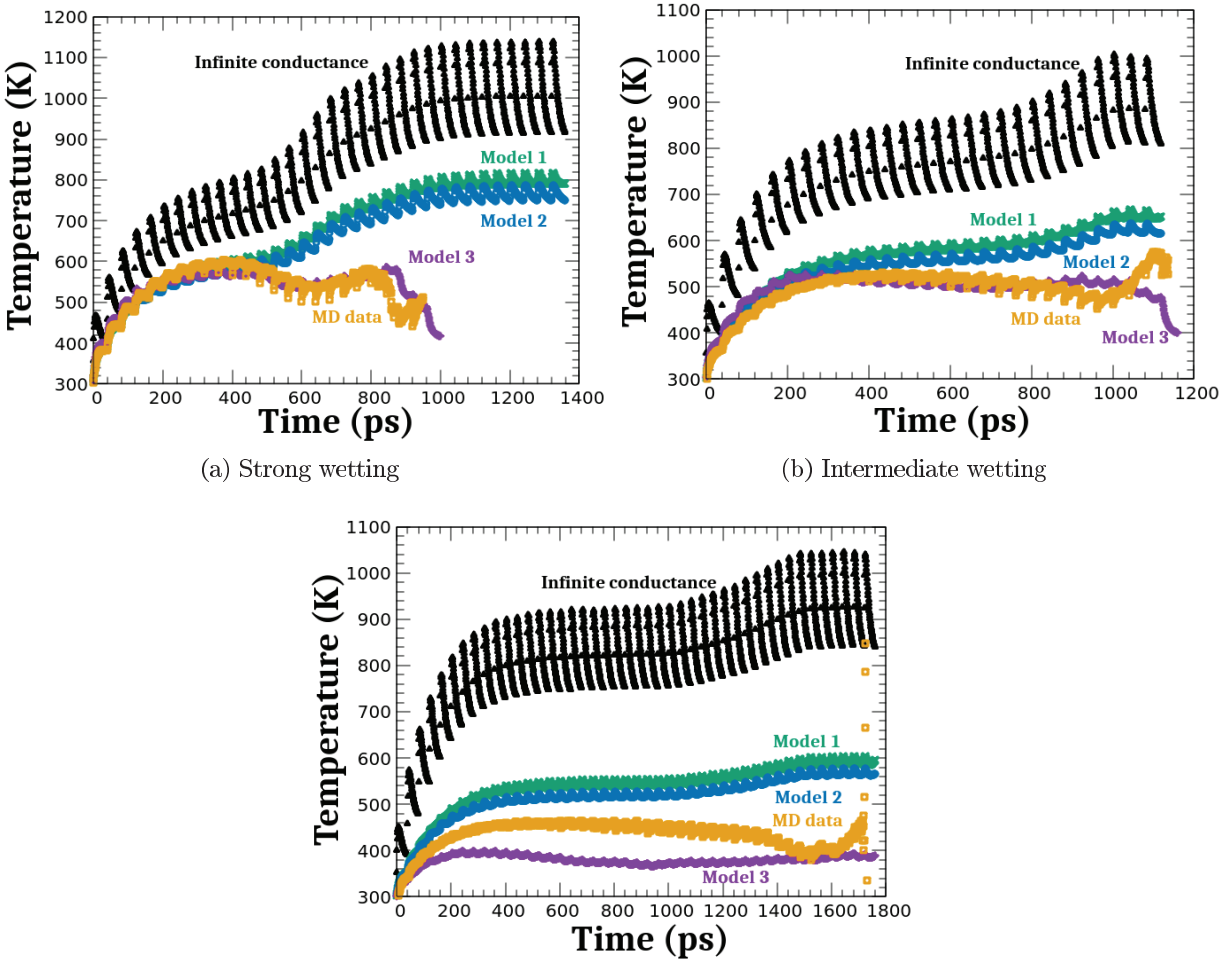

(a) Strong wetting

(b) Intermediate wetting

(c) Weak wetting

Figure 6.6: Figs. 6.6a, 6.6b, and 6.6c are the comparison between the different continuum models and Molecular Dynamic data for the temperature evolution of water at a distance of 1 nm from the nanoparticle surface.

We can also see the differences between the different continuum medium models and the MD data in the time required to reach the maximum water temperature, as seen in Fig. 6.7. Model 1, Model 2, and Model 1 with $G_K \to \infty$ yiel similar values that are hundreds of Kelvin above the MD data. Model 3 predicts values similar to those of the MD data for the strong and intermediate wetting. None of the continuum medium models can predict the time seen in the MD simulations for the weak wetting.

6.1.4 Characteristics of nanocavitation

For each wetting, before cavitation, it is observed that the maximum temperature reached by water at 1 nm from the nanoparticle surface has a linear variation with positive slope as function of the nanoparticle heating temperature, as seen in Fig. 6.8. This means that for higher nanoparticle heating

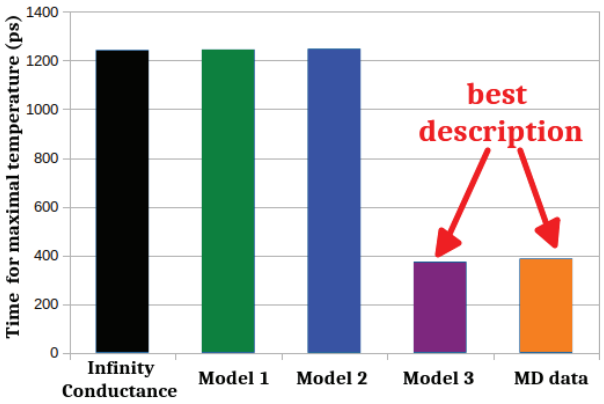

(a) Strong wetting

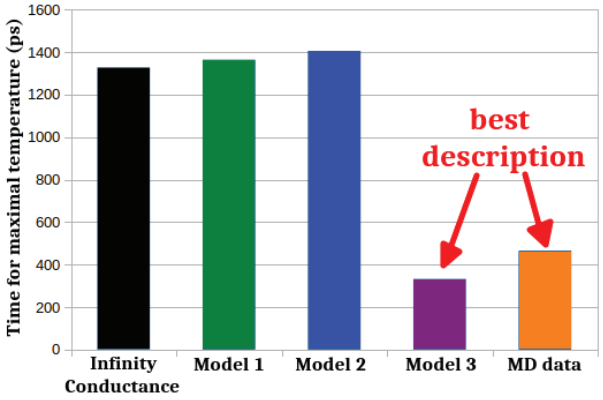

(b) Intermediate wetting

(c) Weak wetting

Figure 6.7: Comparison of the Molecular Dynamics data and the different continuum medium models for the time to reach the maximum water temperature at 1 nm from the nanoparticle surface.

temperatures, the maximum temperature reached by the water is higher. This behavior is observed for each wetting regime, but the temperature reached by water is higher for strong wetting and lower for weak wetting.

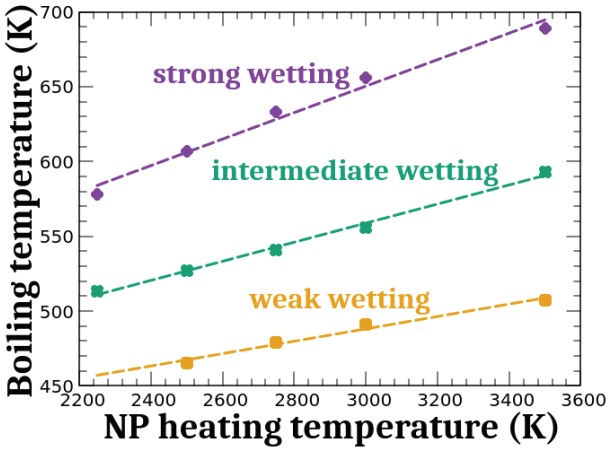

Figure 6.8: Boiling temperature for water at a distance of 1 nm from the nanoparticle surface (y-axis) vs nanoparticle heating temperature (x-axis). The dashed lines are linear functions fitted to the MD data.

The nanocavitation time depends on the contact angle, as seen in Fig. 6.1. This time is strongly dependent on wetting, as seen in Fig. 6.9. Nevertheless, the maximum temperature reached by water surrounding the nanoparticle is different for each nanoparticle heating temperature (see Fig. 6.8). Therefore, the time required to observe nanocavitation strongly depends on the wetting regime. Also, the time required to start nanocavitation is longer for weak wetting and shorter for strong wetting, which is contrary to what is predicted by isothermal classical nucleation. This can be explained with the strong or weak interactions between the nanoparticle and the fluid in each wetting, which transfer the energy to the liquid in a better way for the strong wetting than for the weak wetting.

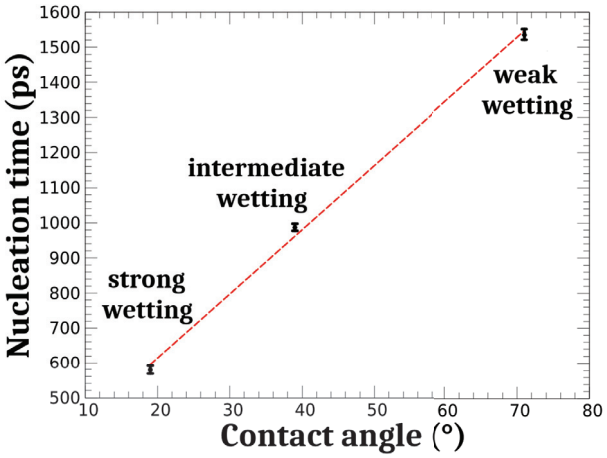

Figure 6.9: Cavitation time as a function of the contact angle. The error bars are calculated by considering the data from 10 different simulations for each type of wetting.

Continuum medium models that take into account a constant interfacial thermal conductance G_K predict longer times to reach the maximum temperature as compared to MD data, Fig. 6.7. However, if the model takes into account the variation of G_K with time, it can describe, at least qualitatively, the water temperature profile for strong wetting and intermediate wetting, as seen in Fig. 6.6. The discrepancy may be due to the fact that the continuum medium models assume that all the thermal properties, such as thermal conductivity, are uniform. However, recent works show indications that the thermal conductivity of water has a different value in the regions close to the interface, being greater than in the bulk [31].

6.1.5 Local phase diagram

We now analyze the evolution of the thermodynamic state of water close to the interface using a local phase diagram. To this end, we focus on analyzing the thermodynamic state of water located at a distance of 1 nm from the nanoparticle surface. We observed the following in Fig. 6.10a. For strong wetting, the water thermodynamic path follows the saturation line until it enters the biphasic zone at temperatures ~ 550 K. For intermediate and weak wetting we observe a similar behavior, the only difference is the temperature at which the system enters the biphasic zone when nucleation starts. These temperatures are ~ 500 K and ~ 450 K for intermediate and weak wetting, respectively.

Our results suggest that nanocavitation occurs when a layer of water having a width of $\sim 1-2$ nm exceeds an onset temperature $T_{cav}(\theta)$ and a certain nucleation time has elapsed, both depend on wetting. This onset temperature is below the critical temperature T_{cri}, $T_{cav} < T_{cri}$, and in a general way it is different than the spinodal temperature, $T_s \approx 580$ K. This is contrary to the common belief that nanocavitation occurs when the fluid spinodal temperature is crossed [115]. In addition, the nanocavitation temperature is strongly dependent on the wetting regime.

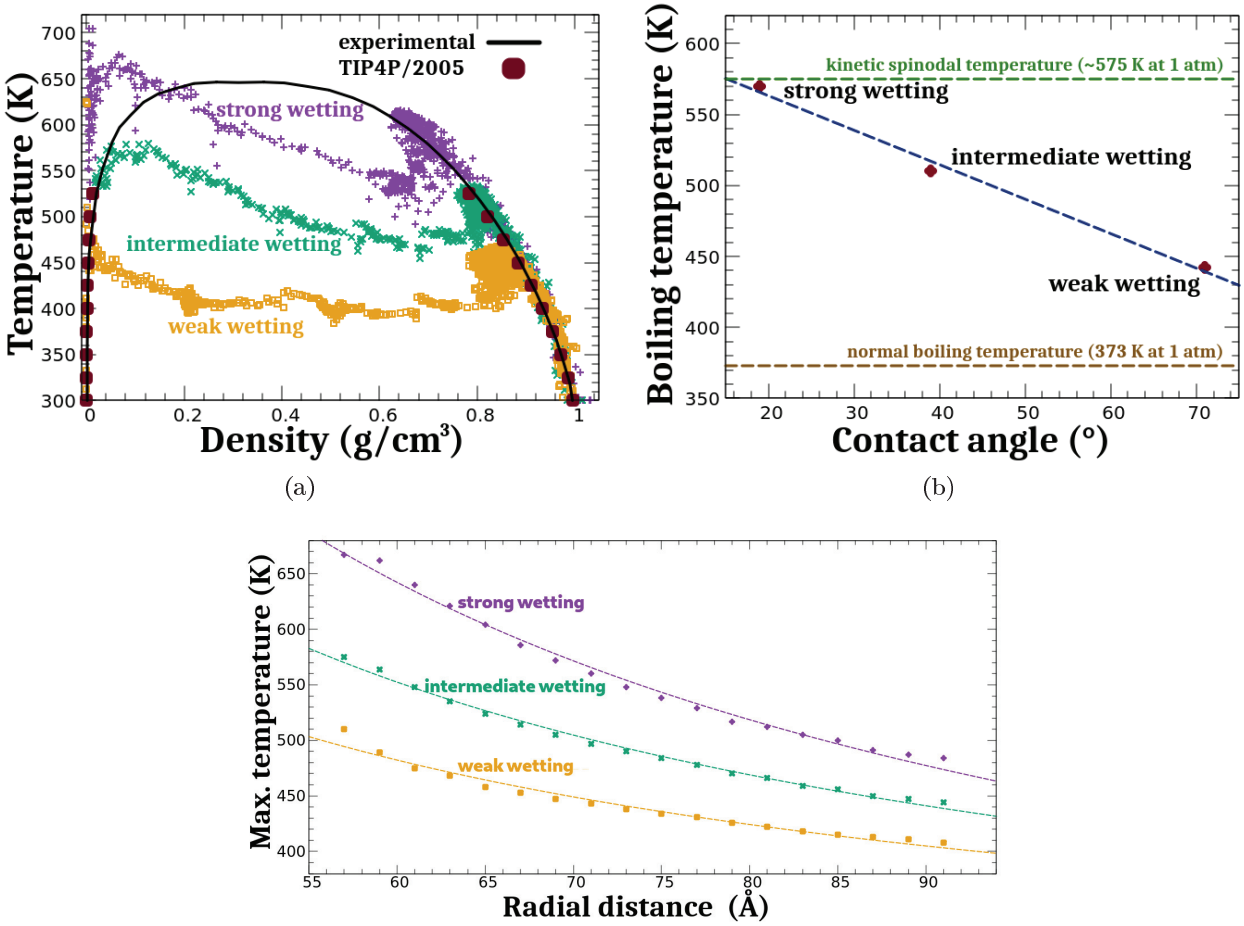

Figure 6.10: Fig. 6.10a shows the thermodynamic state followed by water at a distance of 1 nm from the nanoparticle surface for the three wetting regimes. The experimental coexistence curves are taken from [116] and for the TIP4P/2005 model from [117]. Fig. 6.10b is the minimum cavitation temperature as a function of the contact angle. Fig. 6.10c is the maximum temperature reached in water as a function of distance, and the dashed lines correspond to the $1/r$ fitting. The nanoparticle heating temperature is 2500 K for all these cases.

Another important point to remark is that nanocavitation is a 'slow' process. For all wetting regimes the time to reach nanocavitation is larger than 0.5 ns. This time is at least 10 times larger than the characteristic heat diffusion time of the bulk water over a distance $d = 1$ nm, $t_{\text{diff}} = d^2/\alpha_{\text{w}} \sim 10$ ps $<<$ 1 ns, where $\alpha_{\text{w}} = 1.5 \times 10^{-7}$ m^2/s denotes thermal diffusivity of water. In our results, nanocavitation occurs on a typical time scale of nanoseconds and is strongly controlled by the decrease in the interfacial thermal conductance prior to liquid phase change. In fact, by writing the relaxation time of the nanoparticle for the case of low conductances, $\tau_{\text{np}} = c_{\text{np}} R_{\text{np}}/(3G_{\text{K}})$ [118], we obtain that for G_{K} in the order of ~ 10 MW/(K m^2) the $\tau_{\text{np}} \sim 0.5$ ns.

6.1.6 Initial behavior of cavitation

It is observed that for timescales of a few picoseconds ($<$ 100 ps), nanobubble nucleation around the heated nanoparticle does not start in a homogeneous way, as predicted by continuum medium models [119]. This can be seen in multiple snapshots of the system before and after the starts of nucleation shown in Fig. 6.11. What is observed is that nucleation begins initially from a random point on the nanoparticle surface, and from this point is triggered phase change. This behavior is common to each wetting regime.

This non uniform nucleation is also observed in experiments. For instance, Neuman et al. did experiment where hydrophilic (strong wetting) microparticles were irradiated with pulsed lasers on the nanosecond scale [120]. They found that initial nucleation occurs only in some regions of the surface and not over the entire surface of the microparticle. However, for particles and bubbles at the nanoscale, the nucleation occurs on timescales of nanoseconds and because of this it is not easy to observe experimentally the early stages of nucleation. Neuman's results are not intuitively expected at the nanoscale, but we are observing them.

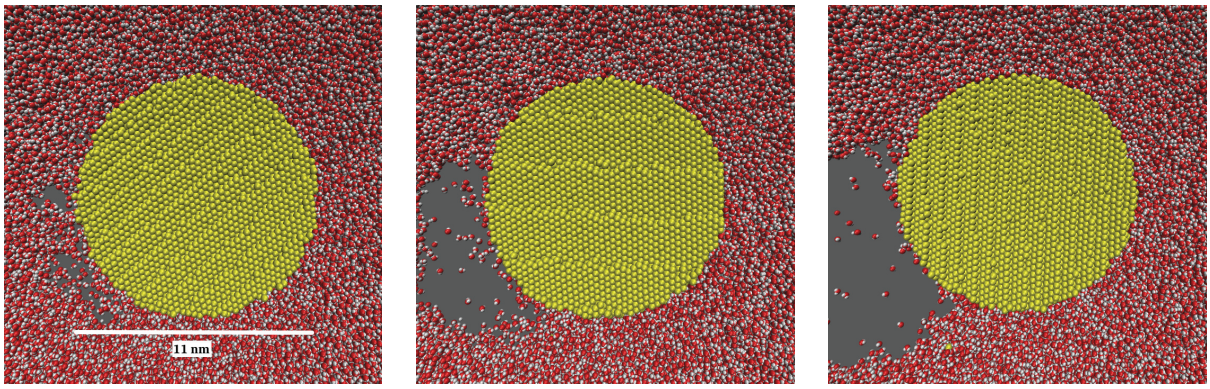

(a) (b) (c)

Figure 6.11: Snapshots of the early stages of nucleation for the strong wetting nanoparticle. Snapshots are taken every 15 ps. The start and later instants are shown from left to right. Snapshots for the intermediate and the weak wetting nanoparticles display similar behaviors.

6.2 Effects of nanoparticle size and shape-competition with fragmentation

We have analyzed the effect of wetting on the phenomenon of nanocavitation, and now we will study more systematically the role that nanoparticle size and geometry play in this phenomenon. To this end, we use spherical nanoparticles having different diameters, and nanoparticles with cylindrical (nanorod) and cubic (nanocube) geometry. In this case, the nanoparticles initially occupy a volume fraction of $\sim 2\%$.

6.2.1 Minimum size for cavitation

Fig. 6.12 shows the minimum nanoparticle diameter to observe cavitation for each wetting regime. The nanoparticle minimal size to observe cavitation depends on wetting. Furthermore, nanoparticles with intermediate and weakly wetting have equal minimum diameter of 8 nm, which is larger than the strongly wetting. Previously, Sasikumar et al. observed that, for a monoatomic fluid, the smallest nanoparticle to reach cavitation is 4 nm in diameter [53]. These results combined with ours suggest that the smallest nanoparticle size to reach cavitation depends not only on wetting, but also on the nature of the fluid. In our case, the strongly wetting nanoparticle has the smallest minimum diameter that it is 6 nm, bigger than the minimal diameter observed with the monoatomic fluid studied in [53].

6.2.2 Fluid and nanoparticle response for different heating

To observe cavitation, water surrounding the nanoparticle must reach a minimum threshold temperature, as can be seen in Fig. 6.13a. This threshold temperature increases linearly as a function of the diameter of the nanoparticle. The maximal value is observed for a planar surface and is ~ 735 K for a strong wettability. This temperature is hundreds of Kelvin above the spinodal kinetic temperature, which

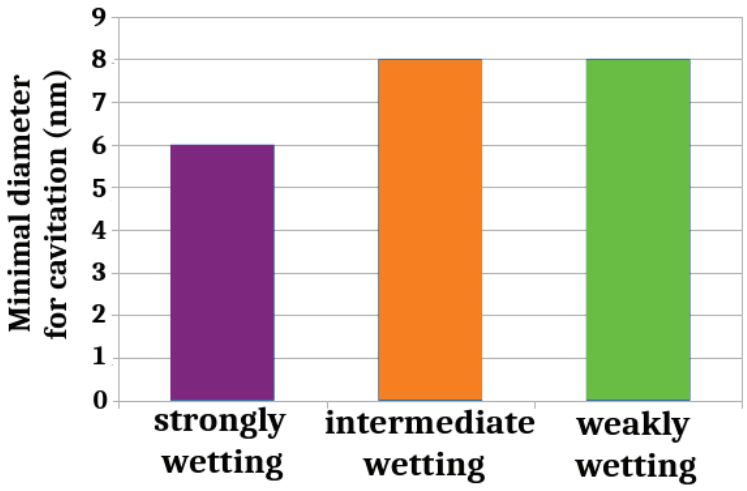

Figure 6.12: Minimal nanoparticle diameter to observe cavitation for different wettabilities.

value is $\sim$ 595 K at 1 atm [121,122]. Bulk water at a pressure of 1 atm undergoes a spontaneous liquid-vapor phase transition upon exceeding the spinodal temperature. The fact that the liquid near the planar interface can reach temperatures well above the spinodal temperature without phase transition, indicates that this liquid has locally a different behavior than bulk water and can remain trapped in a metastable state due to the interaction with the surface [123, 124].

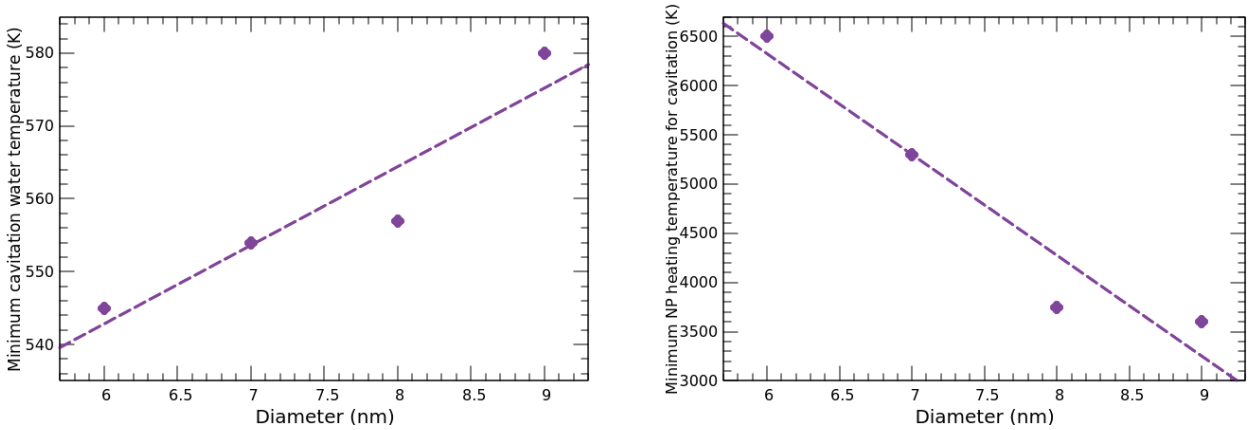

Figure 6.13: Fig. 6.13a shows the minimum cavitation water temperature at a distance of 1 nm from the nanoparticle surface, as a function of the nanoparticle diameter. Fig. 6.13b shows the minimum heating temperature of the nanoparticle necessary to observe cavitation as a function of the nanoparticle diameter. These cases correspond to the strongly wetting nanoparticle.

By reducing the nanoparticle size, higher nanoparticle heating temperatures are necessary to reach the threshold water temperature, as can be seen in Fig. 6.13b. For strong wetting nanoparticles smaller than 6 nm in diameter, the minimum nanoparticle heating temperature to reach cavitation is so high that the nanoparticle first melts. Previous works highlighted the critical role played by the curvature of the interface in the heat flux between nanoparticles and a fluid [64, 65]. As the temperature of the nanoparticle increases, a point is reached where the heat flux saturates. This behavior is related with the fact that for larger curvatures, the fluid pressure increases proportionally to the inverse of the radius of the nanoparticle (Laplace's equation). This preassure increase at the interface inhibits the phase transition of the fluid and helps explain why we need higher nanoparticle heating temperatures to drive phase transition.

As will be explained in more detail later, cavitation can occur in two different ways with respect to the integrity of the nanoparticle. In a first scenario, nanoparticle undergoes partial fragmentation and the other is when the nanoparticle is completely fragmented. In our results, we observe that the maximal temperature of the water surrounding the nanoparticle depends on whether the nanoparticle is completely fragmented or not, as can be seen in Fig. 6.14. In the case of partial fragmentation, it is observed that the maximum value of the water temperature prior to cavitation increases linearly with the nanoparticle heating temperature independently of wetting and size, as seen in Figs. 6.14a, 6.14b, 6.14c, and 6.14d. On the other hand, in case of total fragmentation, the maximum value of the water temperature prior to cavitation is constant independent of the nanoparticle heating temperature, as can be seen in Fig. 6.14b. We can relate this behavior to what has been observed in other works; when above a threshold nanoparticle temperature, the heat flux towards the fluid saturates [65]. When the energy supplied to the nanoparticle is high enough to reach this threshold, there is a part of the energy stored in the nanoparticle which serves to promote the fragmentation. Hence, it appears that saturation in the energy flux is related with the total fragmentation of the nanoparticle.

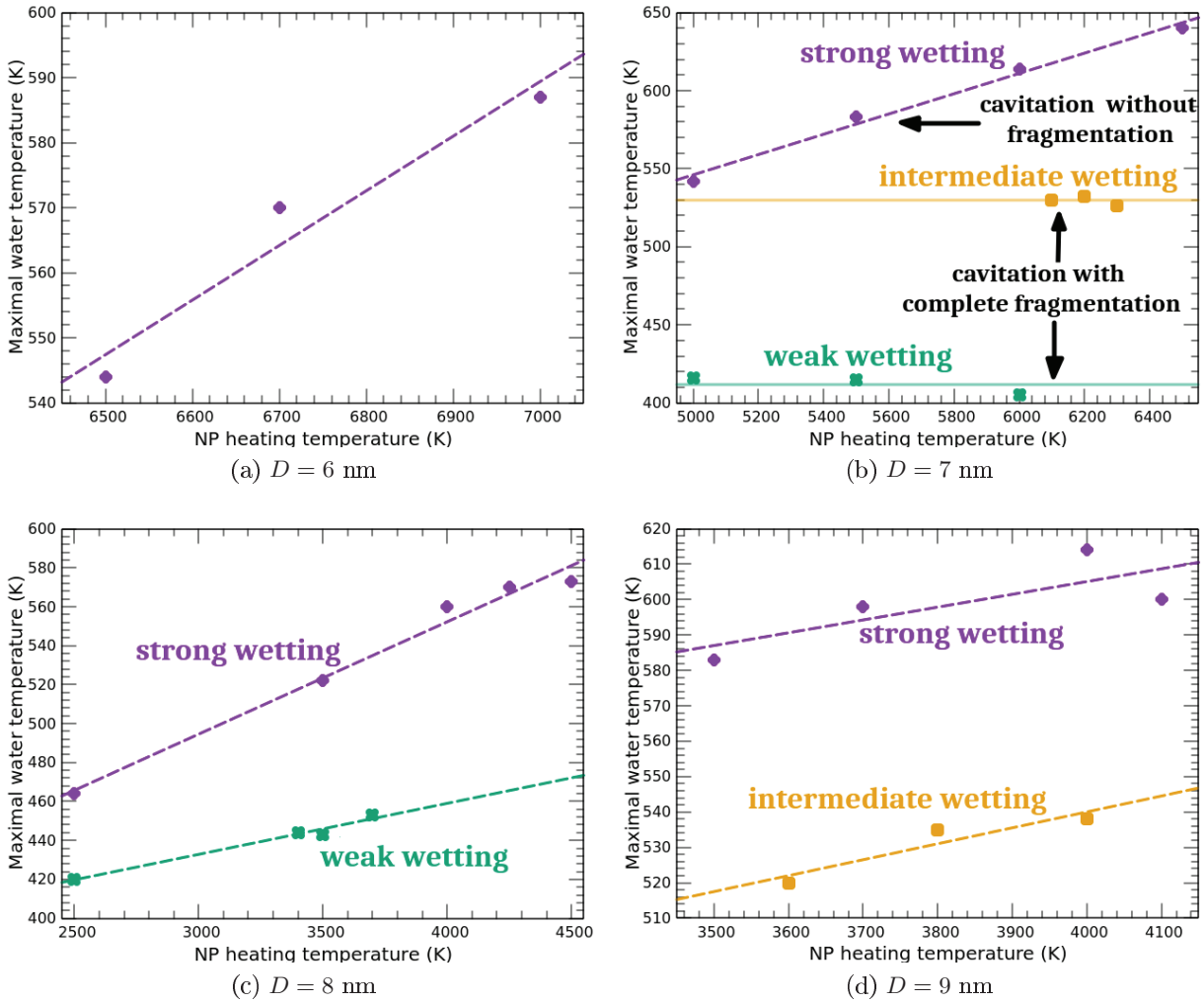

(a) $D = 6$ nm (b) $D = 7$ nm

(c) $D = 8$ nm (d) $D = 9$ nm

Figure 6.14: Maximal temperature reached by water at a distance of 1 nm from the nanoparticle surface as a function of the nanoparticle heating temperature. Different nanoparticle diameters and wettings are considered.

Fig. 6.14 summarizes the different situations encountered. We can observe various situations which depend on the value of the nanoparticle heating temperature, the size of the nanoparticle, and its wetting. These situations have the following main characteristics. If we heat the nanoparticle to

temperatures below a threshold temperature T_{l1}, the liquid surrounding the nanoparticle does not cavitate and the nanoparticle maintains its physical integrity. This threshold temperature depends on the size, geometry, and contact angle of the nanoparticle. Fig. 6.15 shows this temperature for a spherical strongly wetting nanoparticle. When we heat up the nanoparticles to temperatures lower than T_{l1}, the energy supplied to the nanoparticle and subsequently transferred to the liquid is not sufficient to promote phase transition, either in the nanoparticle or in the fluid. When T_{l1} is exceeded, the liquid surrounding the nanoparticle cavitates and the structure of the nanoparticle begins to be lost. In this case, as the nanoparticle heating temperature rises, it can be observed that the nanoparticle undergoes partial fragmentation and some of its atoms are detached, an effect being more evident for higher heating temperatures, as can be seen in Fig. 6.16.

The last case corresponds to another threshold temperature T_{l2} beyond which cavitation of the liquid occurs, and the nanoparticle is completely fragmented. The value of T_{l2} also depends on the size, geometry, and wetting of the nanoparticle, as seen in Fig. 6.15.

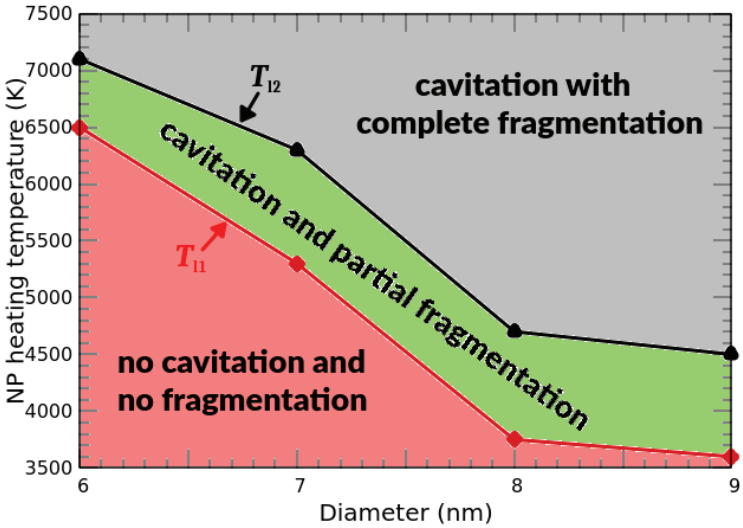

Figure 6.15: Map of the regions corresponding to the different cases: no cavitation and no fragmentation (red zone), cavitation with partial fragmentation (green zone), and cavitation with complete fragmentation (gray zone). The red line corresponds to the threshold temperature T_{l1} and black line to the threshold temperature T_{l2}, as a function of the nanoparticle size. These data correspond to a strongly wetting nanoparticle.

Fig. 6.15 shows, for strongly wetting nanoparticle, the frontiers which delimit the different cases: no cavitation and no fragmentation, cavitation with partial fragmentation, and cavitation with complete fragmentation. For diameters smaller than 6 nm, cavitation does not occur. In the case of 8 nm diameter nanoparticles with intermediate wetting, we have the following threshold values: $T_{l1} \approx 4200$ K and $T_{l2} \approx 5000$ K. In the case of 8 nm diameter nanoparticles weakly wetting, we have the following threshold values: $T_{l1} \approx 3400$ K and $T_{l2} \approx 3800$ K.

6.2.3 Local characterization of nucleation and cavitation

The high temperatures to which nanoparticles are heated periodically can cause their damage. Our simulations show that cavitation can be accompanied by partial or total fragmentation of the nanoparticle, as can be seen in Figs. 6.16 and 6.17. When we observe partial fragmentation, the nanoparticle generally retains its geometric shape and integrity. By contrast, when we observe total fragmentation, the nanoparticle completely loses its geometric shape and integrity. We focus now on cavitation without fragmentation and study in detail the nucleation phenomenon in this case.

When the nanoparticle is not fully fragmented, simulations show that the early stage of cavitation is non-uniform, as can be seen in Fig. 6.16. This non-uniform nature has been already reported in section 6.1.6. We also have shown that the phenomenon of cavitation on the nanometer length scale is closer to a nucleation phenomenon not as spinodal decomposition phenomenon. When we consider the effects of size and geometry, we have more evidence of this last point. In Fig. 6.13a is shown the minimal temperature of the liquid surrounding the nanoparticle to observe cavitation as a function of the nanoparticle diameter. We see that the minimal temperature for cavitation can be hundreds of Kelvin above the spinodal temperature for strong wetting.

In order to compare our results with those predicted by classical nucleation theory (CNT), we compute the initial bubble radius both in MD and in CNT. To calculate the initial diameter of the nanobubble in the simulations, we do the following. We consider the geometry of the system when the exponential growth of the simulation box begins, that is, when the total volume of the simulation box does not decrease with respect to the previous value. It is localized the place on the surface where the embryo starts using a visualization tool (we use VMD). A cross-section of the embryo is made and the radius of the nanobubble is measured, as shown in Fig. 6.14. As for CNT, we use the following Eq.:

$$r_c = \frac{2\gamma}{\rho_l L_f} \frac{T_b}{T - T_b} \tag{6.2}$$

where γ is the surface tension of the interface between the nucleus ant the liquid surrounding, L_f the latent heat per unit of mass, and T_b is the normal boiling temperature that for water at 1 atm is 373 K. We consider the values of T and ρ_w for the water at 1 nm from the surface just at the beginning of nucleation, and the values of $\gamma(T)$ and $L_f(T)$ at the temperature T for water.

	bubble diameter (nm)		
NP diameter (nm)	**simulation**	**CNT**	**contact angle** (degrees)
	strongly wetting		
6	2.8	0.40	99
7	4.0	0.11	109
8	4.2	0.27	111
9	4.1	0.15	115
	intermediate wetting		
8	5.9	0.41	131
	weakly wetting		
8	6.0	1.14	147

Table 6.1: Diameter of the nanobubble in the early stage of nucleation observed in simulations compared with the predictions of the classical nucleation theory (CNT), for the different nanoparticle sizes and wettabilities.

We observe in our simulations that the nanobubble diameter in the early stage depends on the nanoparticle size and on its wettability, as seen in Tab. 6.1. The general behavior is that at a fixed value of nanoparticle contact angle, the diameter of the bubble increases with the diameter of the nanoparticle. Furthermore, if we fix the diameter of the nanoparticle, the diameter of the nanobubble is larger when the wetting is weaker. This shows that the specific characteristics of nucleation depend on the type of wetting and on the curvature of the interface. Fluid molecules that are close to the interface strongly interact with the nanoparticle atoms. In order to cavitate, it is necessary to detach these molecules from the surface of the nanoparticle, which requires a certain amount of work. This energy, known as work of adhesion, depends on the type of wetting and the size of the nanoparticle. It is important to note that the radii predicted by the CNT are in general an order of magnitude smaller than what we measured in our simulations.

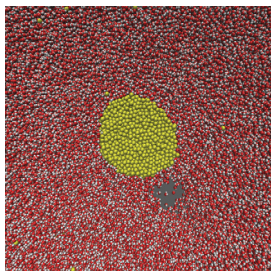

(a) $D = 6$ nm and nanoparticle heating temperature of 6500 K.

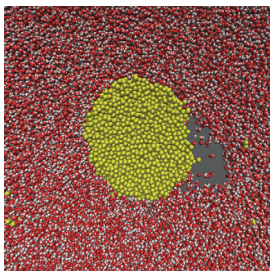

(b) $D = 7$ nm and nanoparticle heating temperature of 5500 K.

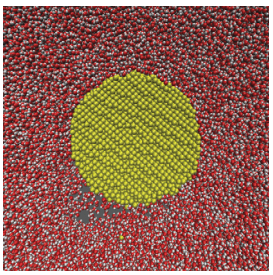

(c) $D = 8$ nm and nanoparticle heating temperature of 4250 K.

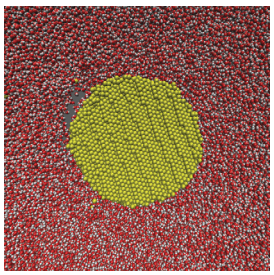

(d) $D = 9$ nm and nanoparticle heating temperature of 3700 K.

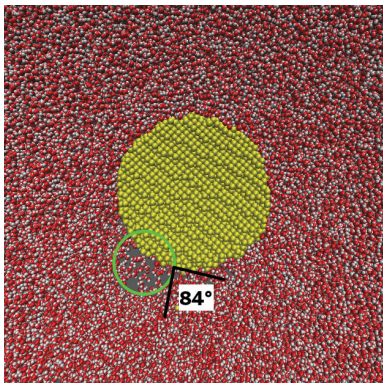

(e) Strongly wetting and nanoparticle heating temperature of 4250 K.

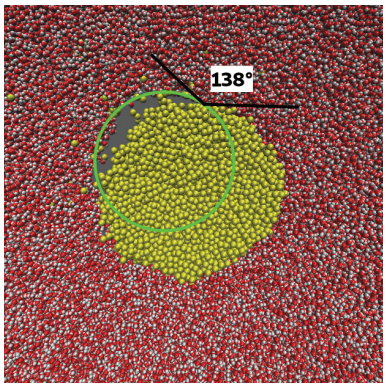

(f) Intermediate wetting and nanoparticle heating temperature of 4500 K.

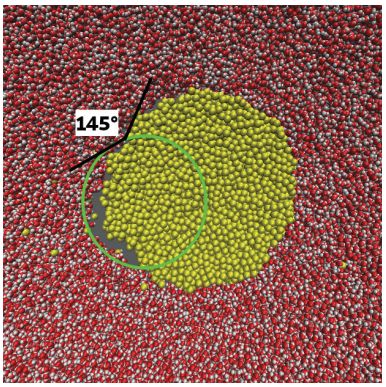

(g) Weakly wetting and nanoparticle heating temperature of 3400 K.

Figure 6.16: Figs. 6.16a, 6.16b, 6.16c, and 6.16d show the nanobubble in the early stage for different nanoparticle diameters with strongly wetting. Figs. 6.16e, 6.16f, and 6.16g show the heterogeneous nucleation in its early stage for the different wetting for the 8 nm diameter nanoparticle.

The others parameters that are influenced by the size and wetting of the nanoparticle are the contact angle and the radius of the nanobubble embryo. To compute these latter quantities, we exploit the same cross-section profile used to meassure the initial radius. As seen in Figs. 6.16e, 6.16f, and 6.16g, the stronger the wetting, the smaller the contact angle of the embryo. On the other hand, if we fix the nanoparticle wettability, the contact angle increases with increasing nanoparticle size, as seen in Tab. 6.1. It is also important to mention that the contact angles we measured at the nanoparticle-fluid interface are very different from those we measured for the planar surface (see Fig. 3.6).

In the other regime, where the nanoparticle is completely fragmented, a bubble appears in the region that was initially occupied by the nanoparticle, as seen in Fig. 6.17. In this latter case both events occur simultaneously, and we observe the following. When the nanoparticle is heated to very high temperatures, it undergoes a slight expansion and begins to fragmentate. While the nanoparticle begins its fragmentation process, it leaves holes in places that were originally occupied by its atoms. This gives rise to the bubble. As time elapses, these gaps expand, the fragments become smaller and separate one from each other. Finally, the bubble occupies the space that originally corresponded to the nanoparticle plus a space gained by expansion. In this case, the vapor in the bubble contains a considerable number of gold atoms.

6.2.4 Effect of geometry: nanorod and nanocube

To study the effect of geometry on cavitation, simulations are carried out with a nanorod and a nanocube. The nanorod and the nanocube have a volume similar to that of a spherical nanoparticle

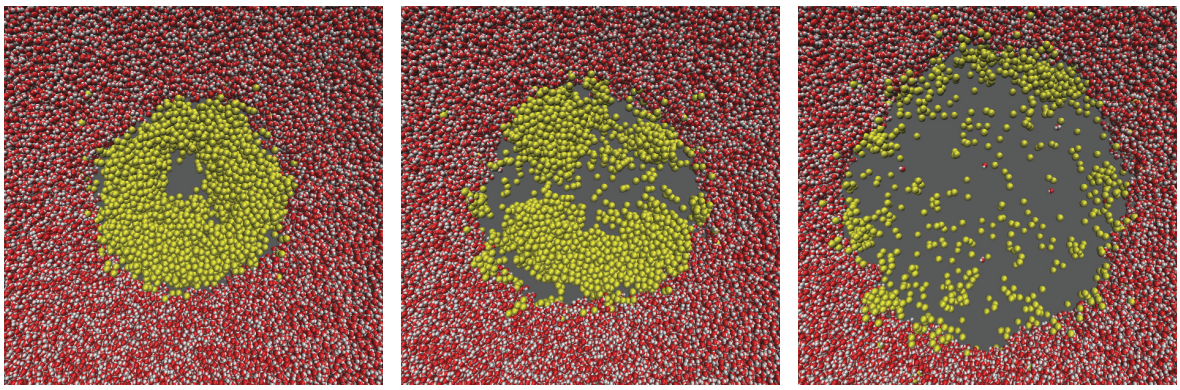

(a) (b) (c)

Figure 6.17: Figs. 6.17a, 6.17b and 6.17c show the generation of the bubble in the case of complete fragmentation of the nanoparticle. The case considered here is the weakly wetting nanoparticle having a diameter of 7 nm, and the nanoparticle heating temperature is 5000 K. The time delay between Figs. 6.17a and 6.17b, and Figs. 6.17b and 6.17c is 100 ps.

having a diameter of 8 nm. The dimensions of the nanorod are $r_{\mathrm{cyl}} = 3.0$ nm and $L_{\mathrm{cyl}} = 9.5$ nm, and for the nanocube its length is $L_{\mathrm{cub}} = 6.45$ nm.

In the case of the nanorod, we observe that cavitation does not occur in case of weak wetting. In this case, above a threshold in the nanoparticle heating temperature, the nanoparticle tends to lose its cylindrical structure and becomes sphere-like. This change of shape is explained energetically, because a spherical geometry is more favorable than a cylindrical or cubic one. On the other hand, when considering a strongly wetting nanorod, cavitation is observed. As seen for spherical nanoparticles, there is a nanoparticle heating temperature window, between T_{l1} and T_{l2}, for which cavitation with partial fragmentation occurs, as seen in Fig. 6.18.

For the nanocube, we observe a behavior similar to the case of the nanorod. In case of weak wetting, cavitation does not occur, and when exceeding a threshold of the nanoparticle heating temperature, the geometric structure is lost to become a sphere-like. The nanoparticle heating temperature window for this geometry is shown in Fig. 6.18. The limits of the nanoparticle heating temperature window for cavitation to occur with partial fragmentation, T_{l1} and T_{l2}, are different for each geometry. The lowest values for T_{l1} and T_{l2} are observed for the cubic geometry, hence, we have that the nanocube generates cavitation and loses its integrity at a lower nanoparticle heating temperature as compared to the others geometries. The spherical geometry is the one for which the nanoparticle heating temperature window is the largest. In addition, this geometry is the one that withstands the highest temperature T_{l2}.

As for the spherical geometry, nucleation around the nanorod and nanocube occurs non-uniformly. Fig. 6.19 shows snapshots of the cross section of the early stage of cavitation for the nanorod and the nanocube. Each geometry has "preferential" sites to initiate nucleation. Independent simulations with different seeds for the Nose-Hoover barostat are carried out in order to analyze the preferred sites to initiate nucleation for the different geometries. Different snapshots of the cross section of the early stage of cavitation for the nanorod are shown in Figs. 6.20a, 6.20b, and 6.20c, and for the nanocube in Figs. 6.20d, 6.20e, and 6.20f. Both nanoparticles are strongly wetting. For the nanorod, nucleation tends to start on one of the flat surfaces and not on the curved surface. For the nanocube, nucleation tends to start close to the vortices. We show in Tab. 6.2 the radius of the nanobubble in the early stage, the radius predicted by the CNT, and the contact angle of the embryo. We follow the same procedure as for the spherical geometry to obtain these values. As for the spherical case, the radius predicted by the CNT is an order of magnitude smaller than the radius computed in the simulations, and the contact angle is higher than the case of the planar surface.

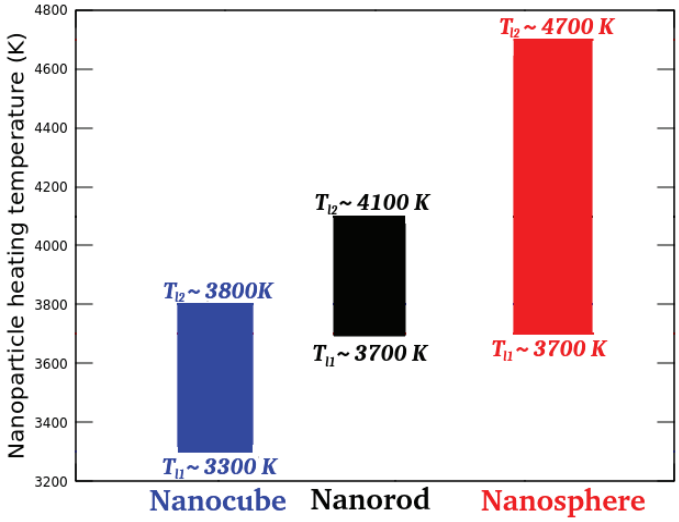

Figure 6.18: Nanoparticle heating temperature window corresponding to cavitation with partial fragmentation.

NP geometry	**bubble diameter** (nm) simulation	CNT	**contact angle** (degrees)
nanorod	1.14	0.09	65
nanocube	2.48	0.24	120

Table 6.2: Diameter of the nanobubble in the early stage of nucleation obtained from simulations compared with the prediction by the classical nucleation theory (CNT), for the strongly wetting nanorod and nanocube.

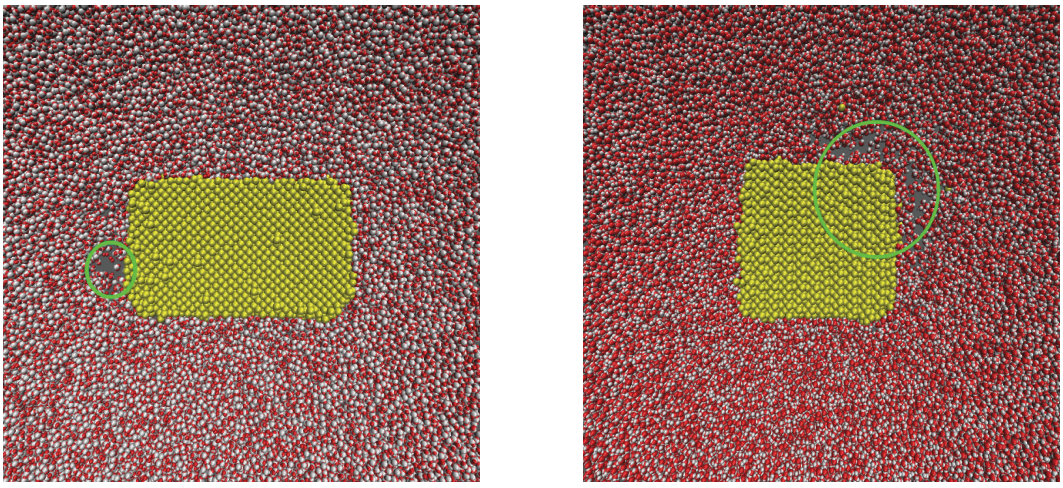

(a) Nanorod (b) Nanocube

Figure 6.19: Snapshots of the early stage of cavitation around the nanorod, Fig. 6.19a, and the nanocube, Fig. 6.19b. In both cases strongly wetting is considered.

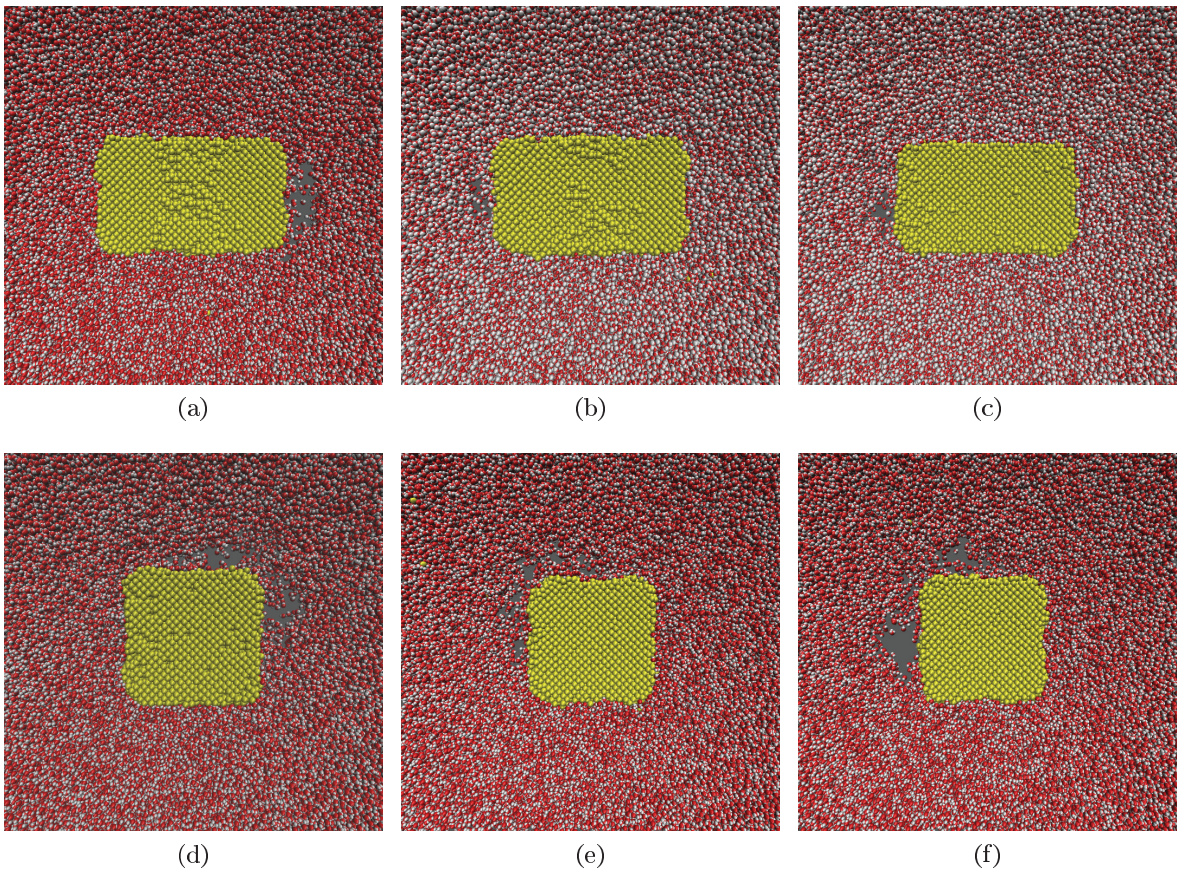

Figure 6.20: Figs. 6.20a, 6.20b, and 6.20c show the early stage of cavitation around a nanorod for different independent simulations. Figs. 6.20d, 6.20e, and 6.20f show the same for the nanocube.

6.2.5 Influence of the geometry on nucleation temperature

In order to investigate the influence of the nanoparticle geometry on the nucleation temperature, the temperature evolution of water in the vicinity of the nanoparticle is analyzed. For this purpose, we define a region surrounding the nanoparticle having a thickness of 1 nm, and we call the water molecules that occupy this region as "*neighboring water layer*". The geometry of this region depends on the geometry of the nanoparticle. In the spherical case, we consider water occupying the radial region $[R_{\mathrm{np}}, R_{\mathrm{np}}+1.0\ \mathrm{nm}]$ with R_{np} the radius of the nanoparticle. For the cylindrical case, we consider water molecules located in the region $[L_{\mathrm{cyl}}/2, L_{\mathrm{cyl}}/2+1.0\ \mathrm{nm}\ ]$ along z axis and in $x^2+y^2 \leq R_{\mathrm{cyl}}$, with L_{cyl} the length of the cylinder, and R_{cyl} its radius. Remember that the nanorod longitudinal axis is along z-axis. For the nanocube, we consider water molecules located in the region $[L_{\mathrm{cub}}/2, L_{\mathrm{cub}}/2+1.0$ nm] along x, y, and z dimensions.

Fig. 6.21 shows the minimum cavitation temperature of the neighboring water layer for the different geometries. We consider the case where the nanoparticle is being heated with the threshold temperature T_{ll} previously discussed. What is observed is that the nanocube has the lowest nucleation temperature, while the spherical geometry has the highest nucleation temperature. The latter indicates, together with the other results presented, that it is possible to control the nucleation of the liquid that surrounds the nanoparticles by modifying their geometric structure and/or wetting properties. For nanocube and nanorod with strong wetting, the minimal temperature for nucleation is lower than the spinodal temperature. Therefore, this also allows us to continue corroborating that nucleation around plasmonic nanoparticles that are heated with ultra-short pulsed lasers is not a phenomenon related with spinodal decomposition. The characteristics of the nucleation phenomenon studied here depend on various factors such as the type of wetting, the size, and the geometry of the nanoparticle.

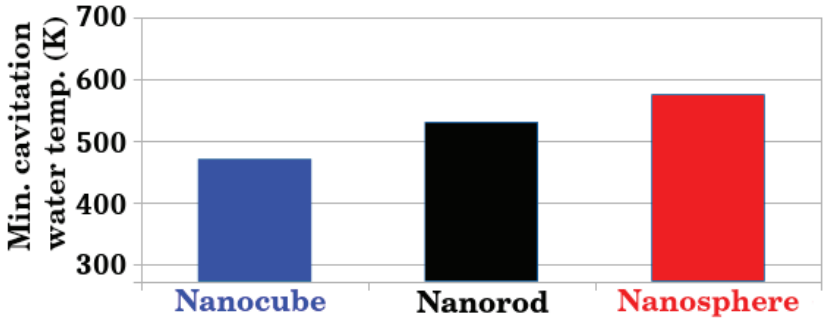

Figure 6.21: Minimum cavitation temperature of the neighboring water layer (see the text for its definition).

6.3 Comparison with previous works

Some previous works addressed the phenomenon of nanocavitation around nanoparticles heated by irradiation of laser light, and in this section we discuss some of these studies.

Experimentally, Hu et al. studied the transient absorption of gold nanoparticles in an aqueous solution, using a double pump-pulse configuration. They observed that explosive boiling of the surrounding liquid occurs when its temperature is larger than 550 ± 50 K [125]. Kotaidis et al., using gold nanoparticles ultra-rapidly excited, observed an out-of-equilibrium heating of the crystalline structure and, subsequently, that of the water layer surrounding the nanoparticle [126]. They found that explosive nanocavitation occurred above a threshold in laser fluence, generating transient nanobubbles with life times on the sub-nanosecond scale. They also mention that the formation of the nanobubble around the nanoparticle is homogeneous, which would be in contradiction with what is observed in Fig. 6.11. However, the window for data collection in their experiments is around 50 picoseconds, and what we observe is that at the beginning of nucleation, for times smaller than 100 ps, it is when nucleation inhomogeneity occurs, and then evolve in a homogeneous nucleation. Therefore, their timescale in data collection would not be small enough to be able to observe the initial inhomogeneities of nucleation. They also observe that the temperature of the liquid that surrounds the nanoparticle is around $0.9T_{cri}$ when nanocavitation occurs. In another work by Kotaidis et al., following a methodology similar to the previous one, they found that when the fluid surrounding the nanoparticle was in the gas phase, the heat flux dropped drastically [12] which would be related to the drop in the interfacial thermal conductance consistently with our results reported in Fig. 6.5a. They also found that the nanoparticle loses its crystalline structure, and the fluid temperature was $0.85T_{cri}$, when cavitation occurs, with T_{cri} the fluid critical temperature.

Hou et al. studied the formation of nanobubbles around a single nanoparticle and monitored them through optical scattering from a laser probe [51]. They observed that the formation of nanobubbles is explosive even when the nanoparticle is heated continuously. Boulais et al. employed a method that uses infrared femtosecond lasers that generated nanobubbles around gold nanoparticles [127]. They showed that the nanobubbles are due to the formation of a plasma around the nanoparticle rather than the heating of the nanoparticle. In their results they show that, initially, the nucleation of the nanobubble occurs at the poles of the nanoparticle that are parallel to the direction of the electric field of the incident radiation, and not on the entire surface of the nanoparticle. In the present work, the nanoparticle is heated up every 40 ps at temperatures above its melting point, and the temperature is allowed to relax between each heating. Our methodology aims to simulate the action of a ultra-short pulsed laser, and what it is seen is an explosive nanocavitation, as observed experimentally [12, 46, 48, 51, 125, 126].

Due to the experimental results of the gold nanoparticle - water system that show that explosive nanocavitation occurs at water temperatures close to the spinodal, it is possible to assume that

nanocavitation around plasmonic nanoparticles is an spinodal decomposition. In the present work, for the case of $\alpha = 1.0$ in $\epsilon_{NpO} = \alpha\epsilon_{\mathrm{AuO}}$ in the LJ potential, the temperature of the liquid surrounding the nanoparticle reaches a temperature around the spinodal temperature before explosive nanocavitation, which is consistent with the different experimental data. However, for the intermediate and weak wetting regimes, the temperature to reach nanocavitation is lower than the spinodal temperature of water. Therefore, this indicates that the temperature for nanocavitation is strongly dependent on the wetting properties of the interface. Nevertheless, to our knowledge, no experiments have been carried out with hydrophobic nanoparticles with which we can compare our results.

It is important to mention that the evolution of the nanobubble could depend on the way in which the nanoparticle is heated up. In another work using solid nanoparticles with two different wetting regimes immersed in a Lennard-Jones fluid, the nanoparticles are continuously heated but in a 'slower' way, until they reach melting temperature [32]. The authors of this work put a constant heating energy that is deposited in the nanoparticle continuously. They observe that for a superhydrophobic (super weak wetting) nanoparticle, the radius of the nanobubble grows continuously and slowly until it reaches a maximum value of 10 Å, but this does not occur in an explosive way. They also observe that for a superhydrophilic (super strong wetting) nanoparticle, first there is no nanobubble and after a certain time a bubble appears with a rapid growth and then has a slow growth until reaching a radius close to 20 Å. In this case, they never observe an explosive growth of the volume of the system. In the present work an explosive nanocavitation is observed regardless of wetting, the only thing that is different is the time to reach nanocavitation. It could be that the authors of the previously mentioned work are in the vapor layer growth regime discussed in section 6.1.2, and they never reach an explosive nanocavitation because energy is deposited in the nanoparticle in a very slow way. In contrast, in the present work, a large amount of energy bringing the nanoparticle to temperatures higher than melting temperatures is deposited frequently. Part of this energy is transferred to the fluid and allows it to reach a sufficiently high temperature to achieve an explosive nanocavitation. These differences in the ways the nanoparticle is heated up could establish methodologies to realize either a vapor layer or an explosive nanocavitation.

6.4 Summary

We can say the following about the phenomenon of nucleation and cavitation around metallic nanoparticles dispersed in an aqueous medium and that are heated by an ultra-short pulsed laser. The cavitation phenomenon strongly depends on the nanoparticle wetting properties. For example, the minimum fluid temperature for nucleation to occur depends on the wettability, being lower for the weaker wetting. For weak wetting, the minimum nucleation temperature of water can be 100 K smaller than its spinodal temperature. This result contrasts with the common belief that it is at the spinodal temperature that the fluid cavitates around plasmonic heated nanoparticles [115]. Another important result is that the process of nucleation is slow, compared to the typical time for heat diffusion in bulk water. The typical time of nucleation is on the order of nanoseconds, while heat diffuses nanometer distances in tens of picoseconds in bulk water. This kinetics is controlled by the interfacial thermal conductance G_{K} decreases with time, translated in long nucleation times. That is, the phenomenon of nucleation and subsequent cavitation is not a diffusion phenomenon, but it is controlled by the evolution with time of G_{K}. It is important to mention that the decrease in the value of G_{K} strongly depends on the type of wetting, and it is more pronounced for strong wetting nanoparticles.

But wetting not only influences the phenomenon of nucleation around plasmonic nanoparticles. If we consider the effects of size and geometry, we observe that the cavitation characteristics are also influenced. For example, we observe that there is a minimum size of the nanoparticle for nucleation to occur, and this size depends on wetting. The stronger the wetting, the smaller the minimal nanoparticle size. The energy deposited in the nanoparticle through abrupt heating can generate partial or total fragmentation of the nanoparticle. This allows us in identify three main behaviors that the nanoparticle-fluid system will display as a function of the energy deposited: i) no cavitation and no

fragmentation, ii) cavitation with partial fragmentation, and iii) cavitation with total fragmentation. Also, we observe that the minimum temperature of the surrounding fluid when cavitation occurs depends on the geometry of the nanoparticle at a fixed value of nanoparticle volume and contact angle. Regarding the nanocube and nanorod, we show that such geometries have preferential sites where nucleation begins.

When comparing the values predicted by classical nucleation theory with the results of our simulations, we obtain that the CNT predicts radii that are generally an order of magnitude smaller than what we measure. Finally, the contact angles of the embryo that we measure during nucleation for the different nanoparticles considered here differ significantly from those that we measure for a drop of water on a flat surface. This study calls for simulations of reallistic nanoparticles coated by surfactants, which allow one to time the nanoparticle-water contact angle.

Chapter 7

Conclusion

Initially we set out to test thermodynamics at its lower limit, that is, considering a few tens of water molecules confined in a nanometric volume. In turn, we propose a methodology to perform simulations of Molecular Dynamics under isobaric conditions using a mobile cover like a piston. In order to assess thermodynamics at the nanoscale and the methodology proposed, we measure different thermodynamic properties of a system composed of 126 water molecules. In general, the values obtained for the thermodynamic response coefficients are in the expected order of magnitude and close to the experimental value. To calculate the response parameters we mainly use concepts from thermodynamics, hence we conclude that the thermodynamic is still valid even for systems of a few tens of molecules in a volume of a few nm^3. However, we show that the average over time and the ensemble average for the considered system differ. We associate this discrepancy to the fact that we are working with a system with very few molecules during a few ps simulations, and this affects the precision described by the partition function.

The small water system reaches a value of its density that agrees quantitatively with the experimental value. Considering the above, in addition to the fact that the thermophysical parameters we measured agree with the experimental ones, we conclude that our methodology to impose a constant pressure on a confined fluid is effective. Even though, some details need to be improved. Here, we use a very dense cover in order to avoid porosity in it. This dense cover can generate important computational costs by increasing the dimensions of the system if we consider that the cover is simulated with atomistic-like detail. It is necessary to improve the interaction between cover atom - fluid molecule in order to reduce the computational cost, but without disturbing the structure of the fluid near the cover. The idea of this proposal is to devise methodologies for MD that simulate the phenomena with greater relation to physical reality, which, although computationally they can be more demanding, avoids adding noise to the Lagrangian of the system. Furthermore, the continuous technological advance in supercomputers is leaving the computational spends in a second plane and allow the development of better methodologies for computational simulations independent of its computational cost.

However, we cannot deny the fact that the different existing methods are very useful for simulating systems in NVT, NPT, among others ensembles. The main idea of many of these methods is to impose the thermodynamic conditions of the ensemble by means of extra degrees of freedom. These extra degrees of freedom in the Lagrangian simulate the thermal bath with a very low computational cost, therefore, they are efficient when we work with a considerable number of atoms. Since this type of algorithms are widely used in different software to carry out Molecular Dynamics simulations, we make use of them in order to study thermal transport for systems with hundreds of thousands of atoms. These molecular systems consist of metallic nanoparticles that are immersed in a pool of water.

We have investigated the dependence of the interfacial thermal conductance of gold-like nanoparticles with the nanoparticle size and with tunable wettability in water. We observe that the thermal conductance increases by decreasing the nanoparticle radius, whatever the wetting properties of the interface are. Size-effects of the thermal transport were rationalized from the perspective of an acoustic

model. It was concluded that the thermal conductance increases when the nanoparticle size decreases, following the relation $G_{\mathrm{K}}(R_{\mathrm{np}}) = G_{\mathrm{K}}(\infty)(1 + \delta/R_{\mathrm{np}})^2$. Such an expression describes not only the molecular dynamics data presented here, but other data of the literature as well [36, 38]. The size dependence of the thermal conductance may also be well described by the empirical relation proposed in [36], $G_{\mathrm{K}}(R_{np}) = G_{\mathrm{K}}(\infty)(1 + \delta/R_{np})$.

The increase of the conductance with the nanoparticle curvature may be due to two important factors. First, when the nanoparticle size is reduced, the number of water molecules interacting with a surface gold atom increases, as quantified by the water-gold potential energy. Second, when the nanoparticle size is reduced, the gold vibrational spectrum is strongly modified. In particular, the spectrum of large nanoparticles displays two van Hove peaks corresponding to the density of states of the bulk gold. The high frequency peak vanishes by reducing the nanoparticle radius, while the low frequency peak is enhanced. This enhancement facilitates energy transfer between small gold nanoparticles and the liquid water, as a result of the good matching between gold and oxygen spectra.

We also have assessed the extent to which continuum heat equations describes the cooling kinetics of small nanoparticles initially heated up at high temperatures. Continuum medium models are found to describe well the heat transfer of a broad range of nanoparticle sizes with diameters down to 1 nm, and heated up by hundredths of Kelvins.

Our model to understand size-dependent effects on the thermal conductance, may be extended to describe systems well beyond plasmonic nanoparticles in water. The size effects evidenced here should be important for nanocomposites and also nanocrystals. Also, beyond the linear regime studied here, the fragmentation process of small nanoparticles, and in particular the influence of wetting, may be systematically explored.

In turn, we use Molecular Dynamics simulations to model experiments in which plasmonic nanoparticles are heated up by ultra-short intense pulsed lasers and the surrounding liquid cavitates. Our methodology consists of heating the nanoparticles at high temperatures every 40 ps, simulating thus the effect of a pulsed laser. We consider three different nanoparticle wettability between the nanoparticle and the fluid: strong wetting, intermediate wetting, and weak wetting. Our results show that the process of nanocavitation is strongly influenced by the nanoparticle wettability.

The time to initiate nanocavitation depends also on wetting, this being smaller for strong wetting and longer for weak wetting. For each wetting, the nanocavitation time is generally shown to be a constant value or a characteristic time that depends on the wetting, and is on the scale of nanoseconds. From this, we have that the nanocavitation is a slow process compared to the heat diffusion in bulk water that is on the picosecond time scale. Before cavitation, the value of the interfacial thermal conductance decreases sharply with time, its decrease being more drastic for strong wetting. Nanocavitation phenomenon seems to be controlled by the decrease in the interfacial thermal conductance. When the fluid surrounding the nanoparticle is in vapor phase, the interfacial thermal conductance converges to a value independent on wetting.

One important point is that the water temperature to reach nanocavitation T_{cav} is different for each wetting, being lower for weak wetting and higher for strong wetting. Also, for each wetting T_{cav} is between the normal boiling temperature and the spinodal temperature, contrary to the common belief that cavitation occurs at the spinodal temperature. In fact, for weak wetting the nanocavitation temperature can be 100 K lower than the spinodal temperature. This helps us to deduce that the phenomenon of nucleation around plasmonic nanoparticles is not a spinodal decomposition.

At the beginning of nucleation, the nanobubble is not generated homogeneously over the entire surface of the nanoparticle. Rather, first, nucleation begins from a localized region of the nanoparticle surface that begins the phase transition from liquid to vapor. This embryo promotes the nucleation of all the

liquid that surrounds the nanoparticle and that takes it to the vapor phase, and allows nucleation to be homogeneous for later times.

We tested different continuum medium models in order to analyze their ability to describe the temperature profile before cavitation of the liquid surrounding the nanoparticle. We observe that continuum models that take into account a constant interfacial conductance can not describe what it is observed in our simulations. But when the variation of the conductance is taken into account, continuum medium models can describe the temperature profile of the water surrounding the nanoparticle for strong and intermediate wetting. For weak wetting, it appears that heat transport at the interface is more complex and continuum models considered here cannot describe it.

Taking into account the size, wetting, and geometry of the nanoparticle in the phenomenon of nanocavitation around plasmonic nanoparticles heated by an ultra-short pulsed laser, we have the following. As previously described, nucleation occurs in a non-uniform way on the surface of the nanoparticle regardless of its geometry. The location to begin nucleation is shown to have "privileged" places for the nanorod and the nanocube. For nucleation to occur, there is a minimum in the size of the nanoparticle that depends on the nanoparticle wettability. For strongly wetting, nucleation is achieved with smaller nanoparticles than for intermediate or weak wetting. Moreover, this minimum nanoparticle size to observe nucleation depends not only on the type of wetting, but also on the nature of the fluid. Similarly, if we consider a fixed wetting, the minimum temperature that the liquid surrounding the nanoparticle must reach depends on the nanopartice size and geometry. This minimum temperature increases with increasing nanoparticle size and reaches a value of ~ 735 K for a planar surface with strong wetting.

We observed different scenarios, as a function of the supplied energy and the dimensions of the nanoparticle: i) no cavitation and no fragmentation of the nanoparticle, ii) cavitation with partial fragmentation of the nanoparticle, and iii) cavitation and total fragmentation of the nanoparticle. The nanoparticle heating temperature window in which cavitation occurs with partial fragmentation depends on its geometry and wetting. For strong wetting, the cubic geometry corresponds to the lowest heating temperature to have cavitation, while the spherical geometry is the one that supports the highest heating temperatures without total fragmentation of the nanoparticle. For the nanocube and nanorod with weak wetting, no cavitation was observed. In these cases, when exceeding a heating threshold temperature, the nanoparticle integrity is lost, and tend to be a sphere-like nanoparticle.

Finally, this work seeks to close gaps in the understanding and study of the behavior of matter at the nanoscale. The continuous advances in the last decades in the study of nanosciences have strongly promoted nanotechnological progress, which demands a greater detail in the study of the matter on the small scale. At the same time, from the didactic point of view, it is important to understand why matter can present different properties at the nanoscale than the properties in the bulk. The work presented in this thesis allows deepening the study and understanding of the behavior of matter at the nanoscale in order to optimize the functioning of practical applications.

Publications and seminars

Publications

We have already presented the main work that was carried out during my doctoral studies. All of this work has been presented in parts in different articles that have already been published, are currently under review, or are still in the writing process. The list of these works are the following.

Published

- O. Gutiérrez-Varela, S. Merabia, and R. Santamaria; Size-dependent effects of the thermal transport at gold nanoparticle-water interfaces; *The Journal of Chemical Physics* **157**; 084702; 2022.
- O. Gutiérrez-Varela, J. Lombard, T. Biben, R. Santamaria, and S. Merabia; Wetting controlled boiling at the nanoscale; Preprint: 10.48550/arXiv.2209.07900. Submitted for review in January 2023.

In preparation

- O. Gutiérrez-Varela, S. Merabia, R. Santamaria, et al.; Effect of size and geometry on nucleation at the nanoscale; Preparing the manuscript to present the results. Expected to be sent in 2023.
- O. Gutiérrez-Varela, S. Merabia, R. Santamaria, et al.; Anharmonic effects on thermal transfer; Preparing the manuscript to present the results. Expected to be sent in 2023.
- O. Gutiérrez-Varela, R. Santamaria, S. Merabia, et al.; Atomistic simulations with isobaric conditions: a proposal for a barostat; Preparing the manuscript to present the results. Expected to be sent in 2023.

Seminars

The work presented in this doctoral thesis was presented in the following seminars and congresses.

- Congress of students of the Postgraduate in Physical Sciences - UNAM, 2019 and 2022 editions.
- Present your doctoral thesis in 3 minutes, Institut Lumière Matière (ILM - UCBL) PhD day, 2021.
- Seminar of the group of Modeling of Condensed Matter and Interfaces - ILM, UCBL, 2021.
- XXX International Materials Research Congress, 2022.

Currently and future work

We are currently working on issues related to those exposed in this thesis. Regarding the confined system for isobaric simulations, we continue to work on an interaction potential between the cover atoms - fluid molecules that has a lower computational cost. Also, we want to work on a system of mixtures of methane in water using pressures of hundreds of atmospheres and higher temperatures in order to study chemical reactions. Furthermore, we are testing the method in a larger system in which only classical interactions between all atoms are considered.

Regarding thermal transport around plasmonic nanoparticles, we are currently working with a system more in line with what is carried out experimentally. In the laboratory, work is done with nanoparticles functionalized with surfactants on their surface in order to make the suspension more stable. In turn, the specific surfactant with which the nanoparticle is functionalized is the one that gives the wetting properties of the nanoparticle-fluid interface. To this end, we have functionalized nanoparticles with hydrophobic and hydrophilic surfactants on their surface. With these systems we seek to study heat transport in realistic and more complex systems, since in this case we have two interfaces: nanoparticle - surfactant and surfactant - fluid. Preliminarily, we have already observed that the fluid near the functionalized nanoparticle can be heated to temperatures higher than boiling temperature without generating a phase transition. We seek to study this property and its potential application in photothermal therapies.

On the other hand, we are studying the dynamics of Janus nanoparticles when they are heated with a laser using Molecular Dynamics simulations. To this end, we use molecular systems that consist of a Janus-like nanoparticle immersed in an aqueous medium. Preliminarily, we have observed that the nanoparticle diffusion regime is different depending on the type of heating. If the heating is sufficient high to generate a phase transition from the surrounding liquid to the nanoparticle, the translation of the latter undergoes a drastic change since the vaporized fluid offers less resistance to the motion of the nanoparticle. Furthermore, if we study the situation where the nanoparticle is confined in the middle of the walls, its diffusion is very different from the situation where there is no confinement. What we have observed is that the confinement reduces the mobility of the nanoparticle.

These projects are the ones we are currently working on and which show promising results in the near future.

Bibliography

[1] L. Bocquet and E. Charlaix; Nanofluidics, from bulk to interfaces; Chemical Society Reviews **260**; pp. 1073-1095; 2009.

[2] S. Napolitano and M. Wübbenhorst; The lifetime of the deviations from bulk behaviour in polymers confined at the nanoscale; Nature Communications **2**; 260; 2011.

[3] K. Adrjanowicz, R. Winkler, A. Dzienia, M. Paluch, and S. Napolitano; Connecting 1D and 2D Confined Polymer Dynamics to Its Bulk Behavior via Density Scaling; ACS Macro Letters **8**; pp. 304-309; 2019.

[4] M. B. Cortie; The weird world of nanoscale gold; Gold Bulletin **37**; pp. 12-19; 2004.

[5] E. Hernández-Huerta, R. Santamaria, and T. Rocha-Rinza; Thermodynamics from Lagrangian theory and its applications to nanosize particle systems; Molecular Physics **119**; e1940333; 2021.

[6] H. J. C. Berendsen, J. P. M. Postma, W. F. van Gunsteren, A. DiNola, and J. R. Haak; Molecular dynamics with coupling to an external bath; The Journal of Chemical Physics **81**; 3684; 1984.

[7] H. C. Andersen; Molecular dynamics simulations at constant pressure and/or temperature; The Journal of Chemical Physics **72**; 2384; 1980.

[8] S. Eustis and M. A. El-Sayed; Why gold nanoparticles are more precious than pretty gold: Noble metal surface plasmon resonance and its enhancement of the radiative and nonradiative properties of nanocrystals of different shapes; Chemical Society Reviews **35**; pp. 209–217; 2006.

[9] G. Baffou and R. Quidant; Thermo-plasmonics: using metallic nanostructures asnano-sources of heat; Laser & Photonics Reviews **7**; pp. 171–187; 2012.

[10] Z. Qin and J. C. Bischof; Thermophysical and biological responses of gold nanoparticle laser heating; Chemichal Society Review **41**; pp. 1191–1217; 2012.

[11] A. Plech and V. Kotaidis; Laser-induced heating and melting of gold nanoparticles studied by time-resolved x-ray scattering; Physical Review B **70**; 195423; 2004.

[12] V. Kotaidis, C. Dahmen, G. von Plessen, F. Springer, and A. Plech, Excitation of nanoscale vapor bubbles at the surface of gold nanoparticles in water; Journal of Chemical Physics **124**; 184702; 2006.

[13] J. Veilleux and S. Coulombe; A dispersion model of enhanced mass diffusion in nanofluids; Chemical Engineering Science **66**; pp. 2377–2384; 2011.

[14] S. Komati and A. K. Suresh; Anomalous Enhancement of Interphase Transport Rates by Nanoparticles: Effect of Magnetic Iron Oxide on Gas-Liquid Mass Transfer; Industrial & Engineering Chemistry Research **49**; pp. 390–405; 2010.

[15] W. Zhao and J. M. Karp; Nanoantennas heat up; Nature Materials **8** (6); pp. 453–454; 2009.

[16] N. Ali, J. A. Teixeira, and A. Addali; A Review on Nanofluids: Fabrication, Stability, and Thermophysical Properties; Journal of Nanomaterials; pp. 1–33; 2018.

[17] D. P. Kulkarni, D. K. Das, and R. S. Vajjha; Application of nanofluids in heating buildings and reducing pollution; Applied Energy **86** (12); pp. 2566–2573; 2009.

[18] S. Wippermann, M. Vörös, D. Rocca, A. Gali, G. Zimanyi, and G. Galli; High-Pressure Core Structures of Si Nanoparticles for Solar Energy Conversion; Physical Review Letters **110** (4); 046804; 2013.

[19] R. Taylor, S. Coulombe, T. Otanicar, P. Phelan, A. Gunawan et al.; Small particles, big impacts: A review of the diverse applications of nanofluids; Applied Physics Reviews **113** (1); 011301; 2013.

[20] J. N. Solanki and Z. V. P. Murthy; Preparation of Silver Nanofluids with High Electrical Conductivity; Journal of Dispersion Science and Technology **32**; pp. 724–730; 2011.

[21] H. S. Kim and D. Y. Lee; Near-Infrared-Responsive Cancer Photothermal and Photodynamic Therapy Using Gold Nanoparticles; Polymers **10**; 961; 2018.

[22] Z. Ge, D. G. Cahill, and P. V. Braun; AuPd Metal Nanoparticles as Probes of Nanoscale Thermal Transport in Aqueous Solution; The Journal of Physical Chemistry B **108**; pp. 18870–18875; 2004.

[23] X. Wu, Y. Ni, J. Zhu, N. D. Burrows, C. J. Murphy, T. Dumitrica and X. Wang; Thermal transport across surfactant layers on gold nanorods in aqueous solution; ACS Applied Material Interfaces **8**; pp. 10581–10589; 2016.

[24] A. J. Schmidt, J. D. Alper, M. Chiesa, G. Chen, S. K. Das, and K. Hamad-Schifferli; Absorption and thermal decay; Journal of Physical Chemistry C **112**; pp. 13320–13323; 2008.

[25] J. Park and D. G. Cahill; Plasmonic sensing of heat transport at solid-liquid interfaces; Journal of Physical Chemistry C; **120**; pp. 2814–2821; 2016.

[26] B. Ramos-Alvarado, S. Kumar, and G. P. Peterson; Solid-Liquid Thermal Transport and Its Relationship with Wettability and the Interfacial Liquid Structure; The Journal of Physical Chemistry Letters **7**; pp. 3497–3501; 2016.

[27] T. Stoll, P. Maioli, A. Crut, S. Rodal-Cedeira, I. Pastoriza-Santos, F. Vallée and N. Del Fatti; Time-resolved investigations of the cooling dynamics of metal nanoparticles: impact of environment; Journal of Physical Chemistry C **119**; pp. 12757–12764; 2015.

[28] P. L. Kapitza; Heat Transfer and Superfluidity of Helium II; Physical Review **60**; pp. 354–355; 1941.

[29] S. Merabia, S. Shenogin; L. Joly, P. Keblinski, and J.-L. Barrat; Heat transfer from nanoparticles: A corresponding state analysis; Proceedings of the National Academy of Sciences **106** (36); pp. 15113–15118; 2009.

[30] X. Chen, A. Munjiza, K. Zhang, and D. Wen; Molecular Dynamics Simulation of Heat Transfer from a Gold Nanoparticle to a Water Pool; The Journal of Physical Chemistry C **118**; pp. 1285–1293; 2014.

[31] A. Rajabpour, R. Seif, S. Arabha, M. M. Heyhat, S. Merabia, and A. Hassanali; Thermal transport at a nanoparticle-water interface: A molecular dynamics and continuum modeling study; The Journal of Chemical Physics **150**; 114701; 2019.

[32] J.-H. Pu, J. Sun, W. Wang and H. S. Wang; Generation and evolution of nanobubbles on heat nanoparticles: a molecular dynamics study; Langmuir **36**; pp. 2375–2382; 2020.

[33] C. Z. Zhao, W. An, Y. Zhang, Q. Dong and N. Gao; A molecular dynamics analysis on interfacial thermal resistance between particle and medium in light-induced heat transfer of plasmonic nanofluid; Langmuir **38**; pp. 2327–2334; 2022.

[34] A. R. Nair and S. P. Sathian; Heat transfer across nanoparticle liquid interfaces; Journal of Heat Transfer **139**; 112402; 2016.

[35] S. M. Neidhart and J. D. Gezelter; Thermal Transport is Influenced by Nanoparticle Morphology: A Molecular Dynamics Study; The Journal of Physical Chemistry C **122**; pp. 1430–1436; 2018.

[36] A. S. Tascini, J. Armstrong, E. Chiavazzo, M. Fasano, P. Asinari, and F. Bresme; Thermal transport across nanoparticle-fluid interfaces: the interplay of interfacial curvature and nanoparticle-fluid interactions; Physical Chemistry Chemical Physics **19** (4); pp. 3244–3253; 2017.

[37] M. Roodbari, M. Abbasi, S. Arabha, A. Gharedaghi, and A. Rajabpour; Interfacial thermal conductance between TiO2 nanoparticle and water: a molecular dynamics study; Journal of Molecular Liquids **348**; 118053; 2022.

[38] W.-L. Ong, S. Majumdar, J. A. Malen and A. J. H Mc Gaughey; Coupling of organic and inorganic vibrational states and their thermal transport in nanocrystals arrays; Journal of Physical Chemistry C **118**; pp. 7288–7295; 2014.

[39] A. Lervik, F. Bresme and S. Kjelstrup; Heat transfer in soft nanoscale interfaces: the influence of interface curvature; Soft Matter **5**; pp. 2407–2414; 2009.

[40] O. Wilhelmsen, T. T. Trinh, S. Kjestrup, S. T. van Erp and D. Bedeaux; Heat and Mass transfer across interfaces in complex nanogeometries; Physical Review Letters **114**; 065901; 2015.

[41] A. M. Karim, N. Al Hasan, S. Ivanov, S. Siefert, R. T. Kelly, et al.; Synthesis of 1 nm Pd Nanoparticles in a Microfluidic Reactor: Insights from in Situ X-ray Absorption Fine Structure Spectroscopy and Small-Angle X-ray Scattering; The Journal of Physical Chemistry C **119**; pp. 13257–1326; 2015.

[42] H. Ding and Z. Chen; Nanotheranostic Application of Fluorescent Protein-Gold Nanocluster Hybrid Materials: A Mini-review; Nanotheranostics **5**; pp. 461–471; 2021.

[43] J. E. Sheperd and B. Strutevand; Rapid evaporation at the superheat limit; Journal of Fluid Mechanics **121**; 1982.

[44] J.S. Sperry, N.Z. Saliendra, W.T. Pockman, H. Cochard, P. Cuizat, S.D. Davis, F.W. Ewers, M.T. Tyree; New evidence for large negative xylem pressures and their measurement by the pressure chamber technique; Plant Cell Environment **19**; pp. 427–436; 1996.

[45] L. Cavigli et al.; Light activated microbubbles for imaging and microsurgery; Proc. SPIE 10064, Photons Plus Ultrasound: Imaging and Sensing 2017, 1006457.

[46] T. Katayama, K. Setoura, D. Werner, H. Miyasaka, and S. Hashimoto; Picosecond-to-Nanosecond Dynamics of Plasmonic Nanobubbles from Pump-Probe Spectral Measurements of Aqueous Colloidal Gold Nanoparticles; Langmuir **30**; pp. 9504–9513; 2014.

[47] A. Vogel and V. Venugopalan; Mechanisms of pulsed laser ablation of biological tissues; Chemical Review **103**; 577; 2003.

[48] T. Jollans and M. Orrit; Explosive, oscillatory and Leidenfrost boiling at the nanoscale; Physical Review E **99**; 063110; 2019.

[49] Y. Wang, M. E. Zaytsev, G. Lajoinie, H. L. The, J. C. T. Eijkel, et al.; Giant and explosive plasmonic bubbles by delayed nucleation; Proceedings of the National Academy of Sciences **115**; pp. 7676–7681; 2018.

[50] D. Stavich, B. Nestoiter, D. Gonzalez, A. Freund, X. Buelna, K. Wang, J. A. Teprovich Jr., and J. Eloranta; Time-Resolved Shadowgraph Photography of Laser-Heated Plasmonic Gold Nanoparticles in Water; The Journal of Physical Chemistry C **124**; pp. 14022–14029; 2020.

[51] L. Hou, M. Yorulmaz, N. R. Verhart, and M. Orrit; Explosive formation and dynamics of vapor nanobubbles around a continuously heated gold nanosphere; New Journal of Physics **17**; 013050; 2015.

[52] E. Lukianova-Hleb, Y. Hu, L. Latterini, L. Tarpani, S. Lee, R. A. Drezek, J. H. Hafner, and D. O. Lapotko; Plasmonic Nanobubbles as Transient Vapor Nanobubbles Generated around Plasmonic Nanoparticles; ACS Nano **4**; pp. 2109–2123; 2010.

[53] K. Sasikumar, Z. Liang, D. G. Cahill, and P. Keblinski; Curvature induced phase stability of an intensely heated liquid; Journal of Chemical Physics **140**; 234506; 2014.

[54] J. Shao, M. Xuan, L. Dai, T. Si, J. Li, and Q. He; Near-Infrared-Activated Nanocalorifiers in Microcapsules: Vapor Bubble Generation for In Vivo Enhanced Cancer Therapy; Angewandte Chemie International Edition **54**; pp. 12782–12787; 2015.

[55] C. M. Pitsillides, E. K. Joe, X. Wei, R. R. Anderson, and C. P. Lin; Selective cell targeting with light-absorbing microparticles and nanoparticles; Biophysical Journal **84**; pp. 4023–4032; 2003.

[56] M. Kitz, S. Preisser, A. Wetterwald, M. Jaeger, G.N. Thalmann and M. Frenz; Vapor bubble generation around gold nanoparticles and its application to damaging of cells; Biomedical Optics Express **2**; 291; 2011.

[57] C. Zhao, Y. Xie, Z. Mao, Y. Zhao, J. Rufo, S. Yang, T. J. Huang, et al.; Theory and experiment on particle trapping and manipulation via optothermally generated bubbles; Lab on a Chip **14**; pp. 384–391; 2014.

[58] D. Lapotko; Plasmonic nanoparticle-generated photothermal bubbles and their biomedical applications; Nanomedicine **4**; pp. 813–845; 2009.

[59] V. P. Zharov; Ultrasharp nonlinear photothermal and photoacoustic resonances and holes beyond the spectral limit; Nature Photonics **5**; pp. 110–116; 2011.

[60] E. Faraggi, B.S. Gerstman, and J. Sun; Biophysical effects of pulsed lasers in the retina and other tissues containing strongly absorbing particles: shockwave and explosive bubble generation; Journal of Biomedical Optics **10**; 064029; 2005.

[61] D. Wen; Intracellular hyperthermia: nanobubbles and their biomedical applications; International Journal of Hyperthermia **25**; 533; 2009.

[62] J. Lombard, J. Lam, F. Detcheverry, T. Biben and S. Merabia; Strong and fast rising pressure waves emitted by plasmonic vapor nanobubbles; Physical Review Research **3**; 023231; 2021.

[63] Y. Wang, M.E. Zaytsev, H.L. The, J.C.T. Eijkel, H.J.W. Zandvliet, X. Zhang and D. Lohse; Vapor and gas-bubble growth dynamics around laser-irradiated water immersed plasmonic nanoparticles; ACS Nano **11**; 2045; 2017.

[64] S. Merabia, S. Shenogin, L. Joly, P. Keblanski, and J.-L. Barrat; Heat transfer from nanoparticles: A corresponding state analysis; PNAS **106**; pp. 15113–15118; 2009;

[65] S. Merabia, P. Keblenski, L. Joly, L. J. Lewis, and J.-L. Barrat; Critical heat flux around strongly heated nanoparticles; Physical Review E **79**; 021404; 2009.

[66] K. Sasikumar, Z. Liang, D. G. Cahill, and P. Keblinski; Curvature induced phase stability of an intensely heated liquid; The Journal of Chemical Physics **140**; 234506; 2014.

[67] X. Chen, A. Munjiza, K. Zhang, and D. Wen; Molecular Dynamics Simulation of Heat Transfer from a Gold Nanoparticle to a Water Pool; The Journal of Physical Chemistry **C 118**; pp. 1285–1293; 2014.

[68] S. Maheshwari, M. van der Hoef; A. Prosperetti and D. Lohse, Dynamics of formation of a vapor nanobubble around a heated nanoparticle; Journal of Physical Chemistry C **122**; 20571; 2018.

[69] J. Lombard, T. Biben, and S. Merabia; Kinetics of Nanobubble Generation Around Overheated Nanoparticles; Physical Review Letters **112**; 105701; 2014.

[70] J. Lombard, T. Biben, and S. Merabia; Threshold for Vapor Nanobubble Generation Around Plasmonic Nanoparticles; The Journal of Physical Chemistry C **121**; pp. 15402–15415; 2017.

[71] R. Thiery, S. Loock, and L. Mercury; Explosive properties of superheated aqueous solutions in volcanic and hydrothermal systems; Metastable Systems under Pressure; Springer; pp. 293–310; 2010.

[72] A. P. Thompson, H. M. Aktulga, R. Berger, et al.; LAMMPS - a flexible simulation tool for particle-based materials modeling at the atomic, meso, and continuum scales; Comp Phys Comm **271**; 10817; 2022.

[73] W. C. Swope, H. C. Andersen, P. H. Berens, and K. R. Wilson; A computer simulation method for the calculation of equilibrium constants for the formation of physical clusters of molecules: Application to small water clusters; The Journal of Chemical Physics. **76** (1); p. 648 (Appendix); 1982.

[74] S. Chandrasekhar; Stochastic problems in physics and astronomy; Reviews of Modern Physics **15**; pp. 1–89; 1943.

[75] R. Santanaria, A. Alvarez de la Paz, L. Roskop, and L. Adamowicz; Statistical Contact Model for Confined Molecules; Journal of Statistical Physics **164**; pp. 1000–1025; 2016.

[76] J. L. F. Abascal and C. Vega; A general purpose model for the condensed phases of water: TIP4P/2005; The Journal of Chemical Physics **123**; 234505; 2005.

[77] H. Heinz, R. A. Vaia, B. L. Farmer, and R. R. Naik; Accurate Simulation of Surfaces and Interfaces of Face-Centered Cubic Metals Using 12-6 and 9-6 Lennard-Jones Potentials; The Journal of Physical Chemistry C **112** (44); pp. 17281–17290; 2008.

[78] R. Santamaria and J. Soullard; Revisiting particle dynamics in the NPT ensemble under the extended Lagrangian approach; Molecular Simulation **49** (9); pp. 855–866; 2023.

[79] M. E. Tuckerman, J. Alejandre, R. López-Rendón, A. L. Jochim, and G. J. Martyna; A Liouville-operator derived measure-preserving integrator for molecular dynamics simulations in the isothermal-isobaric ensemble; Journal of Physics A: Mathematical and General **39**; pp. 5629-5651; 2006.

[80] The Leapfrog Integrator; Drexel.edu. Retrieved on January 31, 2023, from http://www.physics.drexel.edu/∼steve/Courses/Comp_Phys/Integrators/leapfrog/

[81] Ensembles; Cam.ac.uk. Retrieved on January 31, 2023, from https://www.tcm.phy.cam.ac.uk/castep/MD/node4.html

[82] Zhao, Y.; Brief introduction to the thermostats. Retrieved on January 31, 2023, from https://home.gwu.edu/∼yxzhao/ResearchNotes/ResearchNote007Thermostat.pdf

[83] The Hoover Barostat; Uark.edu.; Retrieved on January 31, 2023, from https://wanglab.hosted.uark.edu/DLPOLY2/node78.html

[84] S. Nosé; A unified formulation of the constant temperature molecular-dynamics methods; Journal of Chemical Physics. **81**; pp. 511–519; 1984.

[85] W. G. Hoover; Canonical dynamics: Equilibrium phase-space distributions; Phyical Review A **31**; pp. 1695–1697; 1985.

[86] W. G. Hoover; Constant-pressure equations of motion; Physical Review A **34**; pp. 2499–2500; 1986.

[87] Universidad de Granada, España; Densidad del agua líquida entre 0 °C y 100 °C; February 2023; https://www.ugr.es/∼elenasb/teaching/densidadtemperatura_agua_tabla

[88] Engineering ToolBox, (2004). Water - Specific Heat vs. Temperature. [online] Available at: https://www.engineeringtoolbox.com/specific-heat-capacity-water-d_660.html; February 2023.

[89] R. Santamaria; Molecular Dynamics for Physicist, Chemistries, and Biologists; Springer; 2023.

[90] P. Vinet, J. Ferrante, J. R. Smith, and J. H. Rose; A universal equation of state for solids; Journal of Physics C: Solid State Physics **19**; L467; 1986.

[91] S. Merabia, J. Lombard, and A. Alkurdi; Importance of viscoelastic and interface bonding effects in the thermal boundary conductance of solid-water interfaces; International Journal of Heat and Mass Transfer **100**; pp. 287–294; 2016.

[92] R. Prasher; Acoustic mismatch model for thermal contact resistance of van der Waals contacts; Applied Physics Letters **94**; 041905; 2009.

[93] A. Jimenez, A. Sarsa, M. Blazquez, and T. Pineda; A molecular dynamics study of the surfactant surface density of alkanethiol self-assembled monolayers on gold nanoparticles as a function of the radius; Journal of Physical Chemistry C **114**; pp. 21309–21314; 2010.

[94] D. Alexeev, J. Chen, J. H. Walther, P. Konstantinos, P. Angelikopoulos, and P. Koumoutsakos; Kapitza Resistance between Few-Layer Graphene and Water: Liquid Layering Effects; Nano Letters **15** (9); pp. 5744–5749; 2015.

[95] L. J. Challis, K. Dransfeld, and J. Wilks; Heat Transfer Between Solids and Liquid Helium II; Proceedings of the Royal Society A: Mathematical, Physical and Engineering Sciences **260** (1300); pp. 31–46; 1961.

[96] H. Han, S. Merabia, F. Müller-Plathe; Thermal Transport at Solid-Liquid Interfaces: High Pressure Facilitates Heat Flow Through Non-Local Liquid Structuring; The Journal of Physical Chemistry Letters **8**; pp. 1946–1951; 2017.

[97] X. Peng, P. Jiang, Y. Ouyang, S. Lu, W. Ren, and J. Chen; Reducing Kapitza Resistance between Graphene/Water Interface via Interfacial Superlattice Structure; Nanotechnology **33**; 035707; 2021.

[98] M.M. Heyhat, A. Rajabpour, M. Abbasi, and S. Arabha; Importance of nanolayer formation in nanofluid properties: Equilibrium molecular dynamic simulations for Ag-water nanofluid; Journal of Molecular Liquids **264**; pp. 699–705; 2020.

[99] L. E. Paniagua-Guerra and B. Ramos-Alvarado; Thermal transport across flat and curved gold-water interfaces: Assessing the effects of the interfacial modeling parameter; The Journal of Chemical Physics **158**; 134717; 2023.

[100] M. Jiang, J. D. Olarte-Plata, and F. Bresme; Heterogeneous thermal conductance of nanoparticle-fluid interfaces: an atomistic nodal approach; The Journal of Chemical Physics **156**; 044701; 2022.

[101] U. Balucani, J. P. Brodhot, and R. Vallauri; Analysis of the velocity autocorrelation function of water; Journal of Physics: Condensed Matter **8** (34); pp. 6139–6144; 1996.

[102] C. Rocchi, A. R. Bizzarri, and S. Cannistraro; Water dynamical anomalies evidenced by molecular-dynamics simulations at the solvent-protein interface; Physical Review E **57** (3); pp. 3315–3325; 1998.

[103] J. Lan and B. Li; Thermal rectifying effect in two-dimensional anharmonic lattices; Physical Review B **74** (21); 214305; 2006.

[104] C. F. Richardson and P. Clancy; Contribution of thermal conductivity to the crystal-regrowth velocity of embedded-atom-method-modeled metals and metal alloys; Physical Review B **45** (21); pp. 12260–12268; 1992.

[105] S. Kuang and J. D. Gezelter; A gentler approach to RNEMD: Nonisotropic velocity scaling for computing thermal conductivity and shear viscosity; The Journal of Chemical Physics **133** (16); 164101; 2010.

[106] F. Römer, A. Lervik, and F. Bresme; Nonequilibrium molecular dynamics simulations of the thermal conductivity of water: A systematic investigation of the SPC/E and TIP4P/2005 model; The Journal of Chemical Physics **137** (7); 074503; 2012.

[107] D. Werner, S. Hashimoto, and T. Uwada; Remarkable Photothermal Effect of Interband Excitation on Nanosecond Laser-Induced Reshaping and Size Reduction of Pseudospherical Gold Nanoparticles in Aqueous Solution; Langmuir **26** (12); pp. 9956–9963; 2010.

[108] Open University (2008). S104 Book 3 Energy and Light, p. 59. The Open University.

[109] Charles E. Ophartd. (2003). Density of Gold. May 2021, from Elmhurst College Web site: http://chemistry.elmhurst.edu/vchembook/125Adensitygold.html

[110] K. Sääskilahti, J. Oksanen, J. Tulkki, and S. Volz; Role of anharmonic phonon scattering in the spectrally decomposed thermal conductance at planar interfaces; Physical Review B **90**; 134312; 2014.

[111] J. Chen, X. Xu, J. Zhou, and B. Li; Interfacial thermal resistance: Past, present, and future; Reviews of Modern Physics **94**; 025002; 2022.

[112] A. Anandakrishnan, B. Ramos-Alvarado, S. K. Kannam, and S. P. Sathian; Effects of interfacial molecular mobility on thermal boundary conductance at solid-liquid interface; The Journal of Chemical Physics **158**; 094710; 2023.

[113] K. Sääskilahti, J. Oksanen, J. Tulkki, and S. Volz; Spectral mapping of heat transfer mechanisms at liquid-solid interfaces; Physical Review E **93**; 052141; 2016.

[114] S. Moon, Q. Zhang, Z. Xu, D. Huang, S. Kim, J. Schiffbauer, E. Lee, and T. Luo; Plasmonic Nanobubbles - A Perspective; arXiv:2108.07921 [physics.optics].

[115] H. Löwen and P. A. Madden; A microscopic mechanism for shock-wave generation in pulsed-laser-heated colloidal suspensions; Journal of Chemical Physics **97**; pp. 8760–8766.; 1992.

[116] C. Vega, J. L. F. Abascal, and I. Nezbeda; Vapor-liquid equilibria from the triple point up to the critical point for the new generation of TIP4P-like models: TIP4P/Ew, TIP4P/2005, andTIP4P/ice; The Journal of Chemical Physics **125**; 034503; 2006.

[117] Material Measurement Laboratory. (2018). SAT-TMMC: Liquid-Vapor coexistence properties - TIP4P/2005 Water (LRC). May 2021, from National Institute of Standars and Technology, Web site: https://www.nist.gov/mml/csd/chemical-informatics-research-group/sat-tmmc-liquid-vapor-coexistence-properties-tip4p2005.

[118] G. Baffou and H. Rigneault; Femtosecond-pulsed optical heating of gold nanoparticles; Physical Review B **84**; 035415; 2011.

[119] D. Wang, P. Cheng, and X. Quan; Photothermal nanobubble nucleation on a plasmonic nanoparticle: A 3D lattice Boltzmann simulation; International Journal of Heat and Mass Transfer **140**; pp. 786–797; 2019.

[120] J. Neumann, and R. Brinkmann; Boiling nucleation on melanosomes and microbeads transiently heated by nanosecond and microsecond laser pulses; Journal of Biomedical Optics **10**; 024001; 2005.

[121] R. Tiery, S. Loock, and L. Mercury; Explosive properties of superheated aqueous solutions in volcanic and hydrothermal systems; Metastable Systems under Pressure; Springer; pp. 293–310; insu-00460799; 2010.

[122] JG Eberhart; A New Four-Parameter Equation of State and Its Application in Predicting the Spinodal Temperature of Water; Water Journal **1**; pp. 85–91; 2009.

[123] V. Gerweck and G. Yadigaroglu; A local equation of state for a fluid in the presence of a wall and its application to rewetting; International Journal of Heat and Mass Transfer **35**; pp. 1823–1832; 1992.

[124] V. P. Carey and A. P. Wemhoff; Thermodynamic analysis of near-wall effects on phase stability and homogeneous nucleation during rapid surface heating; International Journal of Heat and Mass Transfer **48**; pp. 5431–5445; 2005.

[125] M. Hu, H. Petrova, and G. V. Hartland; Investigation of the properties of gold nanoparticles in aqueous solution at extremely high lattice temperatures; Chemical Physics Letters **391**; pp. 220–225; 2004.

[126] V. Kotaidis and A. Plech; Cavitation dynamics on the nanoscale; Applied Physics Letters **87**; 213102; 2005.

[127] E. Boulais, R. Lachaine, and M. Meunier; Plasma Mediated off-Resonance Plasmonic Enhanced Ultrafast Laser-Induced Nanocavitation; Nano Letters **12**; pp. 4763–4769; 2012.